Transition-Edge Sensors

K. D. Irwin and G. C. Hilton

National Institute of Standards and Technology
Mail Stop 817.03
325 Broadway
Boulder, CO 80305

Transition-Edge Sensors[*]

K. D. Irwin and G. C. Hilton
National Institute of Standards and Technology
Boulder, CO 80305-3328 USA

April 29, 2005

Abstract

In recent years, superconducting transition-edge sensors (TES) have emerged as powerful, energy-resolving detectors of single photons from the near infrared through gamma rays and sensitive detectors of photon fluxes out to millimeter wavelengths. The TES is a thermal sensor that measures an energy deposition by the increase of resistance of a superconducting film biased within the superconducting-to-normal transition. Small arrays of TES sensors have been demonstrated, and kilopixel arrays are under development. In this chapter, we describe the theory of the superconducting phase transition, derive the TES calorimeter response and noise theory, discuss the state of understanding of excess noise, and describe practical implementation issues including materials choice, pixel design, array fabrication, and cryogenic SQUID multiplexing.

Contents

1   Introduction

In 1911, Heike Kamerlingh Onnes cooled a sample of mercury in liquid helium, and made the dramatic discovery that its electrical resistance drops abruptly to zero as it cools through its superconducting transition temperature, $T_c = 4.2\,\mathrm{K}$ [1]. A large number of materials have since been found to have phase transitions into a zero-resistance state at various transition temperatures. The superconducting phase transition can be extremely sharp, suggesting its use as a sensitive thermometer (Fig. 1). In fact, the logarithmic sensitivity (Chapt. 1) of a superconducting transition, $\alpha = d\log R/d\log T$, can be two orders of magnitude more sensitive than that of the semiconductor thermistor thermometer that has been used so successfully in cryogenic calorimeters (Chapt. 2).

A superconducting transition-edge sensor (TES), also called a superconducting phase-transition thermometer (SPT) , consists of a superconducting film operated in the narrow temperature region between the normal and superconducting state, where the electrical resistance varies between zero and its normal value. A TES thermometer can be used in a bolometer (to measure power) or in a calorimeter (to measure a pulse of energy). The sensitivity of a TES makes it possible in principletransitionfig to develop thermal detectors with faster response, larger heat capacity, and smaller detectable energy input than thermal detectors made using conventional semiconductor thermistors. However, the sharp transition leads to a greater tendency for instability and lower saturation energy, so that careful design is required.

In 1941, D.H. Andrews applied a current to a fine tantalum wire operating in its superconducting transition region at $3.2\,\mathrm{K}$ and measured the change in resistance caused by an infrared signal [2]. This was the first demonstration of a TES bolometer. In 1949, the same researcher applied a current to a niobium nitride strip within its superconducting transition at $15\,\mathrm{K}$ and measured the voltage pulses when it was bombarded by alpha particles [3] - the first reported demonstration of a TES calorimeter. This work followed on earlier suggestions by Andrews himself in 1938 [4] and Goetz in 1939 [5].

During the first half century after their invention, TES detectors were seldom used in practical applications. One of the principal barriers to their adoption was the difficulty of matching their noise to FET amplifiers (the TES normal resistance is typically a few ohms or less). In order to noise match, the TES was sometimes read out using a cross-correlation circuit to cancel noise [6], ac biased in conjunction with a step-up transformer [7], or fabricated in long meander lines with high normal resistance [8, 9]. In recent years, this problem has been largely eliminated by the use of superconducting quantum interference device (SQUID) current amplifiers [10], which are easily impedance-matched to low-resistance TES detectors [11, 12]. In addition to their many other advantages, SQUID amplifiers make it possible to multiplex the readout of TES detectors (Sect. 4.2), so that large arrays of detectors can be instrumented with a manageable number of wires to room temperature. Large arrays of TES detectors are now being deployed for a number of different applications.

Another barrier to the practical use of TES detectors has been that it is difficult to operate them within the extremely narrow superconducting transition region. When they are current-biased, Joule heating of the
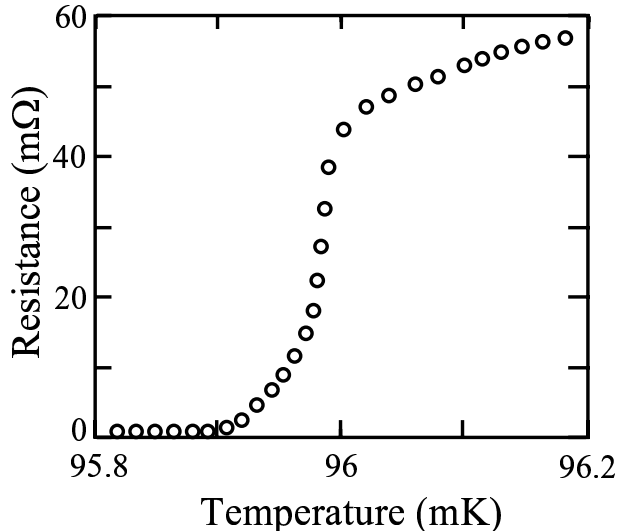
Figure 1: The transition of a superconducting film (a Mo/Cu proximity bilayer) from the normal to the superconducting state near 96 mK. The sharp phase transition suggests its use as a sensitive thermometer.

TES by the current can lead to thermal runaway, and small fluctuations in bath temperature significantly degrade performance. Furthermore, variations in the transition temperature between multiple devices in an array of TES detectors can make it impossible to bias them all at the same bath temperature. As will be explained in Sect. 2.5, when the TES is instead voltage-biased and read out with a current amplifier, the devices can easily be stably biased and they self-regulate in temperature within the transition with much less sensitivity to fluctuations in the bath temperature [13]. The introduction of voltage-biased operation with SQUID current readout has led to an explosive growth in the development of TES detectors in the past decade.

The potential of TES detectors is now being realized. TES detectors are being developed for measurements across the electromagnetic spectrum from millimeter [14, 15, 16] through gamma rays [17, 18] as well as with weakly interacting particles [19] and biomolecules [20, 21, 22]. They have contributed to the study of dark matter and supersymmetry [23, 24], the chemical composition of materials [25], and the new field of quantum information [26]. They have extended the usefulness of the single-photon calorimeter all the way to the near infrared [27], with possible extension to the far infrared. They are being used in the first multiplexed submillimeter, millimeter-wave, and x-ray detectors for spectroscopy and astronomical imaging [28, 29, 15, 16, 30].

2   Superconducting transition-edge sensor theory

We now describe the theory of a superconducting transition-edge sensor. We describe the physics of the superconducting transition (2.1), summarize the equations for TES small-signal theory (2.2), and analyze the bias circuit for a TES and its electrical and thermal response (2.3), the conditions for the stability of a TES (2.4), the consequences of negative electrothermal feedback (2.5), thermodynamic noise (2.6), unexplained noise (2.7), and the effects of operation outside of the small-signal limit (2.8). Particular implementations of both TES single pixels and arrays, including performance results, will be described in Sects. 3 and 4.

2.1   The superconducting transition

In this work, we discuss sensors based on traditional "low-T_c" superconductors (often those with transition temperatures below 1 K). Other classes of superconductors, including the cuprates such as yttrium-barium-copper-oxide, are also used in thermal detectors. Transition-edge sensors based on these "high-T_c" materials have much lower sensitivity and much higher saturation levels than those that are discussed here.

In low-T_c materials, the phenomenon of superconductivity has been fairly well understood since the 1950s, when detailed microscopic and macroscopic theories were developed. Superconductivity in low-T_c materials occurs when two electrons are bound together in "Cooper" pairs, acting as one particle. The energy binding Cooper pairs prevents them from scattering, allowing them to flow without resistance. Bardeen, Cooper, and Schrieffer first explained the formation of Cooper pairs in 1957 in the landmark microscopic BCS theory [31].

The energy binding the two electrons in a Cooper pair is due to interactions with positive ions in the lattice mediated by phonons (quantized lattice vibrations). When a negatively charged electron flows in a superconductor, positive ions in the lattice are drawn towards it, creating a cloud of positive charge. A second electron is attracted to this cloud. The energy binding the two electrons is referred to as the "superconducting energy gap" of the material. In the BCS theory, the size of the Cooper pair wave function is determined by the temperature-dependent coherence length $\xi(T)$, which has the zero-temperature value $\xi_0 \equiv \xi(0) \approx 0.18 v_\text{F}/(k_\text{B} T_\text{c})$. Here v_F is the Fermi velocity of the material, k_B is the Boltzmann constant, and T_c is the superconducting transition temperature. At temperatures above the transition temperature, thermal energies of order $k_\text{B} T$ spontaneously break Cooper pairs and superconductivity vanishes. In a BCS superconductor, the transition temperature T_c is related to the superconducting energy gap E_gap of the material by $E_\text{gap} = 2\delta(0) \approx 3.5 k_\text{B} T_\text{c}$. In addition to perfect dc conductivity below T_c, a second hallmark of superconductivity is the Meissner effect: the free energy of the system is minimized when an external magnetic field is excluded from the interior of a superconducting sample. An applied magnetic field is exponentially screened by an induced Cooper-pair supercurrent with an effective temperature-dependent penetration depth, $\lambda_\text{eff}(T)$. The approximate zero-temperature value of the penetration depth is the London penetration depth, $\lambda_\text{L}(0)$.

Near the transition temperature, the physics of a superconductor is well described by the macroscopic Ginzburg–Landau theory [32], which was derived by a Taylor expansion of a phenomenological order parameter Ψ. Ψ was later shown to be proportional to the density of superconducting pairs [33]. One result of the Ginzburg–Landau theory is that the characteristics of a superconductor with penetrating magnetic flux (such as a superconductor on its transition) are strongly dependent on its dimensionless Ginzburg–Landau parameter, $\kappa \equiv \lambda_\text{eff}(T)/\xi(T)$. If $\kappa < 1/\sqrt{2}$, the superconductor is of Type I, and the free energy is minimized when magnetic flux that has penetrated the material clumps together. If $\kappa > 1/\sqrt{2}$, the superconductor is of Type II, and magnetic flux that has penetrated the material preferentially separates into individual flux quanta that repel each other. The size of the flux quantum is $\Phi_0 = h/2e = 2.0678 \times 10^{-15}$ Wb. Whether a film is of Type I or II influences the physics of the transition, its noise behavior, current-carrying capability, and sensitivity to magnetic field. Transition-edge sensors with $T_\text{c} < 1$ K can be either Type I or II.

The superconducting films considered in this section are usually in the dirty limit (the coherence length is typically $> 1 \,\mu$m for $T_\text{c} < 1$ K, and mean free paths are usually a few tens or hundreds of nanometers.) See Table 2 in Sect. 3 for a list of coherence lengths of typical TES superconductors. A film in the dirty limit at T_c has an approximate Ginzburg–Landau Parameter ([34] pg. 120),

$$\kappa \approx 0.715 \, \lambda_\text{L}(0)/\ell(d) \,, \tag{1}$$

where $\ell(d)$ is the electron mean free path, which is a function of the film thickness d. See Table 2 for a list of London penetration depths, and Sect. 3.4 for a discussion of the electron mean free path. As can be shown by (1), TES detectors with a high mean free path, such as many TES x-ray detectors, have a low κ and are typically Type I. TES detectors with a shorter mean free path, including optical TES detectors fabricated using thin tungsten films, have a higher κ and are typically Type II.

The physics of a BCS superconductor well below T_c is largely understood. However, the situation is more complicated in the transition region. In a typical TES, the measured transition width in the presence of a very small bias current (e.g. the current from a sensitive resistance bridge) is 0.1 mK to ~ 1 mK. In the presence of typical operational bias currents, the transition width is usually a few mK. The variation of resistance with temperature can be caused by nonuniformities in T_c, by an external field, by transport current densities approaching the critical current density, by magnetic fields induced by transport current, or by variations in temperature within the TES due to Joule heating or other sources of power. The transition is strongly influenced by the geometry and by imperfections in the boundaries of the film and in the film itself. However, the transition width is finite even for a uniform film with near-zero applied current and no external field, which is the case that we consider first.

In a Type II superconductor, a current exerts a Lorentz force on flux quanta at pinning sites in the film. When the current is near zero, the Lorentz force is insufficient to overcome the pinning force, and the superconductor does not exhibit dc electrical resistance. However, as the temperature approaches the transition temperature, thermal energy of order $k_{\rm B}T$ allow flux lines to jump between pinning sites, creating a voltage and a finite transition width. The number of vortices present is a function of the magnetic field. Even at zero field, vortex-antivortex pairs can be thermally generated in the interior of the film. At the Kosterlitz-Thouless transition temperature of the film, $T_{\rm KT}$ [35, 36], thermal energies are sufficient to generate and unbind vortex-antivortex pairs, creating a thermally excited distribution of vortices that can move in response to a transport current. $T_{\rm KT}$ is typically slightly below $T_{\rm c}$, leading to a finite transition width even in a perfect Type II film at zero field and transport current approaching zero.

A finite transition width must also occur in Type I superconductors, because thermodynamic fluctuations cause the system to statistically sample any states that raise the free energy by about $k_{\rm B}T$. In a thin, one-dimensional superconducting wire, as the transition is approached, fluctuations periodically cause the order parameter to reach zero at some point, allowing a phase slip of 2π [37]. These phase slips lead to a finite transition width. The onset of resistance occurs when $k_{\rm B}T$ approaches the energy required to drive a segment of the wire as long as $\xi(T)$ normal. Quantitative predictions of the phase-slip-driven width of the transition of tin wires have been experimentally verified [38, 39].

At the bottom of the transition (near $R = 0$) in a perfect two-dimensional Type I thin film (wider than $\xi(T)$) at zero current bias, it is energetically unfavorable for thermal fluctuations to drive a segment that is the entire width of the film normal. The transition is thus more complicated in a two-dimensional Type I film than in a one-dimensional Type I film. Any flux that penetrates a Type I film tends to clump together, producing larger superconducting and normal regions - a situation referred to as the "mixed state." As in Type II materials, flux can be generated either by magnetic fields or by thermal effects near $T_{\rm c}$. Smaller normal regions in Type I materials can move in response to a transport current. Higher in the transition, normal regions that span the entire width of the superconducting film lead to resistance even when they do not move. Both of these phenomena lead to a finite transition width at zero field and near-zero applied current.

The transition widths predicted by flux motion in perfect superconducting films at near-zero current bias are typically much smaller than the transition widths measured under bias in a practical TES. In a TES, the approximations of near-zero applied current and film uniformity are not valid. It is obvious that nonuniformity of $T_{\rm c}$ or applied magnetic field can lead to finite transition widths. Large bias currents can also lead to transition broadening through Joule heating, critical current effects and self-induced magnetic fields. We now discuss the effect of large transport currents.

Joule heating in the film can lead to variations in temperature across the film, resulting in apparently larger transition widths, and to instability against phase separation into two or more normal and superconducting regions [40]. The effects of self-heating depend on the thermal conductances and geometry of the detector and the form of the superconducting transition. In the general case, the effects of self-heating must be analyzed numerically. However, a simple analysis shows how the effect of self-heating on the transition scales.

At temperatures below $1\,\rm K$, conductance in a normal-metal film is dominated by Wiedemann–Franz thermal conductance of the normal electrons, $G_{\rm WF} = L_0 T/R$, where R is the resistance of the film and L_0 is the Lorenz number (see Sect. 3.5). The temperature variation caused by the Joule power dissipation depends on the geometry of the detector and the geometry of its link to the heat sink, but is of order $\delta T \sim P_{\rm J}/G_{\rm WF}$, where $P_{\rm J}$ is the Joule power dissipation in the film.

Self-heating can also lead to detector instability and geometrical separation of parts of the device into superconducting and normal phases. If parallel segments of a TES have a temperature differential, the hotter segment has a higher temperature and resistance, and the current preferentially flows to the low-resistance segment, leading to stability. However, if series segments of a TES have a temperature differential, the hottest segment has the highest resistance and receive the highest Joule power, which can lead to thermal runaway and separation into superconducting and normal-phase regions. The condition for thermal runaway depends on the geometry of the TES and its link to the heat sink. In the case where the heat flows uniformly from the TES to the heat bath (for instance, in the case where electron-phonon decoupling is the dominant thermal conductance), the condition for stability against phase separation in a rectangular film can be solved

in closed form by expansion of the temperature profile in a two-dimensional Fourier series [40]:

$$R_{\mathrm{N}} < \pi^2 \frac{L_0 T_{\mathrm{c}} n}{G \alpha} \ , \tag{2}$$

where R_{N} is the normal resistance of the film, n is the exponent of power flow to the heat bath (see Sect. 2.3), G is the thermal conductance to the heat bath, and $\alpha = d \log R / d \log T$ is the logarithmic sensitivity of the superconducting transition. At normal resistance above this value, the Wiedemann–Franz thermal conductance is insufficient to prevent separation into superconducting and normal phases.

Even if the Wiedemann–Franz thermal conductance is large enough to minimize temperature gradients in the TES, large transport currents can lead to broadening of the transition width. In Type II films, this broadening occurs as the Lorentz force becomes large enough to overcome the forces binding flux quanta to pinning sites in the material, leading to flux flow and dissipation further below T_{c}. In Type I films, the process is even more complicated. A solution of the Ginzburg–Landau equations shows that well below T_{c} and I_{c}, most of the current flows along the edges of the film. As the bias current approaches the critical current, or the temperature approaches the transition temperature, normal regions are created at the edges that grow across the full width of the film in a phase-slip line (PSL) with a normal core of width $\xi_{\mathrm{eff}}(T)$ [41]. As the transport current crosses a PSL, it is carried predominantly by the quasiparticles. After crossing the PSL, a fraction of the current is converted to supercurrent by Andreev reflection, but a fraction continues to be carried in the quasiparticle branch. The quasiparticle current relaxes back to a supercurrent over a timescale τ_{Q^*}, the quasiparticle branch-imbalance relaxation time. This time corresponds to an effective normal length scale $\Lambda_{\mathrm{Q}^*} = \sqrt{D \tau_{\mathrm{Q}^*}}$, where D is the diffusion coefficient of the film. As $T \to T_{\mathrm{c}}$, the Andreev reflected component goes to zero and Λ_{Q^*} diverges, leading to a broadened transition width in the presence of a large current.

The situation is complicated by the fact that new PSLs can be nucleated and denucleated either as a function of the current and temperature, or due to fluctuations. The nucleation of new PSLs leads to steps in the differential resistance of the film. Steps in the differential resistance can in some cases be measured in the complex impedance of a TES, and may be due to the nucleation of new PSLs. Also, the telegraph noise sometimes seen in TES devices may be due to the nucleation of new PSLs. Attempts have been made to derive approximate limits on the α of a TES due to variations in Λ_{Q^*}[40].

The transition temperature of the TES must be chosen to achieve the needed energy resolution and response time, and to match the available cryogenic system for a particular application. The energy resolution and response time of a TES depend strongly on the temperature because of the temperature dependence of the heat capacity, thermal conductance, thermal noise, and other parameters. Fortunately, the transition temperature can be tuned to the desired value by choosing an element with an appropriate superconducting transition temperature, by the use of the proximity effect in a normal/superconductor bilayer, or by the use of magnetic dopants to suppress the T_{c} of a superconductor (see Sect. 3). The most commonly chosen transition temperatures are $\sim 100\,\mathrm{mK}$ (above the bath temperature in an adiabatic demagnetization refrigerator or dilution refrigerator), and $\sim 400\,\mathrm{mK}$ (above the bath temperature of a ^{3}He refrigerator).

2.2 TES Small Signal Theory Summary

In Table 1, we summarize the equations for the ideal small-signal performance of a TES. These equations are similar to those derived in Chapt. 1, but are specialized for a TES calorimeter. Most importantly, they explicitly include the inductance in the bias circuit, which strongly influences the detector response and noise performance. Because of interactions between the electrical and thermal poles, a consideration of the inductance in the bias circuit is required even to compute the response time of the TES. The explicit inclusion of inductance also allows a computation of the conditions for stability. The results in this section reduce to the results in Chap. 1 when the inductance is taken to zero, to the extent that there are comparable equations. In these summary tables, we present the equations for the response of a TES to a delta-function energy impulse, the response to an incident power load (the power responsivity), the response of a TES to a signal on the bias line (the complex impedance), the stability criteria, the equations for electrothermal feedback (ETF) self-calibration, and the noise equivalent power and energy resolution. The derivation of these equations follows in Sects. 2.3–2.6, but they are gathered here for convenience, with terms defined in

the following sections. These equations do not include the effects of excess noise or large signals, which are described in Sects. 2.7 and 2.8.

The derivation of the equations is complicated, but full understanding of all of the mathematical steps is not necessary to make use of the equations. If a detailed understanding of the derivations is not desired, Sects. 2.3–2.6 can be skipped.

2.3   TES electrical and thermal response

In this section, we discuss the electrical and thermal bias circuit of the TES and derive the differential equations describing the TES response. In the small signal limit, we solve the equations for response to a pulse of energy (as in a calorimeter), response to an input power (as in a bolometer), and response to a voltage signal on the bias line (the complex impedance of the TES). In later sections, we use these equations to derive the conditions for stability, fluctuations due to noise, and the achievable energy resolution and noise equivalent power.

A TES can be biased with real source impedance ranging from zero (constant voltage bias) to infinite (constant current bias). When a voltage amplifier is used, the chosen bias condition is typically close to a constant-current bias, so as to minimize loading effects that increase the relative amplifier noise and minimize the Johnson noise contribution of the load resistor. When a SQUID current amplifier [10] is used, the bias condition is typically close to a constant-voltage bias for the same reasons. The bias circuit also has reactive elements. For the low-impedance, voltage-bias case, this reactance principally consists of parasitic inductance in the leads and inductance from the SQUID input coil. For a high impedance, current bias case, this reactance principally consists of parasitic capacitance and capacitance from the voltage amplifier. In most cases, TES detectors are now low-impedance devices coupled to SQUID amplifiers. This is the configuration that we consider in this section.

SQUID amplifiers are operated at low temperatures, but they are biased and read out with room-temperature electronics. Wires are run from room temperature to the operating temperature of the SQUID to provide a bias current, to measure the voltage across the SQUID, and to provide a feedback flux to the SQUID to linearize its output.

The output voltage of a typical SQUID is too low to couple directly to a room-temperature amplifier without significant degradation in noise performance, so a variety of techniques are used to improve the match. These include modulating the SQUID and transforming its impedance with a wirewound transformer, the use of "additional positive feedback" to increase the transimpedance of the SQUID (at the cost of reduced dynamic range)[42], the use of "noise cancellation," [43] and the use of a series array of SQUIDs to increase the output voltage swing [44, 45, 46].

One example implementation of a SQUID circuit to read out a TES is shown in Fig. 2. In this circuit, the stray inductance is kept small by mounting the first-stage SQUID chip at the base temperature of the cryostat, adjacent to a chip with the TES. The shunt resistor is fabricated on the TES chip, and the TES chip is connected to the first-stage SQUID chip by wirebonds. The first-stage SQUID is voltage-biased in series with the input coil of a series-array-SQUID second-stage amplifier. The series-array SQUID amplifies the signal sufficiently to couple to room-temperature electronics.

In addition to the shunt resistance R_{SH} and the TES resistance shown in Fig. 2, the bias circuit of the TES can also have a parasitic resistance R_{PAR} in series with the SQUID input coil (Fig. 3a). The TES bias circuit can be represented by a Thevenin-equivalent circuit consisting of a bias circuit with a voltage $V = I_{\mathrm{BIAS}}R_{\mathrm{SH}}$ applied to a series combination of a load resistor $R_{\mathrm{L}} = R_{\mathrm{SH}} + R_{\mathrm{PAR}}$, the SQUID input inductance L, and the TES (Fig. 3b). It is this Thevenin-equivalent circuit that we analyze in this work.

The response of the TES is governed by two coupled differential equations describing the electrical and thermal circuits. Each differential equation governs the evolution of a state variable: the electrical equation determines the current I, and the thermal equation determines the temperature T. Ignoring noise terms for the present, the *thermal differential equation* is:

$$C\frac{\mathrm{d}T}{\mathrm{d}t} = -P_{\mathrm{bath}} + P_{\mathrm{J}} + P \, , \tag{3}$$

where C is the heat capacity (of both the TES and any absorber), T is the temperature of the TES (the state variable), P_{bath} is the power flowing from the TES to the heat bath, P_{J} is the Joule power dissipation and P is the signal power.

Table 1: Summary of important equations for TES small-signal performance

Definitions (Section 2.3):

$$\alpha_I \equiv \frac{T_0}{R_0}\frac{\partial R}{\partial T}\bigg|_{I_0} \qquad\qquad \beta_I \equiv \frac{I_0}{R_0}\frac{\partial R}{\partial I}\bigg|_{T_0} \qquad\qquad \mathscr{L}_I \equiv \frac{P_{J_0}\alpha_I}{GT_0}, \text{ where } P_{J_0} = I_0^2 R_0$$

Time constants:

Natural (no feedback)
$$\tau = \frac{C}{G}$$

Zero-inductance effective thermal
$$\tau_{\text{eff}} = \tau\frac{1+\beta_I+R_L/R_0}{1+\beta_I+R_L/R_0+(1-R_L/R_0)\mathscr{L}_I}$$

Delta-function response (rise time τ_+, fall τ_-)
$$\frac{1}{\tau_\pm} = \frac{1}{2\tau_{\text{el}}} + \frac{1}{2\tau_I} \pm$$
$$\frac{1}{2}\sqrt{\left(\frac{1}{\tau_{\text{el}}}-\frac{1}{\tau_I}\right)^2 - 4\frac{R_0}{L}\frac{\mathscr{L}_I(2+\beta_I)}{\tau}}$$

Constant-current
$$\tau_I = \frac{\tau}{1-\mathscr{L}_I}$$

Electrical
$$\tau_{\text{el}} = \frac{L}{R_L + R_0(1+\beta_I)}$$

Low-inductance limit of $\tau_\pm$
$$\tau_+ \to \tau_{\text{el}} \text{ and } \tau_- \to \tau_{\text{eff}}$$

Current response to an energy impulse: $(t > 0)$

$$\delta I(t) = \left(\frac{\tau_I}{\tau_+}-1\right)\left(\frac{\tau_I}{\tau_-}-1\right)\frac{1}{(2+\beta_I)}\frac{C\delta T}{I_0 R_0 \tau_I^2}\frac{\left(e^{-t/\tau_+}-e^{-t/\tau_-}\right)}{(1/\tau_+ - 1/\tau_-)} \qquad\qquad \tau_+ \neq \tau_-$$

$$\delta I(t) = \left(\frac{\tau_I}{\tau_\pm}-1\right)^2\frac{1}{(2+\beta_I)}\frac{C\delta T}{I_0 R_0 \tau_I^2}\left(-te^{-t/\tau_\pm}\right) \qquad\qquad \tau_+ = \tau_-$$

Power-to-current responsivity: $(\omega = 2\pi f)$

$$
\begin{aligned}
s_I(\omega) &= -\frac{1}{I_0 R_0}\frac{1}{(2+\beta_I)}\frac{(1-\tau_+/\tau_I)}{(1+i\omega\tau_+)}\frac{(1-\tau_-/\tau_I)}{(1+i\omega\tau_-)} \\
&= -\frac{1}{I_0 R_0}\left(\frac{L}{\tau_{\text{el}}R_0\mathscr{L}_I} + \left(1-\frac{R_L}{R_0}\right) + i\omega\frac{L\tau}{R_0\mathscr{L}_I}\left(\frac{1}{\tau_I}+\frac{1}{\tau_{\text{el}}}\right) - \frac{\omega^2\tau}{\mathscr{L}_I}\frac{L}{R_0}\right)^{-1}
\end{aligned}
$$

Complex impedence:

$$Z(\omega) = R_L + i\omega L + Z_{\text{TES}}(\omega),$$

where

$$Z_{\text{TES}}(\omega) = R_0(1+\beta_I) + \frac{R_0\mathscr{L}_I}{1-\mathscr{L}_I}\frac{2+\beta_I}{1+i\omega\tau_I}$$

Stability (Sect. 2.4):

$$
\begin{aligned}
L_{\text{crit}\pm} = &\left(\mathscr{L}_I\left(3+\beta_I-\frac{R_L}{R_0}\right)+\left(1+\beta_I+\frac{R_L}{R_0}\right)\pm\right.\\
&\left.2\sqrt{\mathscr{L}_I(2+\beta_I)\left(\mathscr{L}_I\left(1-\frac{R_L}{R_0}\right)+\left(1+\beta_I+\frac{R_L}{R_0}\right)\right)}\right)\frac{R_0\tau}{(\mathscr{L}_I-1)^2}
\end{aligned}
$$

Table 1 (continued)

$\tau_+ = \tau_-$, or $L = L_{\mathrm{crit}\pm}$	Critical damping ($L_{\mathrm{crit}-}$ most important)
$L < L_{\mathrm{crit}-}$ or $L > L_{\mathrm{crit}+}$	Overdamping
$\dfrac{L_{\mathrm{crit}\pm}}{R_0} = \left(3 + \beta_I \pm 2\sqrt{2 + \beta_I}\right)\dfrac{\tau}{\mathscr{L}_I}$	In the limit $R_{\mathrm{L}} = 0$, $\mathscr{L}_{\mathrm{I}} \gg 1$
$R_0 > \dfrac{(\mathscr{L}_I - 1)}{(\mathscr{L}_I + 1 + \beta_I)} R_L$	Stability condition, overdamped
$\tau > (\mathscr{L}_I - 1)\,\tau_{\mathrm{el}}$	Stability condition, underdamped

ETF self-calibration (Sect. 2.5):

$\delta P_{\mathrm{ETF}} = -I_0(R_0 - R_L)\delta I$	ETF power
$E_{\mathrm{ETF}} = (I_0 R_L - V)\int_0^\infty \delta I(t)dt + R_L \int_0^\infty \delta I(t)^2 dt$	ETF energy

Noise (Sect. 2.6): (linear approx. $\xi(I_0) = 1$, quadratic approx. $\xi(I_0) = 1 + 2\beta_{\mathrm{I}}$)

$S_{V_{\mathrm{TES}}} = 4k_{\mathrm{B}}T_0 R_0 \xi(I_0)$	TES voltage noise
$S_{I_{\mathrm{TES}}}(\omega) = 4k_{\mathrm{B}}T_0 I_0^2 R_0 \xi(I_0)(1 + \omega^2\tau^2)|s_I(\omega)|^2/\mathscr{L}_I^2$	TES current noise
$S_{V_{\mathrm{L}}} = 4k_{\mathrm{B}}T_0 R_L$	Load voltage noise
$S_{I_{\mathrm{L}}}(\omega) = 4k_{\mathrm{B}}T_L I_0^2 R_L (\mathscr{L}_I - 1)^2(1 + \omega^2\tau_I^2)|s_I(\omega)|^2/\mathscr{L}_I^2$	Load current noise
$S_{P_{\mathrm{TFN}}} = 4k_{\mathrm{B}}T_0^2 G F(T_0, T_{\mathrm{bath}})$	TFN power noise
$S_{I_{\mathrm{TFN}}}(\omega) = 4k_{\mathrm{B}}T_0^2 G F(T_0, T_{\mathrm{bath}})|s_I(\omega)|^2$	TFN current noise

Total power-referred noise: ($S_{I_{\mathrm{amp}}}(\omega)$ is the SQUID noise current)

$$
\begin{aligned}
S_{P_{\mathrm{tot}}}(f) =\ & S_{P_{\mathrm{TFN}}} + S_{V_{\mathrm{TES}}} I_0^2 \frac{1}{\mathscr{L}_I^2}\left(1 + \omega^2\tau^2\right) + \\
& S_{V_{\mathrm{L}}} I_0^2 \frac{(\mathscr{L}_I - 1)^2}{\mathscr{L}_I^2}\left(1 + \omega^2\tau_I^2\right) + \frac{S_{I_{\mathrm{amp}}}(\omega)}{|s_I(\omega)|^2}
\end{aligned}
$$

Energy resolution: (for $S_{I_{\mathrm{amp}}} = 0$)

$$
\begin{aligned}
\delta E_{\mathrm{FWHM}} =\ & 2\sqrt{2\ln 2}\Bigg(\frac{\tau}{\mathscr{L}_I^2}\bigg(\left(\mathscr{L}_I^2 S_{P_{\mathrm{TFN}}} + I_0^2 S_{V_{\mathrm{TES}}} + (\mathscr{L}_I - 1)^2 I_0^2 S_{V_{\mathrm{L}}}\right) \times \\
& \left(I_0^2 S_{V_{\mathrm{TES}}} + I_0^2 S_{V_{\mathrm{L}}}\right)\bigg)^{1/2}\Bigg)^{1/2}
\end{aligned}
$$

In the limit $R_{\mathrm{L}} = 0$, $\mathscr{L}_{\mathrm{I}} \gg 1$:

$$
\begin{aligned}
\delta E_{\mathrm{FWHM}} =\ & 2\sqrt{2\ln 2}\sqrt{\frac{\tau I_0}{\mathscr{L}_I}\sqrt{\left(S_{P_{\mathrm{TFN}}}\right)\left(S_{V_{\mathrm{TES}}}\right)}} \\
=\ & 2\sqrt{2\ln 2}\sqrt{\frac{4k_{\mathrm{B}}T_0^2 C}{\alpha_I}\sqrt{\frac{nF(T_0, T_{\mathrm{bath}})\xi(I_0)}{1 - (T_{\mathrm{bath}}/T_0)^n}}}
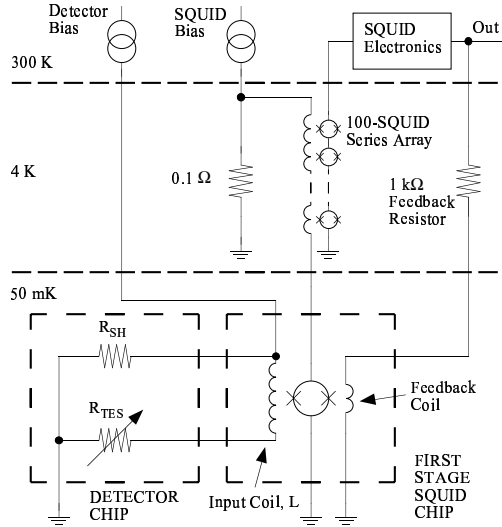\end{aligned}
$$

Figure 2: An example of a SQUID readout circuit for a TES. A TES is voltage-biased by applying a current to a small shunt resistor R_{SH} in parallel with the TES resistance $R_{\mathrm{TES}} \gg R_{\mathrm{SH}}$. The current through the TES is measured by a first-stage SQUID, which is in turn voltage-biased by a current through a small shunt resistor with resistance $\approx 0.1\Omega$. The output current of the first-stage SQUID is measured by a series-array SQUID. A feedback flux is applied to linearize the first-stage SQUID.
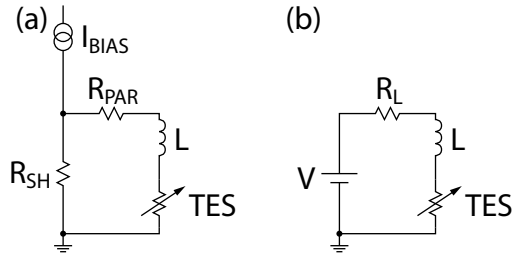

Figure 3: The TES input circuit and a Thevenin-equivalent representation. (a) A bias current I_{BIAS} is applied to a shunt resistor R_{SH} in parallel with a parasitic resistance R_{PAR}, an inductance L (including both SQUID and stray inductance), and a TES. (b) The circuit model used in this section, the Thevenin equivalent of the circuit in 3(a). A bias voltage $V = I_{\mathrm{BIAS}} R_{\mathrm{SH}}$ is applied to a load resistor $R_{\mathrm{L}} = R_{\mathrm{SH}} + R_{\mathrm{PAR}}$, the inductance L, and the TES.

Once again ignoring noise terms, the *electrical differential equation* is:

$$L\frac{\mathrm{d}I}{\mathrm{d}t} = V - IR_L - IR(T,I) \;, \tag{4}$$

where L is the inductance, V is the Thevenin-equivalent bias voltage, I is the electrical current through the TES (the state variable) and $R(T,I)$ is the electrical resistance of the TES, which is generally a function of both temperature and current. One subtlety is that, depending on the design, a feedback flux applied to the SQUID can reduce the effective value of L within the bandwidth of the feedback. The feedback bandwidth can be (but is not always) larger than the signal bandwidth. If feedback changes the inductance, the physical L should be used in signal-to-noise ratio calculations, and the effective L (including any reduction due to feedback) should be used in calculations of signal level and stability.

These differential equations can be solved in this form [13, 47, 48], or they can be converted to the electrical circuit analogues of Chapt. 1 - the powerful approach used in Mather's classic papers [49, 50, 51]. In this chapter, we keep the thermal-electrical differential equation formalism.

The two differential equations are complicated by several nonlinear terms. These nonlinear terms can be linearized in a small-signal limit around the steady-state values of resistance, temperature, and current: R_0, T_0, I_0. In the small-signal limit, we use steady-state values of heat capacity and thermal conductance. We describe the linearization of the power flow to the heat bath, the nonlinear TES resistance, and the Joule power dissipation, and then derive the linearized differential equations for current and temperature.

For the power flow to the heat bath, we assume a power-law dependence, which can be written as

$$P_{\mathrm{bath}} = K\left(T^n - T_{\mathrm{bath}}^n\right) \;, \tag{5}$$

where $n = \beta + 1$, β is the thermal conductance exponent defined in Chapt. 1, and the prefactor $K = G/n(T^{n-1})$, where the differential thermal conductance $G \equiv \mathrm{d}P_{\mathrm{bath}}/\mathrm{d}T$. Eqn. 5 can be expanded for small signals around T_0 as:

$$P_{\mathrm{bath}} \approx P_{\mathrm{bath}_0} + G\delta T \;, \tag{6}$$

where $G = nKT^{n-1}$ and $\delta T \equiv T - T_0$. The values of K and n are determined by the nature of the thermal weak link to the heat bath. Four experimentally relevant cases for TES detectors are described in detail in Sect. 3. (insulators such as silicon nitride, electron-phonon coupling, normal-metal links, and acoustic crystal mismatch). The steady-state power flow to the heat bath $P_{\mathrm{bath}_0} = P_{J_0} + P_0$, where the steady-state Joule power is $P_{J_0} = I_0^2 R_0$ and the steady-state signal power is P_0.

Similarly, for small signals, the resistance of the TES can be expanded around R_0, T_0, I_0 to first order as

$$R(T,I) \approx R_0 + \left.\frac{\partial R}{\partial T}\right|_{I_0} \delta T + \left.\frac{\partial R}{\partial I}\right|_{T_0} \delta I \;, \tag{7}$$

where $\delta I \equiv I - I_0$. Substituting the unitless logarithmic temperature sensitivity used in Chapt. 1,

$$\alpha_I \equiv \left.\frac{\partial \log R}{\partial \log T}\right|_{I_0} = \frac{T_0}{R_0}\left.\frac{\partial R}{\partial T}\right|_{I_0} \;, \tag{8}$$

and the current sensitivity

$$\beta_I \equiv \left.\frac{\partial \log R}{\partial \log I}\right|_{T_0} = \frac{I_0}{R_0}\left.\frac{\partial R}{\partial I}\right|_{T_0} \;, \tag{9}$$

the expression for the resistance is

$$R(T,I) \approx R_0 + \alpha_I \frac{R_0}{T_0}\delta T + \beta_I \frac{R_0}{I_0}\delta I \;. \tag{10}$$

This equation includes the dependence of the resistance of the TES on both the temperature and the electrical current (Chapt. 1). Some authors have defined α as a total derivative, incorporating the effect on the resistance when the current changes with temperature [40]. In that definition, α incorporates both temperature and current dependence. Here we use the partial derivative definition, and divide the temperature and current dependence into α_I and β_I.

It is useful to note that, from (10), the constant-temperature dynamic resistance of the TES is

$$R_{\mathrm{dyn}} \equiv \left. \frac{\partial V}{\partial I} \right|_{T_0} = R_0 \left(1 + \beta_I \right) . \tag{11}$$

The Joule power can also be expanded to first order around R_0, T_0, I_0 as

$$P_J = I^2 R \approx P_{J_0} + 2 I_0 R_0 \delta I + \alpha_I \frac{P_{J_0}}{T_0} \delta T + \beta_I \frac{P_{J_0}}{I_0} \delta I . \tag{12}$$

We also define the low-frequency loop gain under constant current,

$$\mathcal{L}_I \equiv \frac{P_{J_0} \alpha_I}{G T_0} , \tag{13}$$

and the natural thermal time constant (in the absence of electrothermal feedback),

$$\tau \equiv \frac{C}{G}. \tag{14}$$

We substitute (6), (10), (12), (13), and (14) into (3) and (4), substitute in the small-signal values for the state variables, $\delta T \equiv T - T_0$ and $\delta I \equiv I - I_0$, and drop second-order terms. The dc terms cancel and we arrive at the linearized differential equations:

$$\frac{\mathrm{d}\delta I}{\mathrm{d}t} = -\frac{R_L + R_0 \left(1 + \beta_I \right)}{L} \delta I - \frac{\mathcal{L}_I G}{I_0 L} \delta T + \frac{\delta V}{L} , \tag{15}$$

$$\frac{\mathrm{d}\delta T}{\mathrm{d}t} = \frac{I_0 R_0 \left(2 + \beta_I \right)}{C} \delta I - \frac{\left(1 - \mathcal{L}_I \right)}{\tau} \delta T + \frac{\delta P}{C} . \tag{16}$$

Here $\delta P \equiv P - P_0$ represents small-power signals around a steady-state power load P_0, and $\delta V \equiv V_{\mathrm{bias}} - V_0$ represents small changes in the voltage bias around the steady-state value V_0.

Two limiting cases of these equations can be directly integrated to give results that are used in the full solutions derived later. In the limit of $\mathcal{L}_I = 0$, (15) is independent of δT and can be integrated to give an exponential decay of current to steady state with the bias circuit electrical time constant

$$\tau_{\mathrm{el}} = \frac{L}{R_L + R_0 \left(1 + \beta_I \right)} = \frac{L}{R_L + R_{\mathrm{dyn}}} . \tag{17}$$

In the limit of $\delta I = 0$ (hard current bias), (16) can be integrated to give an exponential decay of temperature to steady state with the current-biased thermal time constant

$$\tau_I = \frac{\tau}{1 - \mathcal{L}_I} . \tag{18}$$

When $\mathcal{L}_I$ is larger than one, the current-biased thermal time constant τ_I is negative. As will be seen later, the negative time constant is indicative of instability due to thermal runaway.

These coupled differential equations have been solved both by using harmonic expansion [49, 50, 51, 47] and by using a change of variables by matrix diagonalization to uncouple the two equations. The harmonic expansion approach is necessary to evaluate the spectral dependence of the noise (Sect. 2.5). However, the change of variables approach, which has been used by Lindeman to study the TES differential equations [48], provides superior insight into the TES response. We adopt Lindeman's approach to calculating the current response. Substituting in (17), equations (15), (16) can be represented in a matrix format as

$$\frac{\mathrm{d}}{dt} \begin{pmatrix} \delta I \\ \delta T \end{pmatrix} = - \begin{pmatrix} \dfrac{1}{\tau_{\mathrm{el}}} & \dfrac{\mathcal{L}_I G}{I_0 L} \\ -\dfrac{I_0 R_0 \left(2 + \beta_I \right)}{C} & \dfrac{1}{\tau_I} \end{pmatrix} \begin{pmatrix} \delta I \\ \delta T \end{pmatrix} + \begin{pmatrix} \dfrac{\delta V}{L} \\ \dfrac{\delta P}{C} \end{pmatrix} . \tag{19}$$

The homogeneous form of (19) is found by taking δV and δP to zero. An appropriate change of variables decouples the two equations. Then, the differential equations can be directly integrated to find solutions in the form of exponentials. The solutions can be converted back to functions of T and I by an inverse change of variables. A conventional technique to accomplish this change of variables for coupled linear differential equations is to represent them in a matrix format and to diagonalize the matrix using its eigenvectors. The matrix has two eigenvectors, $\vec{v}_\pm$, with eigenvalues $\lambda_\pm$.

Consider two functions proportional to the two eigenvectors, $\vec{f}_\pm(t) = f_\pm(t)\, \vec{v}_\pm$. When these functions are substituted into the homogeneous form of (19), the equation reduces to

$$\frac{d}{dt} f_\pm(t) = -\lambda_\pm f_\pm(t) \;, \tag{20}$$

which can be directly integrated to give a full homogeneous solution

$$\begin{pmatrix} \delta I \\ \delta T \end{pmatrix} = A_+ e^{-\lambda_+ t}\, \vec{v}_+ + A_- e^{-\lambda_- t}\, \vec{v}_- \;, \tag{21}$$

where the prefactors $A_\pm$ are unitless constants.

The two eigenvalues of the 2×2 matrix in (19) are

$$\frac{1}{\tau_\pm} \equiv \lambda_\pm = \frac{1}{2\tau_{\mathrm{el}}} + \frac{1}{2\tau_I} \pm \frac{1}{2}\sqrt{\left(\frac{1}{\tau_{\mathrm{el}}} - \frac{1}{\tau_I}\right)^2 - 4\frac{R_0}{L}\frac{\mathscr{L}_I(2 + \beta_I)}{\tau}} \;, \tag{22}$$

where we define two time constants $\tau_\pm$ as the inverse eigenvalues. The two eigenvectors are

$$\vec{v}_\pm = \begin{pmatrix} \dfrac{1 - \mathscr{L}_I - \lambda_\pm \tau}{2 + \beta_I}\dfrac{G}{I_0 R_0} \\ 1 \end{pmatrix} \;. \tag{23}$$

We now present specific solutions of these equations for two important cases: a small delta-function impulse of energy, and a small sinusoidal power load at a given frequency.

In the case of a delta-function impulse (such as the absorption of a photon with instantaneous thermalization), the homogenous solution in (21) can be used with the values of the prefactors determined by the initial value of temperature change from the impulse $\delta T(0) = \delta T = E/C$ and initial quiescent current $\delta I(0) = 0$:

$$\begin{pmatrix} 0 \\ \delta T \end{pmatrix} = A_+ e^{-\lambda_+ t}\, \vec{v}_+ + A_- e^{-\lambda_- t}\, \vec{v}_- \;, \tag{24}$$

which makes it possible, using (23), to solve for the prefactors

$$A_\pm = \pm \delta T \frac{\dfrac{1}{\tau_I} - \lambda_\mp}{\lambda_+ - \lambda_-} \;. \tag{25}$$

Substituting (25) into (21) and (23) and using the time constants $1/\tau_\pm \equiv \lambda_\pm$ in place of the eigenvalues yields equations for the current and temperature for times $t > 0$,

$$\delta I(t) = \left(\frac{\tau_I}{\tau_+} - 1\right)\left(\frac{\tau_I}{\tau_-} - 1\right)\frac{1}{(2 + \beta_I)}\frac{C\delta T}{I_0 R_0 \tau_I^2}\frac{\left(e^{-t/\tau_+} - e^{-t/\tau_-}\right)}{(1/\tau_+ - 1/\tau_-)} \tag{26}$$

$$\delta T(t) = \left(\left(\frac{1}{\tau_I} - \frac{1}{\tau_+}\right)e^{-t/\tau_-} + \left(\frac{1}{\tau_I} - \frac{1}{\tau_-}\right)e^{-t/\tau_+}\right)\frac{\delta T}{(1/\tau_+ - 1/\tau_-)} \;, \tag{27}$$

which are valid for $t \geq 0$.

From the form of the current response $\delta I(t) \propto (e^{-t/\tau_+} - e^{-t/\tau_-})$ in (26), we identify the time constants as the "rise time" τ_+ and "fall time" τ_- (relaxation to steady state) after a delta-function temperature

13

impulse. Equations (26) and (27) are a complete solution for the response of a TES calorimeter to a small delta-function temperature impulse at time $t = 0$.

It is interesting to note that, when L is small so that $\tau_+ \ll \tau_-$, equation (22) reduces to

$$\tau_+ \rightarrow \tau_{\rm el}, \tag{28}$$

$$\tau_- \rightarrow \tau \frac{1 + \beta_I + R_L/R_0}{1 + \beta_I + R_L/R_0 + (1 - R_L/R_0)\mathscr{L}_I} = \tau_{\rm eff} \ , \tag{29}$$

which are the electrical time constant $\tau_{\rm el}$ of equation (17), and the effective thermal time constant of the bolometer in the case of zero bias-circuit inductance, $\tau_{\rm eff}$. As the two time constants approach each other, the poles interact, causing the rise and fall times of (22) to differ significantly from $\tau_{\rm el}$ and $\tau_{\rm eff}$.

A useful form of equation (26) is for the case where $\tau_+ = \tau_-$. Then, taking the limiting form of (26), the current reduces to

$$\delta I(t) = \left(\frac{\tau_I}{\tau_\pm} - 1\right)^2 \frac{1}{(2 + \beta_I)} \frac{C\delta T}{I_0 R_0 \tau_I^2} \left(-te^{-t/\tau_\pm}\right) \ . \tag{30}$$

As will be seen later, this solution is "critically damped," and is often chosen to optimize a tradeoff between energy resolution or noise-equivalent power and the required slew rate in the readout electronics.

We now proceed to determine the power-to-current responsivity of the TES. Usually, this is done by means of a harmonic expansion of (19) in a Fourier series [49, 47, 14]. Instead, we find these parameters by direct solution of the differential equation including an inhomogeneous sinusoidal drive term. This approach yields a useful and simple expression that clearly illustrates the dependence of the power-to-current responsivity on the rise and fall times of a delta-function pulse.

In the case of a small, sinusoidal power load $\delta P = \mathrm{Re}(\delta P_0 e^{i\omega t})$, the full solution to (19) can be found in the conventional manner of finding a particular solution including the inhomogeneous terms, and adding the homogenous solution (21). The particular solution must satisfy the real part of

$$\frac{d}{dt}\begin{pmatrix} \delta I \\ \delta T \end{pmatrix} = -\begin{pmatrix} \dfrac{1}{\tau_{\rm el}} & \dfrac{\mathscr{L}_I G}{I_0 L} \\ \dfrac{-I_0 R_0(2 + \beta_I)}{C} & \dfrac{1}{\tau_I} \end{pmatrix}\begin{pmatrix} \delta I \\ \delta T \end{pmatrix} + \begin{pmatrix} 0 \\ \dfrac{\delta P_0}{C} \end{pmatrix} e^{i\omega t} \ . \tag{31}$$

We look for a particular solution of the form

$$\vec{f}(t) = A_+ e^{i\omega t}\, \vec{v}_+ + A_- e^{i\omega t}\, \vec{v}_- \ , \tag{32}$$

that, when substituted into (31), results in

$$\begin{pmatrix} 0 \\ \dfrac{\delta P_0}{C} \end{pmatrix} = A_+\, \vec{v}_+ \left(i\omega + \lambda_+\right) + A_-\, \vec{v}_- \left(i\omega + \lambda_-\right) \tag{33}$$

Using the eigenvectors from (23), we solve for the prefactors

$$A_\pm = \mp \frac{\delta P_0}{C\tau} \frac{\lambda_\mp \tau + L_I - 1}{(\lambda_+ - \lambda_-)(\lambda_\pm + i\omega)} \tag{34}$$

A general solution consists of this particular solution added to (21). However, the particular solution has sufficient information to calculate responsivity (the current and temperature fluctuation amplitudes due to a power fluctuation amplitude). Substituting (34) into (32) using (23), and substituting the inverse rise and fall times for the eigenvalues, yields an expression for the responsivity of the TES at angular frequency ω:

$$s_I(\omega) = -\frac{1}{I_0 R_0} \frac{1}{(2 + \beta_I)} \frac{(1 - \tau_+/\tau_I)(1 - \tau_-/\tau_I)}{(1 + i\omega\tau_+)(1 + i\omega\tau_-)} \tag{35}$$

$$s_T(\omega) = \frac{1}{G} \frac{\tau_+ \tau_-}{\tau^2} \frac{(\tau/\tau_+ + \tau/\tau_- + \mathscr{L}_I - 1 + i\omega\tau)}{(1 + i\omega\tau_+)(1 + i\omega\tau_-)} \ . \tag{36}$$

14

Equations (35) and (36) are the power responsivity of a linear TES; the first is the power-to-current responsivity $s_I(\omega)$, and the second is the power-to temperature responsivity $s_T(\omega)$. Here we use a lower-case s for responsivity to avoid confusion with noise power spectral density, which is an upper-case S. $s_I(\omega)$ is one of the most important parameters for bolometric applications in which power levels are monitored rather than the energy impulses measured in calorimetry, since it allows measured currents to be referred back to input power signals. In this form, it rolls off at two poles associated with the rise and fall times of equation (22), including the pole-interaction effects. In the limit that the poles are widely separated and noninteracting, τ_+ and τ_- reduce to the electric and effective zero-inductance thermal time constants of equation (28) and (29).

Equation (35) can be usefully expressed in terms of the inductance L instead of the time constants $\tau_\pm$:

$$s_I(\omega) = -\frac{1}{I_0 R_0} \left(\frac{L}{\tau_{\mathrm{el}} R_0 \mathscr{L}_I} + \left(1 - \frac{R_L}{R_0} \right) + \right.$$
$$\left. i\omega \frac{L\tau}{R_0 \mathscr{L}_I} \left(\frac{1}{\tau_I} + \frac{1}{\tau_{\mathrm{el}}} \right) - \frac{\omega^2 \tau}{\mathscr{L}_I} \frac{L}{R_0} \right)^{-1} . \tag{37}$$

For a voltage bias case $(R_L \ll R_0)$ and strong feedback satisfying the condition

$$\mathscr{L}_I \gg \frac{R_l + R_0(1 + \beta_I)}{(R_0 - R_L)} , \tag{38}$$

the zero-frequency responsivity from (37) is simply

$$s_I(0) = -\frac{1}{I_0(R_0 - R_L)} , \tag{39}$$

and depends only on the bias circuit parameters. This result is discussed further in the next section.

The complex impedance, or the current response given a voltage excitation, can be computed in the same way as the responsivity was in equations (31) through (35). However, in this case it is more convenient to compute it by a harmonic expansion in a Fourier series [49, 40, 52, 53]. When a Thevenin-equivalent voltage signal with Fourier component V_ω is applied to the bias, each component, I_ω, of a Fourier-series expansion of the current in (19) satisfies

$$\begin{pmatrix} \dfrac{1}{\tau_{\mathrm{el}}} + i\omega & \dfrac{\mathscr{L}_I G}{I_0 L} \\ \dfrac{-I_0 R_0 (2 + \beta_I)}{C} & \dfrac{1}{\tau_I} + i\omega \end{pmatrix} \begin{pmatrix} I_\omega \\ T_\omega \end{pmatrix} = \begin{pmatrix} \dfrac{V_\omega}{L} \\ 0 \end{pmatrix} . \tag{40}$$

This formalism is frequently used to analyze the differential equations of coupled mechanical systems, and it has been used to extract the complex impedance of a TES [52]. The inverse of the matrix in (40) has been referred to as a "generalized responsivity matrix," because it contains both the current and temperature responses to a voltage or power input [53].

If we left-multiply both sides of the equation by the inverse of the matrix in (40), we arrive at a circuit complex impedance

$$Z_\omega = V_\omega / I_\omega = R_L + i\omega L + Z_{\mathrm{TES}} , \tag{41}$$

where the complex impedance of the TES alone is

$$Z_{\mathrm{TES}} = R_0(1 + \beta_I) + \frac{R_0 \mathscr{L}_I}{1 - \mathscr{L}_I} \frac{2 + \beta_I}{1 + i\omega \tau_I} . \tag{42}$$

It is also useful to derive the complex admittance of the full circuit,

$$Y(\omega) = s_I(\omega) I_0 \frac{\mathscr{L}_I - 1}{\mathscr{L}_I} (1 + i\omega \tau_I) , \tag{43}$$

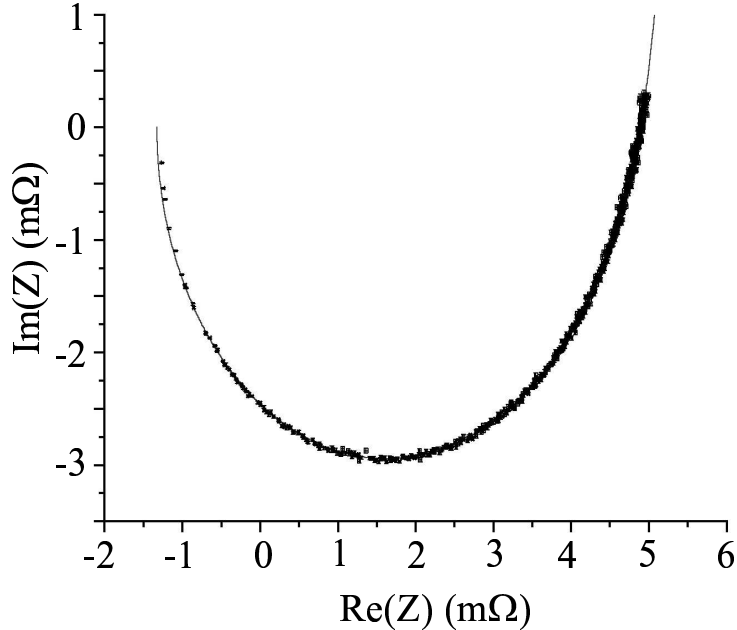where we have used the power-to-current responsivity $s_I(\omega)$ from (37).

15

Figure 4: The complex impedance of the bias circuit of a TES x-ray calorimeter measured at many different frequencies using a white noise source. The line is a fit of the data to $Z(\omega) = R_L + i\omega L + Z_{\text{TES}}(\omega)$ using the expression for $Z_{\text{TES}}(\omega)$ in (42). Figure courtesy of M. Lindeman, Univ. of Wisconsin.

The complex impedance is useful as an experimental probe of the linear circuit parameters of a TES [52]. It can be difficult to accurately extract these parameters from the observed detector response to optical signals. By measuring the detector response to voltage signals applied to the bias line, the complex impedance can be measured as a function of frequency. These data can be fit to (41), making it possible to extract the parameters $\beta_I, \mathscr{L}_I, \tau_I,$ and L. From these, using (18) and (14), C can also be extracted. An example of a fit to the measured complex impedance of a TES x-ray calorimeter is shown in Fig. 4.

2.4 TES Stability

The solution for the response of a TES can be either damped or oscillating, and it can be either stable or unstable [40, 48]. As will be seen in the next section, the desire for stable operation at high $\mathscr{L}_I$ was a historical motivation for introducing voltage-biased operation [13]. We now determine the constraints that these equations place on the operating parameters for stable operation.

If the time constants $\tau_\pm$ of equations (22) are real, the solution (26) is critically damped or overdamped (exponential, with no sinusoidal component). If they are complex, the response is underdamped (with a sinusoidal component), and if the real part is negative, the response is unstable, and signals grow over time.

From equation (22), the response of the calorimeter is overdamped if $\tau_+ < \tau_-$, and is critically damped if

$$\tau_+ = \tau_- . \tag{44}$$

Practically, this condition constrains the inductance in the bias circuit for damped response. Solving (22) and (44) for the inductance at critical damping, we arrive at

$$L_{\text{crit}\pm} = \left\{ \mathscr{L}_I \left(3 + \beta_I - \frac{R_L}{R_0} \right) + \left(1 + \beta_I + \frac{R_L}{R_0} \right) \pm \right.$$
$$\left. 2\sqrt{\mathscr{L}_I \left(2 + \beta_I \right) \left(\mathscr{L}_I \left(1 - \frac{R_L}{R_0} \right) + \left(1 + \beta_I + \frac{R_L}{R_0} \right) \right)} \right\} \frac{R_0 \tau}{\left(\mathscr{L}_I - 1 \right)^2} . \tag{45}$$

16

For zero and very large L, the response of the calorimeter is overdamped. The response is underdamped when

$$L_{\mathrm{crit}-} < L < L_{\mathrm{crit}+} \ . \tag{46}$$

Operating at or below $L_{\mathrm{crit}-}$ is most interesting for voltage-biased calorimeters, as operation at or above $L_{\mathrm{crit}+}$ reduces the temperature-to-current responsivity of the TES at frequencies of interest, leading to a degradation due to amplifier noise.

In the case of voltage-bias, where $R_L = 0$, and strong feedback, where $\mathscr{L}_I \gg 1, \beta_I$, equation (45) reduces to

$$\frac{L_{\mathrm{crit}\pm}}{R_0} = \left(3 + \beta_I \pm 2\sqrt{2 + \beta_I}\right) \frac{\tau}{\mathscr{L}_I} \ . \tag{47}$$

This equation, in turn, reduces to the criterion for $L_{\mathrm{crit}\pm}$ in the limit $\beta_I = 0$ [40]

$$\frac{L_{\mathrm{crit}\pm}}{R_0} = \frac{\tau}{\mathscr{L}_I} \left(3 \pm 2\sqrt{2}\right) \ . \tag{48}$$

The response of the calorimeter is stable and tends to relax back to steady-state over time when the real part of both time constants $\tau_{\pm}$ are positive. This is true when

$$\mathrm{Re} \left(\frac{1}{\tau_{\mathrm{el}}} + \frac{1}{\tau_I} - \sqrt{\left(\frac{1}{\tau_{\mathrm{el}}} - \frac{1}{\tau_I}\right)^2 - 4\frac{R_0}{L}\frac{\mathscr{L}_I(2 + \beta_I)}{\tau}} \right) > 0 \ . \tag{49}$$

Equation (49) can be simplified in both the overdamped and underdamped cases. If $\tau_+ < \tau_-$, the TES is overdamped, and equation (49) becomes

$$\frac{1}{\tau_{\mathrm{el}}} + \frac{1}{\tau_I} > \sqrt{\left(\frac{1}{\tau_{\mathrm{el}}} - \frac{1}{\tau_I}\right)^2 - 4\frac{R_0}{L}\frac{\mathscr{L}_I(2 + \beta_I)}{\tau}} \ . \tag{50}$$

Substituting in (17) for the electrical time constant, this equation reduces to

$$R_0 > \frac{(\mathscr{L}_I - 1)}{(\mathscr{L}_I + 1 + \beta_I)} R_L \ . \tag{51}$$

Equation (51) is the criterion for stability of an overdamped TES. It places a constraint on the value of the Thevenin-equivalent load resistor R_L to prevent thermal runaway from positive feedback if $\mathscr{L}_I$ is greater than one. It is automatically satisfied when $R_0 > R_L$, so a simple, linear, voltage-biased TES is always stable when it is over- or critically damped.

In the underdamped case, the real part of the square root in (49) vanishes, and the TES is stable when

$$\tau > (\mathscr{L}_I - 1)\, \tau_{\mathrm{el}} \ , \tag{52}$$

or, equivalently, when

$$\mathscr{L}_I \leq 1, \quad \text{or} \ \ \mathscr{L}_I > 1 \ \text{and} \ L < \frac{\tau}{\mathscr{L}_I - 1} \left\{ R_L + R_0 \left(1 + \beta_I\right) \right\} \ . \tag{53}$$

Equation (52), and equivalently equation (53), represents the criterion for stability of an underdamped TES. It constrains how large the inductance can be (or how fast the detector response can be) before the onset of unstable electrothermal oscillations that grow over time. If a TES is critically damped, conditions (51), (52), and (53) are equivalent.

2.5 Negative electrothermal feedback

In the previous two sections, we developed the equations for the response and stability of a linear TES with arbitrary R_L. We now further discuss the effect of the value of R_L on the characteristics of the TES,

considering in detail the important special case of strong negative electrothermal feedback: voltage bias ($R_L \ll R_0$) and high low-frequency constant-current "loop gain" ($\mathscr{L}_I \gg 1, \beta_I$). In this limit, there are significant simplifications and operational advantages, including stable operation with high $\mathscr{L}_I$, reduced sensitivity to TES parameter variation (making it possible to operate large arrays of TES devices), faster response time, self-biasing, and self-calibration.

The thermal and electrical circuits of a TES interact due to the cross-terms in the thermal-electrical differential equations (15) and (16). A temperature signal in a TES is transduced into an electrical current signal by the change in the resistance of the TES. In turn, the electrical current signal in the TES is fed back into a temperature signal by Joule power dissipation in the TES. This "electrothermal feedback" (ETF) process is analogous to electrical feedback in a transistor circuit. And, as in a transistor circuit, feedback can be either positive or negative.

In a TES, α_I is positive, so the resistance of the TES increases as the temperature increases. Under current-bias conditions ($R_L \gg R_0$), as the temperature and resistance increase, the Joule power, $P_J = I^2 R$, increases as well, and the ETF is positive. Under voltage-bias conditions ($R_0 \gg R_L$), the Joule power, $P_J = V^2/R$, decreases with increasing temperature, and electrothermal feedback is negative. When the load is matched ($R_0 = R_L$) the Joule power is independent of temperature for small changes in R, and there is no electrothermal feedback.

There are significant advantages to using negative feedback in transistor circuits, and many of these advantages apply to TES circuits as well. When operated with positive feedback, an amplifier can easily become unstable. High-gain transistor amplifiers tend to have non-negligible variation in intrinsic parameters including the open-loop gain. When negative feedback is used, the (closed-loop) gain is determined by the extrinsic parameters of the bias circuit instead of the amplifier itself, making circuit performance more uniform and reproducible. Furthermore, negative feedback linearizes the detector response and increases the dynamic range.

When voltage biased, a TES is stable against thermal runaway even at high $\mathscr{L}_I$. As the temperature is increased, the reduction in Joule power acts as a restoring force. From (51), a damped (overdamped or critically damped) TES is stable when $R_0 > R_L$. In contrast, in a current-biased TES ($R_L \gg R_0$), an increase in temperature results in increased Joule power. From (51), a damped, current-biased TES is stable from thermal runaway only when $\mathscr{L}_I \leq 1$, seriously restricting the range of available operational parameters. However, even a voltage-biased TES can sometimes be unstable due to growing electrothermal oscillations. Just as in an amplifier, unstable oscillations occur when the "loop gain" is above unity at a frequency where the phase shift in the feedback signal is larger than $180\,^\circ$. The condition to avoid unstable oscillations is (52).

Another attractive feature of a voltage-biased TES is that, over a certain range of signal power and bias voltage, it self-biases in temperature within its transition. This feature is important for array applications. If multiple pixels in an array have superconducting phase transition regions that do not overlap in temperature, it is impossible to bias them all at the same temperature. However, if they are voltage biased, and the bath temperature is much lower than the transition temperature, the Joule power dissipation in each pixel causes it to self-heat to within its respective phase transition. When the bath temperature is well below the transition temperature, the TES performance is also less sensitive to fluctuations in the bath temperature, easing the requirements for temperature stability.

Negative feedback generally increases the bandwidth of an electrical system. This is also true for TES detectors. As is evident in equation (22) and more clearly in (29), if a TES is voltage biased, for high $\mathscr{L}_I$ the thermal relaxation time $\tau_- \propto \mathscr{L}_I^{-1}$. In the strong feedback limit, $\tau_- \ll \tau$. Negative feedback has been experimentally shown to speed up the pulse fall time of a TES by more than two orders of magnitude. While the feedback speeds up the response time, when other parameters are held fixed, it does not increase the signal-to-noise ratio at any frequency, so that it does not itself improve the energy resolution. However, it does increase the useful count rate. If multiple small pulses arrive within several effective time constants of each other, it can be difficult to deconvolve the two signals without a loss in energy resolution. More importantly, if multiple pulses drive the TES out of its linear range (or into saturation), degradation in energy resolution is unavoidable. As a result, pulse pileup is normally vetoed. Thus, negative feedback can lead to dramatic increases in useful bandwidth. Another advantage of a voltage bias is that it makes it possible to use a higher $\mathscr{L}_I$ than a current biased TES without thermal runaway, so it provides more flexibility in the choice of design parameters. This flexibility may make it possible to design a sensor with

better energy resolution.

The low-frequency power-to-current responsivity $s_I(0)$ of a TES is, in general, dependent on the intrinsic TES parameters including $\alpha_I, \beta_I, \mathscr{L}_I$ and R_0. There can be large pixel-to-pixel variation in intrinsic TES parameters across an array due to slightly different T_c, transition width, and magnetic field environment. However, as shown in equation (39), the low-frequency responsivity of a TES in the strong negative ETF limit is simply $s_I = -1/(I_0(R_0 - R_L))$, where the steady-state voltage across the TES is $V_{\mathrm{TES}} = I_0 R_0$. The low-frequency responsivity is a function solely of the steady-state bias voltage and the load resistance, and independent of the intrinsic TES parameters, making the response of many pixels across an array more uniform and reproducible than in the current-bias case. This simplification is a consequence of conservation of energy. For negative ETF with high $\mathscr{L}_I$, the temperature change approaches zero. Thus, the low-frequency power coming into a TES must approach the reduction in the Joule power due to ETF for small δI :

$$\delta P_{\mathrm{ETF}} = -I_0(R_0 - R_L)\delta I, \tag{54}$$

resulting in the responsivity of equation (39).

We have shown that the low-frequency current responsivity of a TES bolometer in the strong ETF limit is self-calibrating (i.e., it is a function only of the extrinsic bias circuit parameters). The energy pulses in a TES calorimeter are similarly self-calibrating. During a current pulse, the energy removed from a calorimeter by electrothermal feedback (i.e., by a reduction in the bias power from the steady-state value) is

$$E_{\mathrm{ETF}} = -\int_0^\infty V_{\mathrm{TES}}(t)\delta I(t)dt . \tag{55}$$

The voltage across the TES is

$$V_{\mathrm{TES}}(t) = V - (I_0 + \delta I(t))R_L - L\frac{d\delta I(t)}{dt} , \tag{56}$$

where $\delta I(t)$ is negative and I_0 is positive.

When (56) is substituted into (55), the inductive term goes to zero on integration since the energy stored in the inductor is the same before and after a pulse:

$$\int_0^\infty L\delta I(t)\frac{d}{dt}\delta I(t)dt = \frac{L}{2}\delta I(\infty)^2 - \frac{L}{2}\delta I(0)^2 = 0. \tag{57}$$

The pulse energy removed by electrothermal feedback is thus

$$E_{\mathrm{ETF}} = (I_0 R_L - V)\int_0^\infty \delta I(t)dt + R_L \int_0^\infty \delta I(t)^2 dt , \tag{58}$$

which is independent of the inductance of the bias circuit. In the strong-feedback limit, the pulse fall time $\tau_- \ll \tau$, so the energy in the pulse must approach E_{ETF} by conservation of energy.

Equations (54) and (58) are frequently used to make initial estimates of power and energy in TES bolometers and calorimeters. However, detailed detector calibration is used for most real applications. This is necessary because $\mathscr{L}_I$ is finite and errors of parts in a thousand are often important. However, the increased uniformity between pixels due to the voltage bias is important for array applications.

2.6   Thermodynamic noise

Like all physical systems with dissipation, the response of a TES is affected by thermodynamic fluctuations of its state variables. In this section, we present an analysis of these thermodynamic noise sources. The thermodynamic fluctuations associated with an electrical resistance are referred to as Johnson or Nyquist noise, and the thermodynamic fluctuations associated with a thermal impedance are often referred to as phonon noise or thermal fluctuation noise (TFN). These noise sources set fundamental limits on the noise equivalent power and energy resolution of a TES. Additional noise sources degrade the performance of a TES from these fundamental limits. These extra noise sources include quantum fluctuations (which are usually negligible in a TES), fluctuations in the superconducting order parameter, flux motion, and thermodynamic

fluctuations due to hidden state variables internal to the sensor, such as poorly-coupled heat capacity. In this section, we discuss the fundamental thermodynamic noise sources assuming no internal hidden variables (i.e., assuming Markovian noise processes). In Sect. 2.7, we discuss other noise sources.

When the power and voltage signals in the coupled differential equations (15) and (16) are stochastic forces determined by correlations in the state variables due to thermodynamic fluctuations, the differential equations are referred to as Langevin equations. The Langevin equations describe the response of the state variables to these fictional random forces. The thermodynamic noise can be analyzed by applying the Fluctuation-Dissipation Theorem (FDT) to these Langevin equations. However, to properly apply the FDT, it is important to identify the conjugate forces associated with the state variables.

In the electrical differential equation, the current I is the state variable (the "velocity" term in the Lagrangian), and the voltage V is the associated conjugate force. It can be seen that V is the conjugate force by imagining a resistor in a simple circuit with an ideal linear inductor L. The circuit is connected to a heat bath at a fixed temperature, so fluctuations in the current follow the canonical, or "Gibbs" distribution. The free energy is the energy stored in the inductor, $F = LI^2/2$. The conjugate momentum is thus $p = \partial F/\partial I = LI$ and the conjugate force is $dp/dt = LdI/dt = V$.

In the formalism of thermodynamics that we use here, the temperature T is allowed to fluctuate, and is considered to be the state variable [54, 55] (in some formalisms, temperature is defined as an equilibrium quantity that does not fluctuate [56]). The heat capacity of the TES is connected through a thermal conductance to a heat bath at a fixed temperature, so the canonical distribution also applies to the thermal circuit. Thus, when heat dQ flows between the heat bath and the bolometer, the free energy change is [54] $dF = -SdT$, where S is the entropy, and the conjugate momentum is $p = \partial F/\partial T = -S$. The heat flowing to the thermal circuit is $dQ = TdS$, so the conjugate force is $dp/dt = -(1/T)dQ/dT = -P/T$. The sign of the random power is arbitrary; here we use P/T as the conjugate force.

When analyzing coupled Langevin equations with the FDT, it is convenient to represent the Langevin equations as an "impedance" matrix Z connecting the vector of the state variables (the "velocity" vector) to the conjugate force vector. Then the Langevin equations are represented as

$$Z \begin{pmatrix} I_\omega \\ T_\omega \end{pmatrix} = \begin{pmatrix} V_\omega \\ \dfrac{P_\omega}{T_0} \end{pmatrix} . \tag{59}$$

In equation (40), we presented a matrix for the coupled TES differential equations that is similar to the impedance matrix, but that does not use the conjugate forces. Converting (40) to the conjugate forces in (59), we arrive at an impedance matrix:

$$Z_{\text{ext}} = \begin{pmatrix} \left(\dfrac{1}{\tau_{\text{el}}} + i\omega \right) L & \dfrac{\mathscr{L}_I G}{I_0} \\ (-I_0 R_0 (2 + \beta_I)) \dfrac{1}{T_0} & \left(\dfrac{1}{\tau_I} + i\omega \right) \dfrac{C}{T_0} \end{pmatrix} . \tag{60}$$

This equation was derived assuming that the Joule power dissipation in the TES is $P_J = IV_{\text{TES}} = I^2 R$, where $V_{\text{TES}} = IR$ (see equation 12). In equation (60), any fluctuating voltage (such as Johnson noise) changes the current, and thus does work on the TES. However, work done by the bias current on the fluctuating voltage is not included in this expression for P_J. Any power dissipated inside this voltage source is dissipated externally (the heat sink of the voltage source does not connect to the thermal circuit of the TES). Here we refer to this impedance matrix as the "external" impedance matrix Z_{ext}.

However, work done on a voltage source internal to the TES, such as work done on a Johnson noise voltage or a thermoelectric voltage, should cause power dissipation in the thermal circuit of the TES. The power dissipation is thus $P_J = IV_{\text{TES}}$, where $V_{\text{TES}} = IR + V_{\text{noise}}$ includes the fluctuating noise voltage. Work that is done on a Johnson noise voltage source can be either positive or negative.

In previous work with the TES differential equations [49, 47, 48], power dissipation due to work done on internal voltage noise sources was accounted for by adding an extra power term in the fictional random force vector on the right-hand side of (59). We instead include this power in the matrix on the left-hand side. The two approaches are mathematically equivalent, but the latter allows the straightforward derivation of the internal impedance matrix Z_{int} (which properly accounts for power dissipation in internal voltage

sources). The derivation of Z_{int} allows a more direct consideration of the noise using the fluctuation-dissipation theorem.

To account for the work done on an internal voltage source, we replace equation (12) with the following expression for the Joule power dissipation in the TES:

$$P_J = IV_{\text{TES}} = I(IR + V_{\text{noise}}) = I\left(V_{\text{bias}} - IR_L - L\frac{dI}{dt}\right) , \tag{61}$$

where, on the right hand side of (61), we have used the fact that the total voltage around the loop in the bias circuit is zero. Unlike equation (12), equation (61) describes Joule power dissipation equal to the full dissipation in the circuit, except for the dissipation in the load resistor. In (61), work done by the bias current on a Johnson noise voltage source in the TES leads to Joule power dissipation in the sensor. Equation (61) can be Taylor expanded for small δI around I_0:

$$P_J = I_0^2 R_0 + I_0(R_0 - R_L)\delta I - I_0 L\frac{d\delta I}{dt} , \tag{62}$$

and harmonically expanded:

$$P_J(\omega) = (I_0(R_0 - R_L) - i\omega LI_0)I_\omega . \tag{63}$$

When inserted into equation (16) in the place of (12), we arrive at

$$Z_{\text{int}} = \begin{pmatrix} \left(\dfrac{1}{\tau_{\text{el}}} + i\omega\right)L & \dfrac{\mathscr{L}_I G}{I_0} \\ (I_0(R_L - R_0) + i\omega LI_0)\dfrac{1}{T_0} & \left(\dfrac{1}{\tau} + i\omega\right)\dfrac{C}{T_0} \end{pmatrix} , \tag{64}$$

where the coupled thermal-electrical differential equations become

$$Z_{\text{int,ext}}\begin{pmatrix} I_\omega \\ T_\omega \end{pmatrix} = \begin{pmatrix} V_{\text{int,ext}_\omega} \\ \dfrac{P_\omega}{T_0} \end{pmatrix} . \tag{65}$$

At equilibrium, the impedance matrix determines the correlations in the thermodynamic fluctuations of the state variables. In fact, any impedance Z that connects a state variable to a conjugate force in a physical system causes correlations in the state variable if Z has a non-zero real component. By the fluctuation-dissipation theorem, at equilibrium and when quantum fluctuations are small, the power spectral density of the fluctuations in the state variable u is [57]

$$S_u(\omega) = 4k_{\text{B}}T\,\text{Re}\{Y(\omega)\} \tag{66}$$

where $Y(\omega) \equiv Z^{-1}(\omega)$ is the admittance. These correlations can be considered to be caused by a fictional random force F with power spectral density [57]

$$S_F(\omega) = 4k_{\text{B}}T\,\text{Re}\{Z(\omega)\} . \tag{67}$$

The corresponding matrix form of (66) is [58]

$$S_{u_i}(\omega) = 4k_{\text{B}}T\,\text{Re}\{Y_{ii}(\omega)\} , \tag{68}$$

where i is the vector index, and the power spectral density of the fluctuations in the velocity variable u_i is determined by the corresponding diagonal element of the admittance matrix Y_{ii}.

It is tempting to apply the matrix form of the fluctuation-dissipation theorem directly to the impedance matrix in (64). However, the predictions from this process are not consistent with experimental results. The problem arises from the fact that this simple FDT is rigorous only when applied to linear circuits at thermodynamic equilibrium. The Langevin equations may be at steady state, but as long as there is a non-zero bias current the temperature is not equal to the bath temperature, and the system is not at equilibrium. Then, the direct application of (68) gives misleading results.

It is conventional (but not rigorous) to use a simplifying ansatz that we refer to here as the linear equilibrium ansatz (LEA). This ansatz, introduced for the analysis of bolometers by Mather [49], asserts that the fictional random forces predicted by the fluctuation-dissipation theorem at equilibrium (when the current is zero) and with linear elements (i.e. ignoring both the current- and temperature- dependence of the resistance) is the same as the fictional random forces that determine the fluctuations in the state variables outside of equilibrium and with nonlinear resistors. Usually the LEA is implicitly assumed without discussion. The LEA is equivalent to the commonly used component-level resistor noise model that associates a random voltage with power spectral density (PSD) $S_V = 4k_BTR$ in series with each resistor R, or a Thevenin-equivalent random current PSD $S_I = 4k_BT/R$ in parallel with each resistor, independent of the bias circuit. At equilibrium ($I_0 = 0$) in the linear limit ($\beta_I = 0$), the real parts of both (60) and (64) reduce to

$$\text{Re}\left\{Z_{\text{int,ext}}\right\} = \begin{pmatrix} R_0 + R_L & 0 \\ 0 & \dfrac{G}{T_0} \end{pmatrix} . \tag{69}$$

Then, by the fluctuation-dissipation theorem (67), the power spectral densities of the fictional random forces are determined by the diagonal elements of the equilibrium impedance matrix matrix (69):

$$\begin{pmatrix} S_V \\ \dfrac{S_{P_{\text{TFN}}}}{(T_0)^2} \end{pmatrix} = 4k_BT_0 \begin{pmatrix} R_0 + R_L \\ \dfrac{G}{T_0} \end{pmatrix} . \tag{70}$$

Here $S_V = S_{V_{\text{TES}}} + S_{V_L}$, $S_{V_{\text{TES}}} = 4k_BT_0R_0$ is the Nyquist noise voltage of the TES, $S_{V_L} = 4k_BT_0R_L$ is the Nyquist noise voltage of the load resistor, and $S_{P_{\text{TFN}}} = 4k_BT_0^2G$ is the thermal fluctuation noise across the thermal conductance G. More generally, if the temperature of the load resistor T_L and the temperature of the heat bath T_{bath} are allowed to vary from T_0, the LEA predicts $S_{V_{\text{TES}}} = 4k_BT_0R_0$, $S_{V_L} = 4k_BT_LR_L$, and $S_{P_{\text{TFN}}} = 4k_BT_0^2G \times F(T_0, T_{\text{bath}})$, where the form of the unitless function $F(T_0, T_{\text{bath}})$ depends on the thermal conductance exponent and on whether phonon reflection from the boundaries is specular or diffuse. $F(T_0, T_{\text{bath}})$ is defined as a function of the temperature of the TES, and typically lies between 0.5 and 1 [49, 59]. In Chapt. 1, the function $F_{\text{LINK}}(T_{\text{bath}}, n)$ was defined as a function of the bath temperature. $F(T_0, T_{\text{bath}})$ can be derived from the results in Chapt. 1 by $F(T_0, T_{\text{bath}}) = F_{\text{LINK}}(T_{\text{bath}}, n)(T_{\text{bath}}/T_0)^{n+1}$. The random forces can be combined with (65) to determine the power spectral density of the fluctuations in the state variables.

The LEA assumes a linear resistor with no temperature dependence ($\alpha_I = 0$) or current dependence ($\beta_I = 0$) for the determination of the random voltage across the resistor. In reality, both current-dependent and temperature-dependent nonlinearity will change the random noise voltage across the resistor. Here we consider a modification to the LEA that approximately incorporates the affects of a current-dependent resistance but that still does not incorporate the effect of a temperature-dependent resistance. The analysis of noise in circuits with current-dependent nonlinearity ($\beta_I \neq 0$) is complicated by several factors. The Thevenin theorem does not apply to circuits with nonlinear elements. Thus, component-level noise models with a series voltage noise source do not have a "Thevenin-equivalent" parallel current noise source. Further, nonlinear resistors have non-Gaussian noise [60], so the Fokker-Planck equation, which has a Gaussian steady-state solution, cannot be used in the analysis.

Here we introduce a more general ansatz that we refer to as the nonlinear equilibrium ansatz (NLEA). The NLEA is equivalent to the LEA, except that it allows the resistor to have current-dependent nonlinearity, with $\beta_I \neq 0$. The noise is still determined assuming a system near equilibrium, except that the values of β_I and R_0 are determined at the steady-state bias current, I_0. The dependence of the power spectral density of the voltage noise on nonlinearity can be written as

$$S_{V_{\text{TES}}} = 4k_BT_0R_0\xi(I_0) , \tag{71}$$

where $\xi(I)$ (unrelated to the superconducting coherence length) can be expressed as a Taylor expansion:

$$\xi(I) = 1 + \left.\frac{d\xi}{dI}\right|_{I=0} I + \mathcal{O}(I^2) . \tag{72}$$

In the linear approximation or $\xi(I_0) = 1$, the NLEA reduces to the LEA.

The noise is Markovian if the real part of the load impedance in the bias circuit is frequency independent. Then, the nonlinear Markov fluctuation-dissipation relations can be used to analyze the first-order term of $\xi(I)$. The quadratic Markov fluctuation-dissipation relations have been used to consider a quadratic nonlinear resistor in a closed loop with an inductor L and a nonzero bias current I [61, 55]. We determine the value of $d\xi/dI$ in the quadratic approximation by fitting the TES resistance to a quadratic resistor with the same $R_0 \equiv V/I$ and β_I at the steady-state bias point. The quadratic V-I relationship is:

$$V = rI + \frac{1}{2}\gamma I^2, \tag{73}$$

where the resistance R_0 approaches the value r for low current, and γ is a constant quantifying the nonlinearity. In this case, the nonlinear Markov fluctuation-dissipation relations [61, 55] give a voltage noise power spectral density (PSD):

$$S_V = 4k_{\mathrm{B}}T\left(r + \frac{3}{2}\gamma I + \mathscr{O}(I^2)\right). \tag{74}$$

From (73), the resistance

$$R_0 \equiv \frac{V}{I} = r + \frac{1}{2}\gamma I, \tag{75}$$

and from (75),

$$\beta_I \equiv \frac{I}{R}\frac{dR}{dI} = \gamma\frac{I}{2R_0}. \tag{76}$$

Substituting (75) and (76) into (74), we have

$$S_V = 4k_{\mathrm{B}}TR_0(1 + 2\beta_I + \mathscr{O}(I^2)), \tag{77}$$

so we find that $d\xi/dI = 2\beta_I/I$ when all terms above the quadratic are dropped.

It is also instructive to consider the case of a resistor with a quadratic conductance. The quadratic conductance is

$$I = gV + \frac{1}{2}\gamma V^2, \tag{78}$$

where the conductance $G \equiv I/V = 1/R_0$ approaches the value g for low current, and γ is a constant quantifying the nonlinearity. If a quadratic conductor is biased in parallel with a capacitor, the nonlinear Markov fluctuation-dissipation relations [61, 55] give a parallel current noise PSD:

$$S_I = 4k_{\mathrm{B}}T\left(g + \frac{1}{2}\gamma V + \mathscr{O}(V^2)\right). \tag{79}$$

From (78), the conductance

$$G \equiv \frac{I}{V} = g + \frac{1}{2}\gamma V. \tag{80}$$

Substituting (80) into (79), and using $G = 1/R_0$, we have

$$S_I = \frac{4k_{\mathrm{B}}T}{R_0} + \mathscr{O}(V^2). \tag{81}$$

In the current-biased circuit, the parallel current source (81) is equivalent to a voltage source in series with the resistor with noise

$$S_V = \frac{4k_{\mathrm{B}}T}{R_0}\left(\frac{dV}{dI}\right)^2 + \mathscr{O}(V^2) = \frac{4k_{\mathrm{B}}T}{R_0}R_{\mathrm{dyn}}^2 + \mathscr{O}(V^2). \tag{82}$$

Using (11) for R_{dyn}, we have

$$S_V = 4k_{\mathrm{B}}TR_0(1 + \beta_I)^2 + \mathscr{O}(V^2) = 4k_{\mathrm{B}}TR_0(1 + 2\beta_I + \beta_I^2) + \mathscr{O}(V^2). \tag{83}$$

Thus, the model of a quadratic resistor with a series voltage noise source (77) or that for a quadratic conductor with a parallel current noise source (81) are consistent with each other to order I, with $d\xi/dI = 2\beta_I/I$.

In this work, we use the NLEA, which reduces to the conventional LEA used by Mather in the linear approximation $\xi(I_0) = 1$. In the NLEA, the use of $\xi(I_0) > 1$, such as the quadratic approximation of $\xi(I_0) = 1 + 2\beta_I$, may explain some of the excess noise observed in TES devices (Sect. 2.7). However, two caveats are in order. First, the noise of a nonlinear resistor is non-Gaussian, so the final uncertainty in the measurement of power or energy is also non-Gaussian. Due to the nonlinearity, the probability distribution is not subject to the usual Fokker-Planck stochastic diffusion equation. Instead, the fluctuation-relaxation process is described by a differential equation with a third derivative, leading to a non-Gaussian current distribution. In the balance of this chapter, we ignore the non-Gaussian nature of the noise in computing the energy resolution and noise-equivalent power (NEP). A more complete solution would require propagating the non-Gaussian distribution through the detector response functions.

A second caveat is that, even if the resistor is linear, we are still using an ansatz, and a full nonlinear, nonequilibrium thermodynamic analysis of the problem is required for a rigorous solution. Close to equilibrium, the full noise can be determined by the application of the nonlinear Markov fluctuation-dissipation relations to the coupled Langevin equations. This process shows that, near equilibrium, the magnitude of the white random force S_V depends on the temperature-dependent nonlinearity α_I as well as the current-dependent nonlinearity β_I. Further away from equilibrium, where a TES normally operates, the fluctuation-dissipation theorem can not provide a unique solution. In fact, there is no general formula connecting the response and dissipation at a nonequilibrium steady state to the noise. A more detailed model of the dissipative processes in the TES is required for a full solution of the correlations in the state variables far from equilibrium.

The thermal conductance $G(T)$ is dependent on the temperature, so it is nonlinear in the same way as a current-dependent $R(I)$. We thus expect a nonlinear contribution to the TFN. Near equilibrium, this nonlinear noise term can also be analyzed using the nonlinear Markov fluctuation-dissipation relations. Here we assume that the correction to the power spectral density of the TFN due to nonlinear thermal conductance is properly included in the factor $F(T_0, T_{\text{bath}})$. However, the TFN is non-Gaussian due to the nonlinear thermal conductance; a rigorous analysis would use a fluctuation-relaxation equation with higher-order terms than are included in the Fokker-Planck stochastic diffusion equation for the computation of the TFN as well as the Johnson noise.

The power spectral density of the current noise due to both internal and external noise voltages can be found by using (65) to determine the internal and external admittance of the circuit. By using the internal form of the impedance matrix (64), we determine the internal admittance

$$Y_{\text{int}}(\omega) \equiv \frac{I(\omega)}{V_{\text{int}}(\omega)} = -s_I(\omega)I_0 \frac{1}{\mathscr{L}_I}(1 + i\omega\tau) \,. \tag{84}$$

By using the external form of the impedance matrix (60), we determine the external admittance,

$$Y_{\text{ext}}(\omega) \equiv \frac{I(\omega)}{V_{\text{ext}}(\omega)} = s_I(\omega)I_0 \frac{\mathscr{L}_I - 1}{\mathscr{L}_I}(1 + i\omega\tau_I) \,, \tag{85}$$

which is the same as the complex admittance of (43).

The noise sources that we consider in this section fall into the categories of external voltage noise with power-spectral density $S_{V_{\text{ext}}}(\omega)$, internal voltage noise $S_{V_{\text{int}}}(\omega)$, power noise due to thermal fluctuation noise $S_{P_{\text{TFN}}}(\omega)$, and amplifier current noise $S_{I_{\text{amp}}}$. If these four types of noise sources are uncorrelated, the overall current noise in a TES can be written

$$\begin{aligned} S_I(\omega) = &S_{V_{\text{ext}}}(\omega)|Y_{\text{ext}}(\omega)|^2 + S_{V_{\text{int}}}(\omega)|Y_{\text{int}}(\omega)|^2 + \\ &S_{P_{\text{TFN}}}(\omega)|s_I(\omega)|^2 + S_{I_{\text{amp}}}(\omega) \,, \end{aligned} \tag{86}$$

and the overall power-referred noise in the TES is:

$$S_P(\omega) = \frac{S_I(\omega)}{|s_I(\omega)|^2} \,. \tag{87}$$

24

These expressions are used in computing the limit on the energy resolution of the calorimeter in the next section.

We now compute both the current-referred and the power-referred noise from four important noise sources in the TES: the Johnson noise in the TES, the Johnson noise in the load resistor, the thermal fluctuation noise, and the amplifier noise. The power spectral density of the current noise due to Johnson noise voltages in the TES can be found by substituting (71) into (84):

$$S_{I_{\mathrm{TES}}}(\omega) = 4k_{\mathrm{B}}T_0 R_0 \xi(I_0) \left| Y_{\mathrm{int}}(\omega) \right|^2 \ , \tag{88}$$

or

$$S_{I_{\mathrm{TES}}}(\omega) = 4k_{\mathrm{B}}T_0 I_0^2 R_0 \frac{\xi(I_0)}{\mathscr{L}_I^2}(1+\omega^2\tau^2)|s_I(\omega)|^2 \ , \tag{89}$$

where $s_I(\omega)$ is the power-to-current responsivity of (35). The TES Johnson noise referred to a power noise is then

$$S_{P_{\mathrm{TES}}}(\omega) = \frac{S_{I_{\mathrm{TES}}}(\omega)}{|s_I(\omega)|^2} = 4k_{\mathrm{B}}T_0 I_0^2 R_0 \frac{\xi(I_0)}{\mathscr{L}_I^2}(1+\omega^2\tau^2) \ . \tag{90}$$

Similarly, the power spectral density of the current noise due to Johnson noise voltages in the load resistor can be found from (85):

$$S_{I_{\mathrm{L}}}(\omega) = 4k_{\mathrm{B}}T_L I_0^2 R_L \frac{(\mathscr{L}_I - 1)^2}{\mathscr{L}_I^2}(1+\omega^2\tau_I^2)|s_I(\omega)|^2 \ . \tag{91}$$

When referred to a power noise, (91) is

$$S_{P_{\mathrm{L}}}(\omega) = 4k_{\mathrm{B}}T_L I_0^2 R_L \frac{(\mathscr{L}_I - 1)^2}{\mathscr{L}_I^2}(1+\omega^2\tau_I^2) \ . \tag{92}$$

We already determined that the thermal fluctuation noise is

$$S_{P_{\mathrm{TFN}}} = 4k_{\mathrm{B}}T_0^2 G \times F(T_0, T_{\mathrm{bath}}) \ , \tag{93}$$

which means that the current-noise fluctuations due to thermal fluctuation noise are

$$S_{I_{\mathrm{TFN}}}(\omega) = 4k_{\mathrm{B}}T_0^2 G \times F(T_0, T_{\mathrm{bath}})|s_I(\omega)|^2 \ . \tag{94}$$

A final noise term that is routinely encountered in an ideal linear TES is the noise of the SQUID amplifier. SQUID amplifiers have both noise referred to an input current and voltage noise due to the back action of the SQUID. Correlations in these two noise sources are important. Fortunately, for TES applications, the impedance of the TES is generally much higher than the noise impedance of the SQUID. Thus, we can neglect the correlated voltage noise terms. The current-referred amplifier noise is $S_{I_{\mathrm{amp}}}(\omega)$, which makes the power-referred amplifier noise

$$S_{P_{\mathrm{amp}}}(\omega) = \frac{S_{I_{\mathrm{amp}}}(\omega)}{|s_I(\omega)|^2}. \tag{95}$$

A key figure of merit for a TES bolometer is the noise-equivalent power, which is the square root of the power spectral density of the power-referred noise,

$$NEP(\omega) = \sqrt{S_P(\omega)}. \tag{96}$$

The total noise of the TES, $S_P(\omega)$, is the sum of (90) , (92), (93), and (95).

The most important figure of merit for a TES calorimeter is the energy resolution. From Chapt. 1, the full width at half maximum (FWHM) energy resolution of a calorimeter is

$$\delta E_{\mathrm{FWHM}} = 2\sqrt{2\ln 2}\left(\int_0^\infty \frac{4}{S_{P_{\mathrm{tot}}}(f)}df\right)^{-1/2} \ , \tag{97}$$

where $f = \omega/2\pi$ and $2\sqrt{2\ln 2} \approx 2.355$. This equation assumes Gaussian noise sources. If there are nonlinear elements, such as nonlinear TES resistance or thermal conductance, the noise is non-Gaussian. Then (97)

and the energy resolution calculations that follow are not rigorously applicable. These equations are a good first approximation, but a more detailed nonlinear analysis is needed. From (86) and (87), $S_{P_{\text{tot}}}(f)$ in (97) is

$$
\begin{aligned}
S_{P_{\text{tot}}}(f) =&S_{P_{\text{TFN}}} + S_{V_{\text{TES}}}I_0^2 \frac{1}{\mathscr{L}_I^2}\left(1 + (2\pi f)^2\tau^2\right) + \\
&S_{V_{\text{L}}}I_0^2 \frac{(\mathscr{L}_I - 1)^2}{\mathscr{L}_I^2}\left(1 + (2\pi f)^2\tau_I^2\right) + \frac{S_{I_{\text{amp}}}(\omega)}{|s_I(\omega)|^2} \, ,
\end{aligned}
\tag{98}
$$

which includes the Johnson noise voltage of the TES $S_{V_{\text{TES}}} = 4k_{\text{B}}T_0R_0\xi(I)$, the Johnson noise voltage of the load resistor $S_{V_{\text{L}}} = 4k_{\text{B}}T_LR_L$, the thermal fluctuation noise $S_{P_{\text{TFN}}} = 4k_{\text{B}}T_0^2 G \times F(T_0, T_{\text{bath}})$, and current fluctuations in the amplifier $S_{I_{\text{amp}}}$ (the SQUID noise).

The full form of (98) must be used for the general case including amplifier noise, but in the important limit that the amplifier noise $S_{I_{\text{amp}}}$ is negligible, (97) and (98) integrate to the simple form:

$$
\begin{aligned}
\delta E_{\text{FWHM}} = 2&\sqrt{2\ln 2}\times \\
&\sqrt{\frac{\tau}{\mathscr{L}_I^2}\sqrt{(\mathscr{L}_I^2 S_{P_{\text{TFN}}} + I_0^2 S_{V_{\text{TES}}} + (\mathscr{L}_I - 1)^2 I_0^2 S_{V_{\text{L}}})(I_0^2 S_{V_{\text{TES}}} + I_0^2 S_{V_{\text{L}}})}} \, .
\end{aligned}
\tag{99}
$$

In the limit of strong electrothermal feedback ($\mathscr{L}_I \gg 1$) and zero load resistance R_L, equation (99) simplifies to:

$$
\delta E_{\text{FWHM}} = 2\sqrt{2\ln 2}\sqrt{\frac{\tau I_0}{\mathscr{L}_I}\sqrt{(S_{P_{\text{TFN}}})(S_{V_{\text{TES}}})}} \, ,
\tag{100}
$$

and

$$
\delta E_{\text{FWHM}} = 2\sqrt{2\ln 2}\sqrt{\frac{4k_{\text{B}}T_0^2 C}{\alpha_I}\sqrt{\frac{n\xi(I_0)F(T_0, T_{\text{bath}})}{1 - (T_{\text{bath}}/T_0)^n}}} \, ,
\tag{101}
$$

where we have used equation (5) for the power flowing from the TES to the heat bath and $\mathscr{L}_I \equiv P_0\alpha_I/GT_0$. In the linear approximation, $\xi(I_0) = 1$. In the quadratic approximation, $\xi(I_0) = 1 + 2\beta_I$.

This equation is consistent with the expression in the literature [13]

$$
\delta E_{\text{FWHM}} = 2\sqrt{2\ln 2}\sqrt{4k_{\text{B}}T_0^2\frac{C}{\alpha_I}\sqrt{n/2}} \, ,
\tag{102}
$$

for $F(T_0, T_{\text{bath}}) = 1/2$, $T_{\text{bath}} \ll T_0$, and $\xi(I) = 1$.

2.7 Excess noise

TES calorimeters and bolometers have achieved excellent noise performance. TES x-ray calorimeters have been demonstrated with energy resolution of δE= 2.38 $\pm$ 0.11 eV FWHM at 5.9 keV, which at the time of this writing is the highest $E/\delta E$ achieved by any nondispersive (or energy-dispersive) photon detector. However, the performance of TES detectors still has not achieved the limits predicted by present theory. In addition to effects due to large pulses (see Sect. 2.8), a key limitation on the noise performance of TES detectors is due to unexplained noise sources in excess of those calculated in Sect. 2.6. In this section, we describe these noise sources, including both a qualitative description of the different types of excess noise observed experimentally and their scaling with different device parameters, and a review of the status of theoretical explanations for these noise sources. A successful theoretical explanation of the noise will guide the design of TES detectors to achieve their full potential.

Many noise sources can degrade the noise performance of the TES due to imperfect experimental conditions. These include RF pickup, stray photon shot noise, microphonics in the leads, noise in the amplifier chain, contact resistance fluctuations, Johnson noise on the leads, fluctuations in the temperature bath, etc. In this section we ignore these noise sources and consider excess noise sources in the TES itself. The excess noise in the TES falls into four general categories according to its dependence on the thermal circuit model

of the detector, its frequency dependence, and its temporal structure. In some cases, the different types of excess noise are related.

The first type of excess noise is dependent on the thermal circuit model of the detector. This noise source has been well explained in terms of internal thermal fluctuations between distributed heat capacities inside the TES. It is referred to as internal thermal fluctuation noise (ITFN). It is often worse for high resistance TES detectors, which have low internal Wiedemann–Franz thermal conductance. The second type of excess noise has the same frequency dependence as Johnson noise voltage in the sensor, and tends to be worse for a lower resistance TES. We refer to this noise as "excess electrical noise." The third type of noise is excess low-frequency noise in the TES, sometimes with $1/f$ dependence, but often with a different exponent. Excess "low frequency" noise is often correlated with strong excess electrical noise. Finally, in some cases switching, or telegraph, noise is observed in the temporal response of a TES. Telegraph noise is also often correlated with excess electrical noise.

ITFN occurs when the simple lumped-element model used in previous sections is not sufficient [62, 63, 53]. Additional internal variables can lead to non-Markovian noise with non-white random forces. A realistic TES consists of distributed heat capacities connected by internal thermal impedances. In Sect. 2.6, we showed that thermal fluctuations were associated with the thermal conductance connecting a TES to the heat bath. Internal thermal fluctuations are similarly associated with internal thermal impedances. As in Sect. 2.6, an impedance matrix can be derived for a more complex thermal circuit model and used to compute excess noise due to ITFN. For a TES with high resistance, it may be necessary to use a more complex thermal circuit model for the TES itself, consisting of distributed heat capacities each interconnected by a Wiedemann–Franz thermal conductance. A higher normal resistance can lead to higher ITFN excess noise.

For a low-resistance TES x-ray calorimeter with an attached absorber, a sufficient thermal circuit model often consists of an absorber heat capacity C_{abs} connected through an internal thermal conductance G_{int} (such as a bismuth film or an epoxy joint) to the TES heat capacity C. The TES is then connected through a thermal conductance G to a heat bath at temperature T. The two coupled differential equations of the previous section can then be extended to three (see, for example, [53]), and solved in the matrix formalism for the full noise. The constraint that ITFN must not significantly degrade the energy resolution places further constraints on the internal thermal conductance and the heat capacity of the absorber.

Aside from ITFN, excess electrical noise with the same frequency dependence as Johnson noise has been observed by multiple research groups using many different TES geometries and materials [6, 7, 64, 25, 65, 66, 67, 68] (see Fig. 5). There is as yet no universally accepted theoretical explanation of this noise, although steps have been made to explain it using fluctuations in magnetic domains or phase-slip lines [64, 25, 65], fluctuations in the superconducting order parameter [69, 70], and fluctuations in normal and superconducting regions leading to complex percolation current paths ([71]).

Excess electrical noise exists in TES detectors where ITFN, which is well understood, does not contribute. This excess noise seems to be larger for lower detector normal resistance, and larger when biased lower in the transition. The boundary conditions of the TES influence the excess electrical noise. If a normal-metal superconductor bilayer (3.1.2) is used as the TES , and the T_{c} is higher at the edges of the film than in the bulk, the excess electrical noise is often extremely high. This situation can be avoided by the fabrication of normal-metal banks on the boundaries parallel to the direction of current flow [72, 73] by the use of elemental superconductors, or by fabricating bilayers with the superconducting layer slightly narrower than the normal layer. It can be reduced much further by the use of normal-metal bars, or "weak links," in the TES perpendicular to the direction of current flow. The use of perpendicular normal-metal bars to reduce excess noise is the subject of a patent [65], and numerous later publications [74, 66, 67, 68]. Excess electrical noise is also a strong function of the applied magnetic field [25, 68].

The most systematic study to date of the effect of magnetic field and TES geometry on excess electrical noise is that of Ullom *et al.* [68], in which a strong correlation was found between the logarithmic sensitivity α of the TES and the excess noise. In this work, TES devices with many different geometries were tested (Fig. 6). In all cases, the materials were the same (Mo/Cu bilayers with Cu normal-metal features), the detector normal resistance was approximately the same, the bias point in the transition was held fixed, and in all cases normal-metal banks were used on the boundaries parallel to the direction of current flow. The excess noise is found to be a strong function of both magnetic field and geometry. Furthermore, the logarithmic sensitivity α of the device was also a function of magnetic field and geometry. A strong correlation between α and excess noise is observed as the geometry is varied (Fig 7). A very similar correlation is also
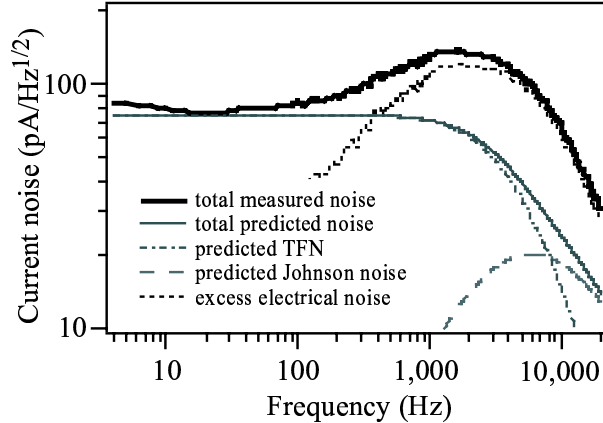
Figure 5: Measured current noise in a Mo/Cu TES x-ray calorimeter at $R_0 = 0.6\ R_N$ and zero magnetic field. Predicted noise contributions and the difference between data and theory are shown. This difference is the excess electrical noise. [68]

observed in the case of magnetic field variation. This correlation, however, has been investigated for one only materials system, and for approximately fixed detector size, normal resistance, bias resistance, and thermal conductance. Nevertheless, any quantitative theory put forward to explain the excess electrical noise in TES detectors must be consistent with the strong observed correlations between α and excess electrical noise.

Excess low-frequency noise is also sometimes observed in the TES. This excess low-frequency noise is problematic especially for bolometric applications, where $1/f$ knees as low as 0.01 Hz are sometimes desired. Qualitatively, the excess low-frequency noise seems to be correlated with especially high values of the excess electrical noise discussed above. When excess electrical noise is low, the TES $1/f$ knee appears to be lower than 0.1 Hz. The fundamental sorce of the $1/f$ noise is not known.

Finally, telegraph noise is sometimes seen in the temporal response of the TES. The telegraph noise tends to be associated with particularly large excess electrical noise. It general occurs at specific current and field bias points, and is suppressed by external magnetic fields [25] and normal-metal banks on the boundaries parallel to current flow. Suggested explanations for the telegraph noise include phase-slip line nucleation and denucleation [25, 65] and more general rearrangements of superconducting and normal-metal domains [71]. It is also observed that when the bias of the TES crosses one of the telegraph-noise regions, there is a step in the differential resistance of the TES, providing support for the interpretation of phase-slip line nucleation and denucleation or more general rearrangement of magnetic domains.

Before considering explanations for the excess electrical noise based on the details of superconductivity, it should be remembered that the small-signal TES thermodynamic noise theory put forward in previous sections is not rigorous, because TES devices are operated out of equilibrium and in the presence of nonlinear effects. Some of the "excess noise" may be due to nonlinearity or nonequilibrium effects, rather than the details of superconductivity. The NLEA in (71) suggests that some "excess" noise is due to nonzero β_I. The experimentally observed correlation between excess noise and α_I may be at least partially explained by excess noise arising from nonzero β_I, accompanied by correlations between β_I and α_I. More work needs to be done in determining correlations between nonlinear and non-equilibrium effects and observed excess noise. Furthermore, there is a need for a full theoretical analysis of the nonlinear, nonequilibrium thermodynamic system. However, while it is likely that nonlinear or nonequilibrium noise theory will provide an explanation for some of the excess noise, it is not likely that it will explain all excess noise, as the exceptionally large excess noise observed in some cases seems to be correlated with the details of superconductivity.

A number of possible mechanisms have been suggested for the excess electrical noise. The physics of the superconducting transition has already been described in Sect. 2.1. All of the mechanisms that have been proposed to explain the excess noise are related to these physical processes, so the mechanisms can be surveyed briefly here. These include either path instabilities or number fluctuations in normal channels or phase-slip lines [25, 65, 40, 75, 76], fluctuations in the superconducting order parameter [69, 70], and
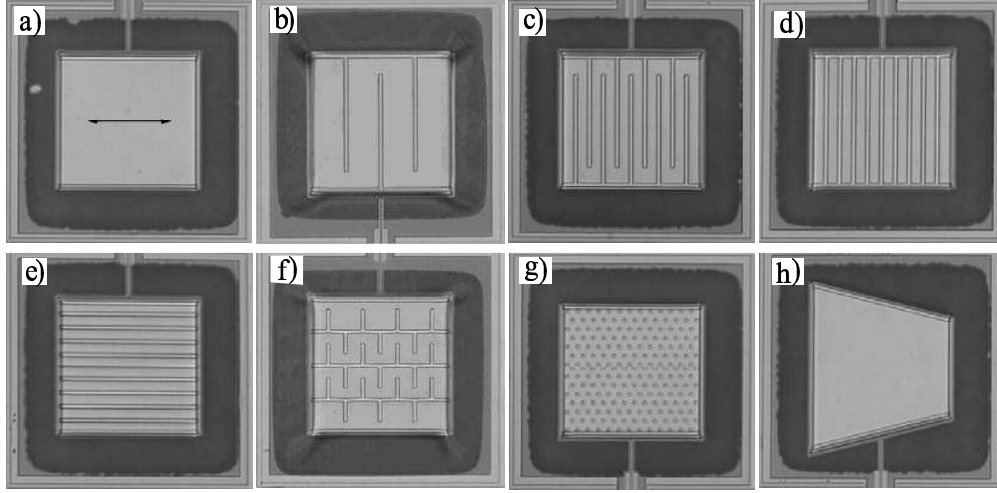
Figure 6: Micrographs of TES sensors on Si_3N_4 membranes. The arrow in (a) indicates the direction of bias current in all devices. Cu edge passivation is present on TES edges parallel to the bias current. Square sensors are 400 μm on a side. (a) standard pixel with $R_N = 14$ mΩ (b) sparse normal bars partially span the device perpendicular to the bias current (c) dense partial perpendicular bars (d) dense full perpendicular bars (e) dense parallel bars (f) parallel and perpendicular bars (g) islands (h) wedge. Normal Cu bars are 10 μm wide and 500 nm thick. Normal Cu islands are 5 μm in diameter and 500 nm thick. [68]
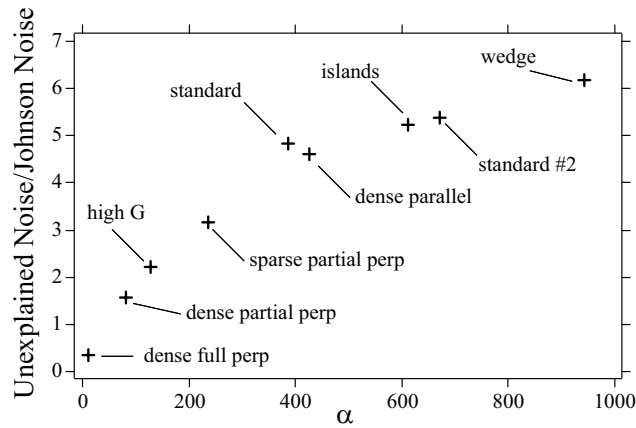
Figure 7: Ratio of excess unexplained noise to Johnson noise versus α for the TES geometries in Fig. 6. The geometries are measured with the same magnetic field and with resistance at the same fraction of the normal resistance ("perp"= perpendicular) .[68]

fluctuations in vortex pairs in the Kosterlitz-Thouless transition [77, 36, 64]. To date, only one theory has provided quantitative predictions of noise that match experiment [70], but only in one specific and very noisy geometry. This work involved TES devices fabricated in an annular, or "Corbino" geometry, in which the radial dependence of the current density creates a clear superconducting-normal phase boundary. The Corbino geometry also radially constrains the current distribution, which makes it possible to find simple analytical solutions for the order parameter. In this work, thermodynamic fluctuations in the superconducting order parameter at the superconducting-normal phase interface provides an explanation for the observed noise.

Some sources of excess noise, including ITFN, can be eliminated by careful detector design. Other sources, such as excess electrical noise, can be characterized as an experimentally determined function of other detector parameters such as α_I or β_I, allowing a computation of their effect on detector performance. If the measured excess electrical noise is written as a voltage-noise power spectral density S_{V_X}, the total voltage noise in the TES is $S_{V_{\text{tot}}} = S_{V_{\text{TES}}} + S_{V_X} = (1 + \Gamma^2)S_{V_{\text{TES}}}$. The ratio of excess noise to Johnson noise $\Gamma(\alpha_I)$ is characterized in Fig. 7 for one material system, detector size, normal resistance, bias resistance, and thermal conductanc. Here $S_{V_{\text{TES}}} = 4k_BT_0R_0$ is the value from the LEA (Sect. 2.6), with $\xi(I) = 1$, and any noise from nonlinear resistance is considered part of the excess noise term S_{V_X}.

$S_{V_{\text{tot}}}$ can then be used to determine the energy resolution. In the common limit of negligible amplifier noise, the energy resolution including excess noise contributions can be written as (99):

$$\delta E_{\text{FWHM}} = 2\sqrt{2\ln 2} \ \times$$
$$\left\{ \frac{\tau}{\mathscr{L}_I^2}\left(\left(\mathscr{L}_I^2 S_{P_{\text{TFN}}} + I_0^2 S_{V_{\text{TES}}}(1 + \Gamma^2) + (\mathscr{L}_I - 1)^2 I_0^2 S_{V_L} \right) \ \times \right.\right.$$
$$\left.\left. \left(I_0^2 S_{V_{\text{TES}}}(1 + \Gamma^2) + I_0^2 S_{V_L} \right) \right)^{1/2} \right\}^{1/2} \ . \tag{103}$$

Using (100), in the limit of strong electrothermal feedback ($\mathscr{L}_I \gg 1$), and $R_L = 0$, (103) reduces to:

$$\delta E_{\text{FWHM}} = 2\sqrt{2\ln 2}\sqrt{\frac{\tau I_0}{\mathscr{L}_I}\sqrt{(S_{P_{\text{TFN}}})(S_{V_{\text{TES}}})(1 + \Gamma^2)}} \ , \tag{104}$$

and, using (101),

$$\delta E_{\text{FWHM}} = 2\sqrt{2\ln 2}\sqrt{\frac{4k_BT_0^2C}{\alpha_I}\sqrt{\frac{nF(T_0, T_{\text{bath}})(1 + \Gamma^2)}{1 - (T_{\text{bath}}/T_0)^n}}} \ , \tag{105}$$

which is consistent with the result in [68].

Significant progress is presently occurring in understanding and mitigating excess noise in TES devices. The use of weak-link noise-mitigation features has recently improved the energy resolution of x-ray calorimeters at 5.9 keV from ≈ 4.0 eV FWHM to 2.38 ± 0.11 eV FWHM (Fig. 14). It is likely that over the next several years both the theoretical explanations and realized performance of TES devices will improve further.

2.8 Large Signals

In the development of the TES theory of Sects. 2.3-2.6, it is explicitly assumed that incident signals are small (e.g., a low-energy photon absorption in a calorimeter or a small power load in a bolometer). At many points in the derivations, parameters such as the TES resistance and Joule power dissipation are expanded in a Taylor series and the higher-order terms are dropped, leading to expressions depending only on first-order parameters such as α_I, β_I, C, and G. In many important applications, however, the small-signal approximation is insufficient. Large energy photons and power loads can "saturate" the TES by driving it outside of its narrow transition region.

A full analysis of the performance of a TES in response to a large signal requires a numerical model with parameters determined by a detailed characterization of the resistance, heat capacity, thermal conductance, and noise as a function of the full range of temperature and electrical current. However, the small-signal theory can prove surprisingly accurate even in the presence of signals that nearly saturate the device. For instance, when equations (103) or (104) are used to compute the energy resolution of the calorimeter, the

results can be within about 20 % of experimentally determined values even for energies close to the saturation energy.

The saturation power of a TES bolometer can be written as

$$P_{\text{sat}} = P_{\text{bath}}(T) - \left(\frac{V}{R_L + R_N}\right)^2 R_N \ , \tag{106}$$

where $P_{\text{bath}}(T) = K(T^n - T_{\text{bath}}^n)$ is the power flowing to the heat bath at temperature T, and R_N is the normal resistance. In the limit of a voltage bias ($R_L = 0$), and a narrow transition, so that P_{bath} is approximately constant, (106) reduces to

$$P_{\text{sat}} = \left(1 - \frac{R_0}{R_N}\right) P_{\text{bath}} \ . \tag{107}$$

A TES bolometer loses all sensitivity when the signal power exceeds P_{sat}. The thermal conductance must be chosen to be large enough that any important signal does not saturate the bolometer. Increasing the thermal conductance so that the highest signal power does not saturate, however, degrades the *NEP* for even the lowest measured signal power. To alleviate this limitation, designs have been proposed that use two TES thermometers with different T_c connected in series [78]. If the saturation power of the lower T_c TES is exceeded, the TES automatically biases on the higher T_c, and the bolometer still has some (degraded) sensitivity. When the signal power allows operation on the lower T_c branch, lower *NEP* is achieved. A second scheme to improve this limitation is to use a variable thermal conductance [79], with a value changed by an applied magnetic field. When a lower signal power is being measured, the thermal conductance is set low, and lower NEP is achieved. At higher signal power, the thermal conductance is increased.

The "soft" saturation energy E_{sat} of a TES calorimeter is the pulse energy that drives the TES completely normal. When the soft saturation energy is exceeded, the top of the pulse becomes flat. The energy resolution is degraded when the pulse energy exceeds E_{sat}, but the energy of the pulse can still be estimated, as higher-energy photons lead to pulses that are saturated for longer periods of time. As long as the pulse recovery time is much smaller than τ, the energy is still approximately equal to the energy removed by ETF (58). For even higher photon energies, the pulse recovery time becomes comparable to τ, and the reponse becomes relatively insensitive to the pulse energy.

It can be shown that, in principle, the energy resolution of a TES calorimeter operated with strong negative feedback into saturation degrades approximately as $\sqrt{E/E_{\text{sat}}}$ as long as the pulse recovery time is still much smaller than τ. In the small-signal limit, the optimal analysis of the pulse energy uses the same filter function for each pulse. Optimal analysis for large pulses is more complicated, and different filter functions must be used for different energies due to pulse nonlinearity [80, 81]. The derivation of these filter function templates can be a laborious process.

In large pulses, the noise is, in general, non-stationary. At the top of the pulse, the TES has a higher resistance, and less noise than at the steady-state resistance value. Optimal analysis in the presence of non-stationary noise also leads to the use of different filter functions for different energies. The optimal analysis of data from a calorimeter with large pulses is derived by Fixsen *et al.* [80, 81]. As long as the pulses are smaller than E_{sat}, analysis is often done with small-signal theory, with a constant filter function, with only small degradation in energy resolution. Above E_{sat}, the use of varying filter functions is necessary to prevent much larger degradation in energy resolution.

3 Single-pixel implementation

TES-based calorimeters and bolometers consist of structures that perform three key functions: thermalization of the input energy, measurement of the temperature change due to the input energy, and thermal isolation and mechanical support of the measurement structures. For the majority of detectors discussed here, an absorber thermalizes incident photon energy and delivers it to the TES to be measured. The energy raises the temperature of the electrons in the TES, causing an increase in the resistance. The TES and absorber must be sufficiently thermally isolated from the apparatus thermal ground, and the TES must be connected to the external readout circuit. In this section we will review the materials and geometries that have been used to implement single-pixel TES detectors and discuss the results obtained.

3.1 TES Thermometers

The key difference between TES detectors and other thermal detectors is the superconducting thermometer. The choice of the superconducting material used for this thermometer plays an important role in determining the detector characteristics. Of the superconductor properties, the superconducting transition temperature, T_c, of the the thermometer has the largest effect on device performance. Because of the strong temperature dependence of physical parameters such as thermal conductance G, heat capacity C, and thermal noise, the choice of T_c has important implications in device design. Furthermore, considerations such as refrigeration often play an important role in constraining device design. As a result, most TESs have transition temperatures near either 400 mK (^{3}He cryostat operation), or 100 mK (operation with adiabatic-demagnetization and dilution refrigerators). Three methods are routinely employed to achieve transition temperatures in these ranges: the use of elemental superconindexductors, proximity multilayers, and magnetically doped superconductors. Proximity multilayers are the most commonly used of the three.

Both proximity multilayers and magnetically doped superconductors are attractive for use in TES detectors because of the tunability of the transition temperature in these systems. It is also possible in these systems to tune other materials properties such as the electrical resistivity ρ_{el}. In proximity multilayers, a composite superconductor is constructed by depositing one or more layers of both a superconductor and a normal metal. When the layers are thinner than the superconducting coherence length and the interface between the layers is sufficiently clean, the composite film exhibits a reduced T_c compared with the superconducting film. This effect, know as the proximity effect, has been widely studied, but was first applied as a technique to engineer a desired transition temperature in a TES by Nagel [82]. Nagel used Ir/Au bilayers to fabricate a TES with a transition temperature near 30 mK. Many additional proximity-effect bilayer and multilayer systems have been developed and will be described in more detail below. Another technique for modifying T_c is magnetic doping of superconductors. This effect has also been widely studied over the last four decades, but was first applied to a TES by Young [83, 84], who demonstrated the suppression of T_c in W by implanted Fe ions.

The ability to controllably suppress T_c using the proximity effect or doping permits a much wider range of materials to be used in the fabrication of TES detectors. For example, there are 18 elements with bulk transition temperature less than 2 K. While many of these material have undesirable properties, five superconducting elements (Al, Ti, Mo, W, and Ir) have been widely reported in low-temperature TES detectors. Of these, all of the materials except Ir have frequent application in other areas of microelectronics. In addition to the elements listed, there are a wide variety of alloy and compound superconductors with transition temperatures in the range of interest. While these material may also have attractive properties for fabrication of TES detectors, they have not been widely used.

3.1.1 Elemental superconductors

Elemental superconductors were among the first materials used in TES detectors. Early work on dark-matter detectors utilized both Ti and W thin films [9, 85, 86]. These researchers found that sputtered thin films of W can have T_c much higher than the bulk temperature of 15 mK by variation of the deposition conditions [85, 87, 88]. This type of behavior has been widely reported. In many cases, thin films do not have the same T_c as the bulk material, and the thin film T_c can be very sensitive to a variety of deposition and processing parameters.

Recent work [89] may shed light on the reasons for this difficulty controlling T_c in W. It has long been known that sputtered films of W can exist in two phases: α, with a T_c near 15 mK. and β, with a T_c in the range of 1 - 4 K, and that a mixed phase is required to obtain transition temperatures in the desired range. Lita and coworkers [89] have used x-ray diffraction and resistivity measurements to show that mixed-phase samples can convert to α phase at room temperature within a few hours of deposition. They have also shown that a thin underlayer of amorphous Si can prevent this change, allowing stable and reproducible fabrication of W films with transition temperatures that can be tuned through deposition conditions in the desired range, in their case near 100 mK.

Although W and Ti have been used in a variety of TES detectors, they have properties that limit their universal applicability. Both of these materials have fairly high electrical resistivities (and thus small Wiedemann-Franz thermal conductivities). For applications where the energy absorption is highly localized (such as a absorption of a single photon), the absorbed energy must spread throughout the entire TES in

a time much less than the thermal time constant. The high resistivity places a limit on either the detector area or speed. Furthermore, the relatively high transition temperature of Ti (400 mK) limits the ultimate noise performance of titanium-based detectors. Nevertheless, these materials have found wide application in dark-matter detectors [87], infrared and submillimeter bolometers [14, 90], and optical photon calorimeters [27].

3.1.2 Bilayers and Multilayers

The majority of low-temperature TES detectors have been constructed using proximity-coupled TES thermometers utilizing a superconductor normal-metal bilayer. The first bilayer TESs utilized Ir/Au to obtain transition temperatures in the range of 20 - 100 mK. Although excellent detector performance has been obtained using Ir/Au [91] this system can be difficult to fabricate. High quality Ir films have been obtained by electron-beam evaporation onto high-temperature (700 C) substrates under ultra-high vacuum conditions ($< 1 \times 10^{-10}$ Torr). Later, suppression of T_c by over an order of magnitude by use of an Al normal-metal bilayer was demonstrated [92]. It was shown that very narrow superconducting transitions could be obtained even when the original starting material has an order of magnitude higher transition temperature than the desired T_c. Furthermore, very high performance x-ray calorimeters [93] were fabricated by a very simple method. Here the detectors were fabricated by simple electron-beam evaporation of Al and Ag through shadow-masks onto room-temperature substrates under high-vacuum conditions.

Although Al bilayers have been used to make sensitive TES detectors, there are several problems with this material. The combination of Al and any noble metal (Cu, Ag or Au) is not chemically stable and has many intermetallic phases that are formed at elevated temperatures. Furthermore, electrochemical effects in the Al/noble metal bilayer make wet processes such as photolithography challenging. Titanium interlayers have recently been used [94] in Al/Ti/Au multilayer as a means of alleviating these difficulties.

With the demonstration of high-quality proximity bilayers using Al, a relatively high T_c superconductor, new elements (Mo,Ti) with higher T_c were quickly adopted. Molybdenum, which has a bulk T_c of 950 mK, was first used [95] in a Mo/Au bilayer system. Because the melting point of molybdenum is similar to that of Iridium, evaporated films of Mo require much the same care in deposition as Ir films. In order to obtain properties similar to the bulk, the films must be deposited onto substrates at very high temperature and under very clean vacuum. Fortunately high quality films of Mo with near-bulk properties can be obtained by magnetron sputtering, a technique that has been widely demonstrated in Mo/Cu bilayers [96] and multilayers [97]. Titanium, with a bulk T_c of 0.40 K, has also been used in Ti/Au bilayers for TES detectors [98]

There have been a variety of theoretical studies of the properties of proximity coupled bilayers. Two recent papers provide means for calculating the bilayer T_c [99, 100]. For example, in [99], the Usadel theory is used to show that the bilayer transition temperature is:

$$
\begin{aligned}
T_c &= T_{c_0} \left[\frac{d_s}{d_0} \frac{1}{1.13(1+1/\alpha)} \frac{1}{t} \right]^\alpha, \\
\frac{1}{d_0} &= \frac{\pi}{2} k_B T_{c0} \lambda_f^2 n_s, \\
\alpha &= d_n n_n / d_n n_s.
\end{aligned}
\tag{108}
$$

Here d_n and d_s are the normal and superconductor film thicknesses, n_n and n_s are the respective density of states, T_{c_0} is the superconductor transition temperature, λ_f is the Fermi wavelength in the normal metal, and t is a unitless adjustable parameter of order 1 that describes the transmission through the bilayer interface. In practice, however, it is impossible to predict the transmission factor, which is strongly process-dependent. As a result, more empirical methods are generally employed where a recipe for a particular T_c and R_n is monitored over time so that small corrections to the thicknesses can be made.

3.1.3 Magnetically doped superconductors

A fairly comprehensive study of a variety of magnetic ions and superconductors has been carried out using ion implantation [101]. Here it was found that the T_c of both W and Mo films could be highly suppressed using small concentrations ($\approx 100\,\mathrm{ppm}$) of implanted Fe. Furthermore, the suppression could be accurately

described using an Abrikosov-Gor'kov pair breaking model. In contrast it was also found that the T_c of Al and Ti films were at best weakly dependent on Fe concentration, but strongly dependent on Mn concentration. In order to suppress T_c by a factor of 5, it has been found that a concentration of roughly 200 ppm of Mn is necessary for Ti, whereas concentrations nearer to 1000 ppm of Mn are necessary for Al. Further studies made on sputtered Al films deposited from doped targets [102, 103] indicate that the suppressed T_c in Al:Mn is due not to pair breaking, but to pair scattering from resonant magnetic impurity sites. Because the physical mechanism of T_c suppression is different, there may be very different effects on device performance for the different dopant systems.

Recently [104], a TES has been demonstrated using Al:Mn films with promising results. Although the resistivity of these doped films is higher at low temperatures than undoped films, a wide range of detector resistances is still attainable. The doped films (particularly those deposited in alloy form) can be made arbitrarily thick to reduce device resistance. This is not the case for multilayers, where the thickness of the superconducting film is limited to roughly the superconducting coherence length. An important concern is that the magnetic impurities may drastically increase the heat capacity of the films. While few measurements have been made, those to date indicate only small increases in heat capacity over undoped films.

3.2 Thermal isolation

The design and fabrication of TES detectors requires a means to control the thermal conductance, G, of the TES to the thermal bath. At the low temperatures used for TESs, normal metals have a large thermal conductivity while superconductors and insulators have much lower thermal conductivity. This difference is due to the fact that in normal metals the heat is carried by the conduction electrons, while in superconductors and insulators it is carried by the phonons. By the Wiedemann–Franz law, the thermal conductivity for normal metals scales linearly with temperature, while the thermal conductivity for phonon-mediated materials scales as T^{n-1}, where n is material dependent, but usually ranges between 3 and 4. The strong temperature dependence of phonon thermal conductance is an important factor in choosing the operation temperature of a TES.

Controlling G has been accomplished in a variety of ways, depending on the application. In most cases this thermal isolation takes the form of micromachined supports to limit phonon transport between the substrate and the TES. In some cases however, the TES is placed directly on a substrate, and the phonon thermal conductance is controlled by acoustic mismatch between the film and the substrate, or by electron-phonon coupling in the TES.

3.2.1 Micromachined thermal supports

Thin membranes of Si_3N_4 and silicon-on-insulator (SOI) have been widely used as research tools in microelectronics for the last 25 years. In these techniques, a continuous film of the membrane material is made on the top surface of a Si wafer, and a small section of wafer is completely removed from the wafer back-side leaving a free standing membrane on the front surface. This type of structure has been used for such diverse applications as ultra-fine-feature electron beam lithography (backscatter from the substrate is eliminated) to radiation hardening (small device cross section), to capacitive pressure sensors. More recently, thin membranes of these and other materials are finding wide application in MEMS (microelectromechanical systems). The fabrication methods used to create MEMS are often referred to as micromachining. We will discuss bulk and surface micromachining methods for TES detectors in Sect. 4.1.

The use of thin membranes for thermal detectors was first pioneered by groups using semiconductor thermistors in IR bolometers [105, 106] and x-ray calorimeters [107]. In both cases, these groups applied a mix of micromachining and conventional microelectronic fabrication techniques to construct a hybrid electrical-thermal device. These ideas have been widely adapted for use with TES-based detectors.

In Fig. 8, we show an example of a simple micromachined thermal support, a solid insulating membrane. Here a TES calorimeter is placed in the middle of a suspended Si_3N_4 membrane. The thin insulating membrane limits the thermal conductance from the detector to the substrate. It is possible to further limit the thermal conductance by removing some fraction of the supporting membrane. Because of the high strength of Si_3N_4, it is possible to make structures with very limited support structures. A dramatic example of this is the "spider-web" geometry employed in a variety of IR bolometers [106, 108, 98]. Using
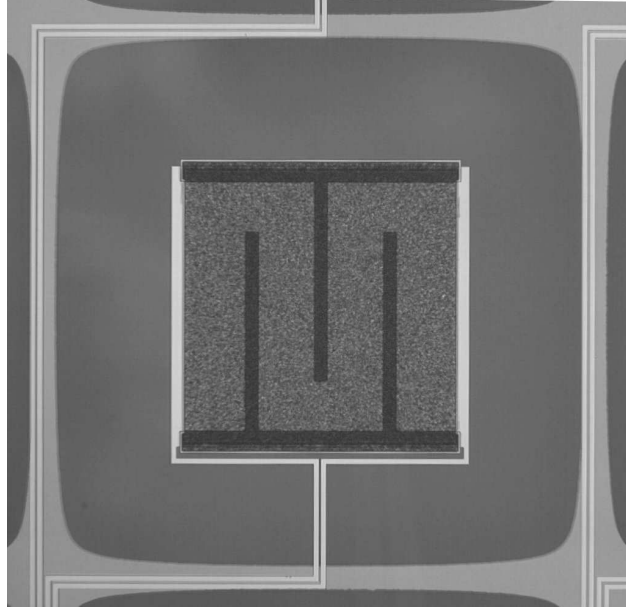
Figure 8: TES x-ray calorimeter utilizing a Si_3N_4 membrane for thermal isolation. Here the 250 μm square TES detector sits on a 450 μm membrane fabricated by deep reactive-ion etching to remove the back-side Si. The membrane thickness is 350 nm. The TES has additional normal-metal bars for noise suppression as well as a 1.5 μm thick Bi absorber. The direction of current flow is parallel to the noise-suppression bars (horizontal).

this structure (Fig. 9) it is possible to create detectors with very small thermal conductances. Silicon nitride membranes are widely used in micromachining because it has very high strength, and the film stress can be widely varied by changing the film stoichiometry.

The thermal properties of Si_3N_4 membranes have been studied experimentally [109, 110]. At the low temperatures of interest, the phonon mean free paths in Si_3N_4 become long, and G is generally limited by scattering of the phonons from the membrane surface. These studies also show that the addition of scattering centers (small Ag particles) greatly reduces the film thermal conductivity. If phonon diffusion in the nitride film were responsible for the low thermal conductivity, additional metal particles on the surface would provide a parallel heat conduction path, increasing G. It was also found that removing membrane by micromachining reduces the thermal conductance by a factor much greater than the geometric loss of conduction path. This implies that the rough micromachined surfaces are also responsible for increased phonon surface scattering.

Micromachined silicon-on-insulator (SOI) has also been employed as a means to fabricate low-G structures. Silicon-on-insulator wafers consist of two single-crystal regions of Si separated by an amorphous SiO_2 insulating region. SOI wafers are typically fabricated using either wafer bonding and grinding techniques or ion-implantation. The group at NASA Goddard has employed SOI for TES detectors in their "pop-up" style infrared bolometers [111, 112]. An example of this detector type is shown in Fig. 10.

3.2.2 Phonon Decoupling

Some researchers have employed phonon scattering from interfaces as a means to achieve thermal isolation. Like the electron-phonon decoupling discussed below, this technique is particularly effective at very low temperatures due to the strong temperature dependence of the conduction. It is possible to theoretically estimate the thermal conduction between dissimilar solids based solely on acoustic considerations [113].

An additional means of controlling the thermal conductance of the TES is provided by the electron-phonon coupling in the TES itself. At sufficiently low temperatures, it is possible for the electrons and the phonons in a material to be at two different temperatures – a "hot electron" effect. A widely studied example
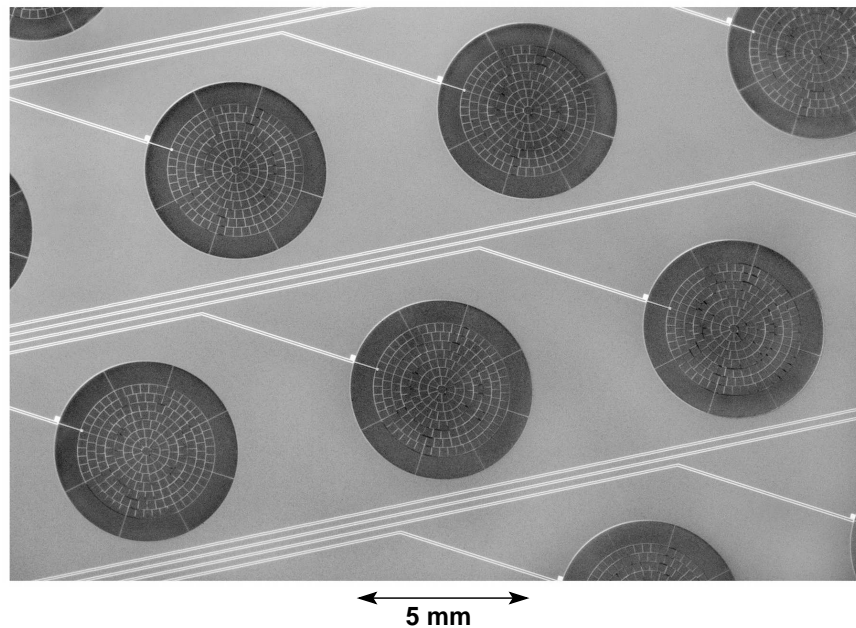
Figure 9: Spider-web-style infrared bolometers. Here a Si_3N_4 membrane is patterned into a structure resembling a spider-web. The outer legs of the web act as thermal isolation, while the inner legs are metallized to form the photon absorber. Photograph courtesy A.T. Lee, UC-Berkeley.
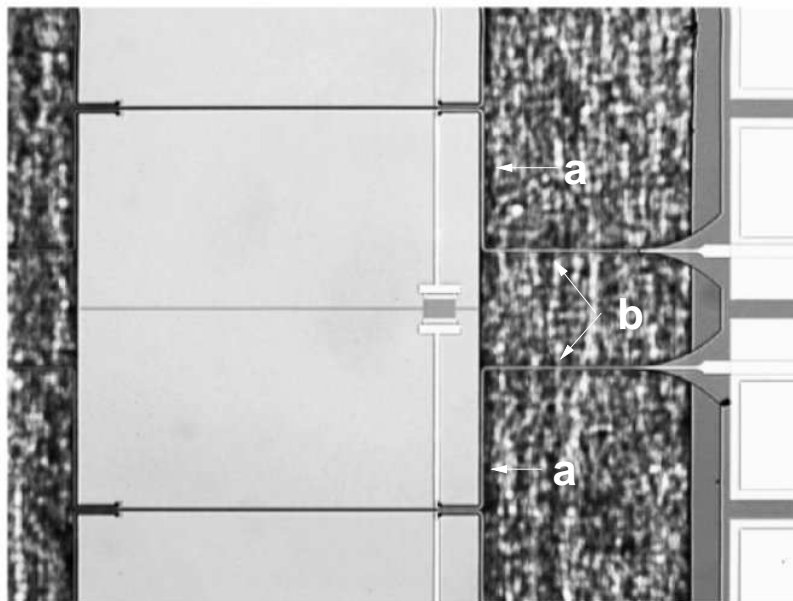

Figure 10: Silicon micromachined "pop-up" detector. The thin support legs (artificially highlighted white) consist of thin (1 - 2 μm) Si. After fabrication the legs are folded, torsionally twisting the legs in the region labeled **a**. The vertical support sections (labeled **b**) now point into the page. Similar leg structures (not highlighted) support the left side of the pixel. Photograph courtesy of S.H. Moseley, NASA GSFC

of this is the heating of the electrons in a cooled resistor [114]. This effect is greatly enhanced in certain materials, with tungsten being one of the most notable. Because of the small electron-phonon coupling in W it is possible to make TES detectors directly on a thick Si substrate, operating in a mode where the electron temperature is not in equilibrium with the phonons.

3.3 Absorbers

In order to be a useful detector, the TES must be efficiently coupled to the incoming radiation.The nature of this absorbing structure depends on the type of radiation being measured. In this section, we will briefly describe the methods employed for photons ranging from the millimeter through the gamma-ray wavelengths.

An ideal absorber should completely absorb the incoming radiation and quickly convert all of the incident energy to heat. This heat should be coupled into the TES with no additional paths for heat loss. The heat capacity of the aborber should be small compared to the TES, as extra heat capacity decreases sensitivity and increases noise.

In the far-infrared to millimeter wavelength regime, there are four principal schemes to couple the radiation to the TES: the use of absorbers with a broadband match to the impedance of free space, quarter-wave resonant cavities, feedhorns, and planar antennas. If an absorbing film is used that matches the impedance of free space ($377\,\Omega/\square$), an absorption efficiency of up to 50 % can be achieved over a wide bandwidth. A higher efficiency is possible with a narrower bandwidth using a quarter-wave resonant structure that employs a reflecting layer (backshort) and an absorbing layer separated by a spacing of $\lambda/4$. The absorbing layer must have a sheet resistance closely matched to the impedance of free space ($377\,\Omega/\square$). The absorbing layer must also be thermal contact with the TES. An example of this scheme is the FIBRE instrument [28], where an external reflector is placed behind each row of pop-up TES detectors. The detector has a $377\,\Omega/\square$ film (both Bi and PdAu alloy have been used) covering the majority of the detector surface. Heat absorbed is coupled through phonons to the small-area TES, which is in the same plane as the absorber, but which covers only a small fraction of the surface area. The detectors for SCUBA-2 [115] employ a different scheme. This absorber (a doped Si surface) and the reflector (the TES) are on opposite faces of an appropriately size silicon "brick." Heat from the absorber is coupled to the TES through the brick. Feedhorns are typically employed with the spider-web bolometers described above [98, 108]. The bolometer is placed at the outlet of the feedhorn in an integrating cavity. For maximum efficiency, the absorbing film should have a sheet resistance that matches the feedhorn output impedence. Typically, all but the outermost legs of the spider-web are coated with normal metal to make a low heat capacity absorber. Lastly, in antenna-coupled bolometers [116, 94], a superconducting planar antenna is fabricated that couples the free space radiation into a transmission line. This transmission-line is terminated with a resistor matched to the transmission-line impedence. The TES is then placed in thermal contact with the termination resistor.

Calorimeters in the near-IR, optical and UV have to-date used much simpler absorbers: they have utilized a tungsten TES itself as the absorber. Because tungsten has a sufficient absorption efficiency in these wavelengths ($\sim$ 10-20 %), detectors with good quantum efficiency have been made using only the TES as the absorber. For applications where higher quantum efficiency is required, techniques such as $\lambda/4$ cavities or anti-reflection coatings can provide a large improvement. Rosenberg [117] has demonstrated a 97 % absorption efficiency in tungsten TES using both anti-reflective coatings and a gold reflector placed underneath the TES.

Because of the extremely short wavelengths in the x-ray and gamma-ray bands, the use of the resonant structures described above is not possible. Instead, since the reflection coefficient at normal incidence is near zero at these wavelengths, it is sufficient that the absorber have high photon stopping power to achieve good quantum efficiency. The requirements of high stopping power and low heat capacity place a constraint on the choice of materials for x-ray and gamma-ray absorbers. For applications in the important soft x-ray range of a few keV, the semi-metal Bi has been used as the absorber in all high-resolution results with high quantum efficiency. The high resistivity of Bi allows the absorber to be placed directly in contact with the TES without electrically shorting it out or causing a significant shift of T_c. In these devices, both electron and phonon excitations from the absorbed photon can easily couple to the TES. Evaporated films of Bi (with thicknesses of $\sim$2-3 μm for 3 keV applications and $\sim$ 10 μm for 10 keV applications) are patterned with conventional photolithography, making process integration simple. Many groups are beginning to apply "mushroom" absorbers [118] to this problem. Here a two-level photoresist stencil is used to make an absorber

that is larger than the TES (Fig 11).

Work with low-α thermistor-based calorimeters, where heat capacity constraints rule out all absorbers except superconductors and insulators, has shown that high-purity Sn and HgTe absorbers provide good energy resolution [119, 120]. Recent work [97] on TES gamma-ray calorimeters also use glued tin absorbers.

3.4 Useful formulas

In this section we will present some simple formulas useful in designing TES detectors, as well as values of material properties (Table 2) for a variety of elements used in TES construction.

3.4.1 Electrical conductivity of normal-metal thin films

It is useful to use a simple free-electron model to express the electrical conductivity, σ (and the resistivity ρ_{el}) in terms of the electron mean free path ℓ:

$$\frac{1}{\rho_{\text{el}}} = \sigma = \frac{ne^2\ell}{mv_{\text{F}}} \ , \tag{109}$$

where n is the density of free electrons, e is the electron charge, m is the effective electron mass, and v_{F} is the Fermi velocity. In this simplified model we ignore the temperature dependence of all terms but the mean free path. It is important to note that this approximation works well for alkali and noble metals, but does gives poor results for transition metals such as molybdenum. At room temperature the mean free path is controlled by inelastic electron-phonon scattering, which is strongly temperature dependent. At sufficiently low temperature, the mean free path is controlled by impurity scattering and thus becomes temperature independent. For this reason the RRR (room-temperature resistance ratio), which is the ratio of resistivity at room temperature to the temperature independent low-temperature resistivity, is a convenient measure of sample purity. As metals are cooled from room temperature, their electrical resistance decreases due to reduced scattering. At a sufficiently low temperature, phonon scattering becomes insignificant and the electrical resistivity is dominated by impurity, isotope, or surface scattering, and the resistivity becomes independent of temperature.

For thin-film samples at low temperatures, it is important to consider the case where the mean free path exceeds the film thickness. Here we apply the Fuchs-Sondheimer model to determine the effective mean free path [121]:

$$\frac{1}{\ell(d)} = \frac{1}{\ell_0} + \frac{3(1-p)}{8d} \ , \tag{110}$$

where d is the film thickness and p is the probability of specular scattering at the surface. The probability p is often used as a fitting parameter, and can be zero for rough films. In more general theories, p is a function of the angle of incidence at the surface.

3.4.2 Heat capacity

At low temperature the heat capacity of normal metals is almost entire due to the electron heat capacity and thus is linear in temperature. A convenient form for the heat capacity is

$$C(T) = \frac{\rho}{A}\gamma VT \ , \tag{111}$$

where T is the temperature, V is the sample volume, γ is the molar specific heat, ρ is the mass density, and A is the atomic weight. The heat capacity for superconductors is more complicated because there are both phonon and electrical contributions with different temperature dependences. However, at T_{c}, BCS theory predicts that the heat capacity of a superconductor is 2.43 times the normal-metal value. Because the TES is operated within the superconducting transition, the heat capacity varies between C and 2.43 C as the resistance changes. The actual value of C within the transition can be determined from the complex impedance measurement [52] shown in Fig 4.
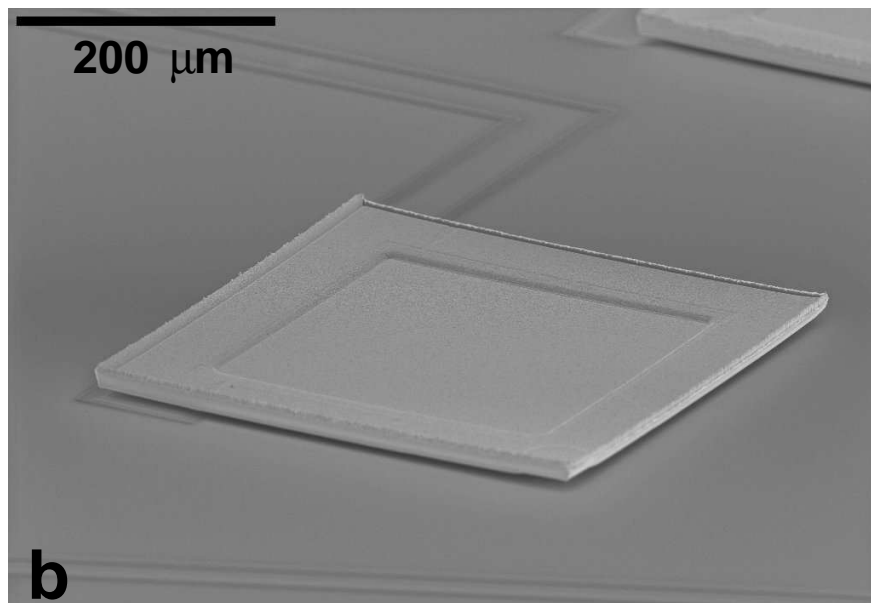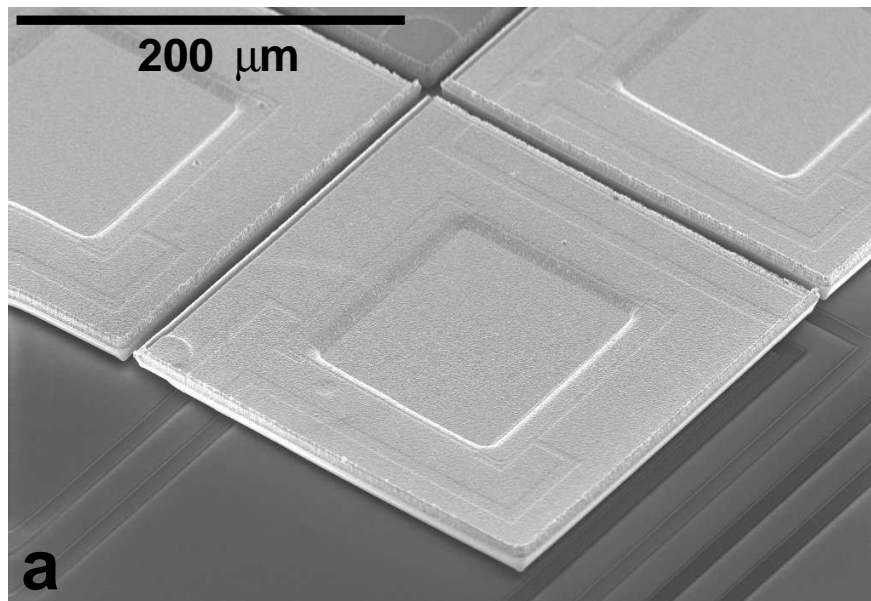
Figure 11: Electron micrographs of Bi "mushroom" absorbers. The "cap" of the mushroom is show higher than the "stem", and is standing above the surface of the substrate. Photos courtesy J. A. Chervenak, NASA GSFC, SEM images by L. Wang.

Table 2: Table of useful values for calculating TES properties presenting the room-temperature bulk electrical resistivity ρ_{el}, free-electron density n, Fermi velocity v_{F}, molar specific heat γ, ratio of density to atomic weight ρ/A, superconducting transition temperature T_c, and bulk value of zero-temperature London penetration depth $\lambda_{\mathrm{L}}(0)$. The values of n and v_{F} (see section 3.4.1) are presented for the transistion metals to allow estimation of mean-free-path from measured resistivity.

	ρ_{el}[1] ($\mu\Omega\cdot$cm)	n[2] (10^{28}/m^3)	v_{F}[2] (10^6m/s)	γ[1] (mJ/mole·K^2)	ρ/A (mole/cm^3)	T_{c}[1] (K)	$\lambda_{\mathrm{L}}(0)$ (nm)
Al	2.74	18.1	2.03	1.35	0.100	1.140	16[1]
Ti	43.1	10.5	.041 [4]	3.35	0.0944	0.39	310[4]
Mo	5.3	38.6	0.60[4]	2.0	0.107	0.92	
W	5.3	37.9	0.70[4]	1.3	0.105	0.012	82[5]
Ir	5.1	63.4	0.36[6]	3.1	0.117	0.140	29[6]
Nb	14.5	27.8	0.62[3]	7.79	0.0922	9.5	39[7], 88[8]
Cu	1.70	8.47	1.57	0.695	0.141	-	-
Ag	1.61	5.86	1.39	0.646	0.0974	-	-
Au	2.20	5.90	1.40	0.729	0.0983	-	-
Bi	116.	14.1	1.87	0.008	0.0468	-	-

Sources: [1][124], [2][125], [3][126], [4][127], [5][128], [6][129], [7]bulk value [124], [8]thin-film value [130].

3.5 Thermal conductance

The thermal conductance G of normal metals at low temperature is dominated by Wiedemann-Franz thermal conductance of the normal electrons:

$$G = L_0 T/R . \tag{112}$$

Here L_0 is the Lorenz number, T is the temperature and R is the electrical resistance. The Lorenz number can often be approximated using the value for a degenerate electron gas [122], $L_0 \approx \pi^2 k_{\mathrm{B}}^2/(3e^2)$ =24.4 nW·Ω·K^{-2}. Near T_{c}, the Lorenz number of a superconductor will be close to the normal value. However, well below T_{c}, the electron thermal conductance becomes exponentially small, as the electrons are bound in Cooper pairs that do not scatter or conduct heat. This fact is often used as a means to make electrical contacts with low thermal conductance. By choosing a superconductor with $T_{\mathrm{c}} \geq 10 T_{\mathrm{fridge}}$ the electron thermal conductance in the electrical leads can generally be assumed to be zero.

The thermal conductance G of Si$_3$N$_4$ membranes at low temperatures [109] is often dominated by surface scattering effects, and it is possible to place only an upper limit on the conductance:

$$G = 4\sigma A T^3 \xi . \tag{113}$$

Here σ has a value of 15.7 mW/cm^{2}K^4, A is the cross-sectional area perpendicular to heat flow, and ξ is a numerical factor with a value of one in the case of specular surface scattering but with a value of less than one for systems with diffuse surface scattering.

In metals with small volume and high power densities, the thermal impedance between the electron and phonon systems can be important. The electrons will heat to a temperature well above the phonon temperature in the bath. In this case, the power flow from the electrons to the phonons will be $P = \Sigma\Omega(T_{\mathrm{el}}^5 - T_{\mathrm{ph}}^5)$, where Ω is the material volume and Σ is a material-dependent constant ($\sim 10^9$ W·m^{-3}·K^{-5}). Hence, the thermal conductivity is

$$G = 5\Sigma\Omega T^4 . \tag{114}$$

It is interesting to note that for cases when G is dominated by electron-phonon conduction, since both C and G depend linearly on TES volume, the natural time constant τ is independent of TES volume. Recent results [123] indicate that for thin metal films, disorder may increase the temperature exponent of the thermal conductance from 4 to 5.
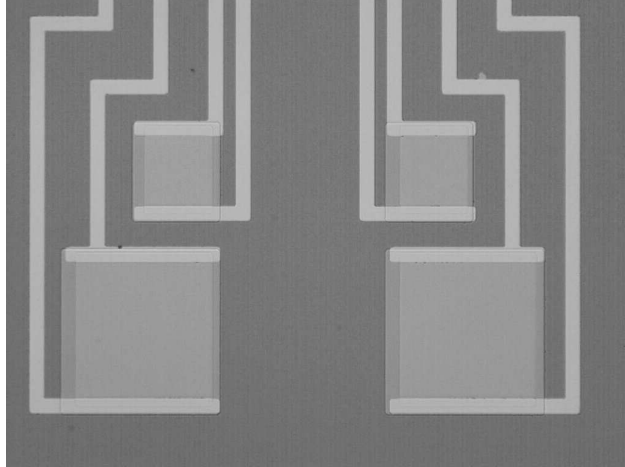
Figure 12: Optical microphotograph of W optical-photon calorimeter showing four individual detectors and Al wiring. Photograph courtesy of A. E. Lita, NIST.

3.6   Example Devices and Results

As previously stated, a large number of TES-based detectors have been developed with excellent performance for a variety of applications. In this section, we review the single-pixel performance results of two example TES calorimeters: an optical photon calorimeter and an x-ray calorimeter.

3.6.1   Optical-photon calorimeters

An interesting new application of photon detectors is quantum cryptography [26]. Secure systems require detectors with single-photon sensitivity at telecommunication wavelengths ($\sim 1.5\ \mu$m) and very low dark counts. These characteristics can both be provided by calorimeters designed to operate at visible-photon wavelengths. Furthermore, such detectors provide photon number-resolving capabilities not afforded by conventional detectors such as Si avalanche photodiodes. Tungsten TES calorimeters have been developed for quantum information applications in addition to optical astronomy [27, 26].

Using small-volume W films (25 μm $\times$ 25 μm $\times$ 35 nm) at temperatures below 100 mK, it is possible to obtain values of C and G necessary to fabricate a fast (10 - 50 μs fall-time) calorimeter with saturation energies of roughly 10 eV. Because the dominant thermal impedance is provided by electron-phonon decoupling, fabrication of such a device is simpler than for calorimeters that rely on micromachined membranes. The W film is deposited and patterned into squares by wet etching in an alkaline ferricyanide solution. An aluminum wiring layer is then added using a lift-off process. A detector completed by this process is shown in Fig. 12. One difficulty with these detectors is the relatively low absorbance of the W film in the wavelengths of interest. Recent improvements include placing a mirror and dielectric underneath the W TES to make a quarter-wave absorbing cavity [117]. The improved structures show near-unity absorption.

In Fig. 13 we show a spectrum demonstrating both the number-resolving capability and the excellent energy resolution (0.2 eV FWHM) obtained with these detectors. These detectors show great promise for applications in the fields of quantum information, where they may be used for quantum cryptography, for experimental tests of Bell's inequality, and in astronomy, where observations of pulsars require detectors with the ability to provide simultaneous measurements of photon energy and arrival time.

3.6.2   X-ray calorimeters

The need for high-resolution detectors of soft x-rays is one of the primary drivers for developing cryogenic detectors. For this reason, x-ray calorimeters have been one of the most active research areas in cryogenic detectors, with active developments in both semiconductor thermistor-based calorimeters (Chapt. 2) and TES calorimeters [96, 74, 131, 132, 133].
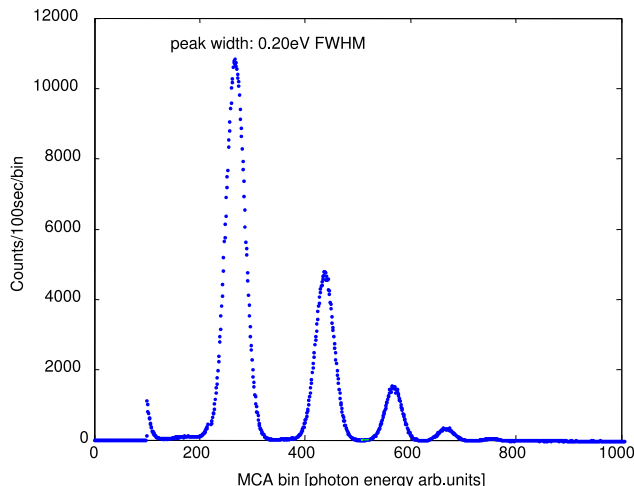
Figure 13: Pulse-height spectrum obtained for highly attenuated pulses of 1.55 μm laser photons (0.8 eV). Here, each pulse can contain 1 or more optical photons. The spectral peaks indicate differing photon numbers in each pulse. Figure courtesy of A. J. Miller, NIST.

Recent studies [65, 66, 134, 67] have demonstrated that additional normal metal structures placed within a TES can greatly reduce excess noise. Furthermore [68] a relationship between excess noise and thermometer α has been demonstrated (see Fig. 7). Using this relationship and additional normal-metal structures to fabricate devices with a pre-determined value of α_I, we have powerful tools to optimize TES energy resolution (see Sect. 2.7).

A pixel designed using this procedure is shown in Fig. 8. The additional normal-metal bars are clearly visible underneath the 1.5 μm thick Bi absorber. These detectors were fabricated using a standard TES process [73]. A Mo/Cu sputtered bilayer is fabricated on a Si_3N_4 coated substrate; the TES and Mo wiring is defined by two wet-etch steps. The normal-metal Cu boundaries and additional transverse bars are deposited by a lift-off process, as is the Bi absorber. In the final step, the Si underneath the pixel membrane is removed with a deep reactive ion-etch process.

In Fig. 14 we show the ^{55}Fe X-ray spectrum obtained by the pixel in shown Fig. 8. A fit to this spectrum of the Mn Kα lines indicates an instrument resolution of 2.38 $\pm$ 0.11 eV FWHM. This pixel has an area of 250 μm $\times$ 250 μm and a pulse fall-time of 230 μs. A larger device (400 μm $\times$ 400 μm) has an energy resolution of 2.9 $\pm$ 0.1 eV, with a fall-time of 90 μs.

4   Arrays

Many applications require large arrays of TES detectors. TES arrays are being developed for astronomical imaging (including millimeter, submillimeter, optical, and x-ray cameras). They are also being developed as a means to increase the collecting area of detectors for terrestrial x-ray spectrometry.

In recent years, significant progress has been made in fabricating TES detector arrays. Lithographic techniques have made it possible to fabricate many pixels at one time. Advances in micromachining techniques have made it possible to separately thermally isolate the pixels.

Even though the fabrication of large arrays is now possible, new readout techniques are necessary before such arrays can be practically implemented. The difficulty of separately wiring a large number of low-temperature detectors from subkelvin temperatures to room temperature precludes all but very modest detector arrays (hundreds of pixels). For larger arrays, it is necessary to use cryogenic multiplexers to reduce the wiring count. One of the most compelling reasons for the widespread interest in TES detectors is the existence of viable multiplexing schemes. Numerous SQUID-base multiplexers are being developed to extend the single-pixel SQUID readout (Fig. 2) to a multiplexed readout where multiple detectors signals are carried on a single set of signal leads.
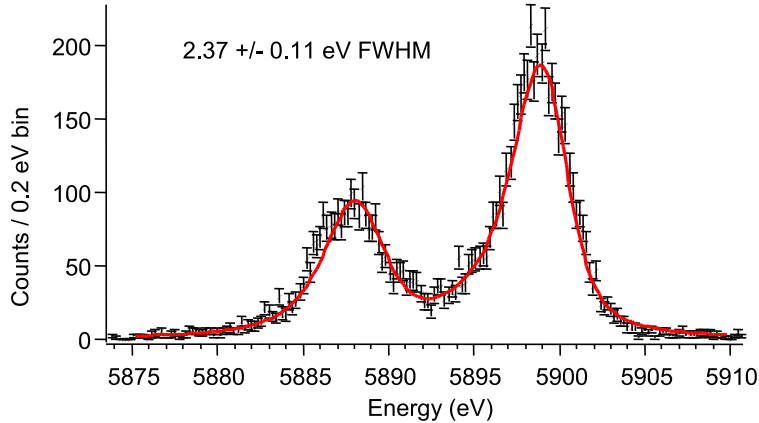
Figure 14: X-ray spectrum of an ^{55}Fe source measured with the TES calorimeter shown in Fig. 8. The data points are shown with statistical error bars, and the line is a fit to the Lorentzian natural linewidths of the Mn-Kα complex [135] convolved with a Gaussian detector response.

In this section we review recent developments in both TES detector array fabrication and cryogenic SQUID multiplexers.

4.1 Array fabrication and micromachining

Arrays of TES microcalorimeters or bolometers must include absorbers, thermometers, and thermal isolation and support structures. Many applications require close-packed arrays with large active-detector filling fractions, which severely limits the area of the array that is available for functions such as support and wiring. Because of their compatibility with standard planar microelectronic processes, it is simple to replicate a large array of TES thermometers. The challenge is the development of thermal supports, wiring, and absorbers that are compatible with arrays.

In Sect. 4.1.1, we describe the anisotropic silicon wet etches that were used in most early single-pixel TES x-ray calorimeters as well as the plasma etch techniques that are presently most often used in array fabrication. In 4.1.2 we describe the recent development of surface-micromachined TES arrays.

4.1.1 Bulk Micromachining

Most TES detectors use the widely developed Si_3N_4 membranes formed by bulk micromachining (BMM) for thermal isolation. A thin film of Si_3N_4 is deposited on the wafer front side and the substrate underneath a region of the nitride film is etched from the backside to form a free-standing membrane. Various processes are used to form deep three-dimensional structures in the substrate [136]. For most BMM TES detectors, this implies that an etch step is performed on the back-side of the wafer to form a thermally isolated membrane on the top surface. While there are many different BMM methods, we describe only two: anisotropic wet etching of Si and deep reactive ion etching of Si.

The crystalline structure of the Si substrate can be used to significant advantage in bulk micromachining. The etch rates of Si in hot alkaline solutions such as KOH or tetramethylammonium hydroxide (TMAH) varies strongly with crystal direction. The etch rate for (110) planes is roughly 600 times higher than for (111) planes. Additionally, these etches have a high selectivity against etching silicon nitride, which forms an ideal etch stop. These "crystallographic etches" can be used to form a variety of features. For instance, if a Si_3N_4-coated <100> Si wafer has a small square window opened in the Si_3N_4, a KOH etch results in an pryamidal etch pit in which each face is a (111) plane. If the window is large enough, the etch pit is a truncated pyramid with the front-surface membrane at the top, so that the Si_3N_4 membrane is smaller than the etch pit on the backside of the wafer. This is a commonly used geometry for single pixels. The size of the window required on the backside of the wafer to produce a given membrane size on the front can be easily calculated using the thickness of the wafer and the angle between the (111) planes and the substrate
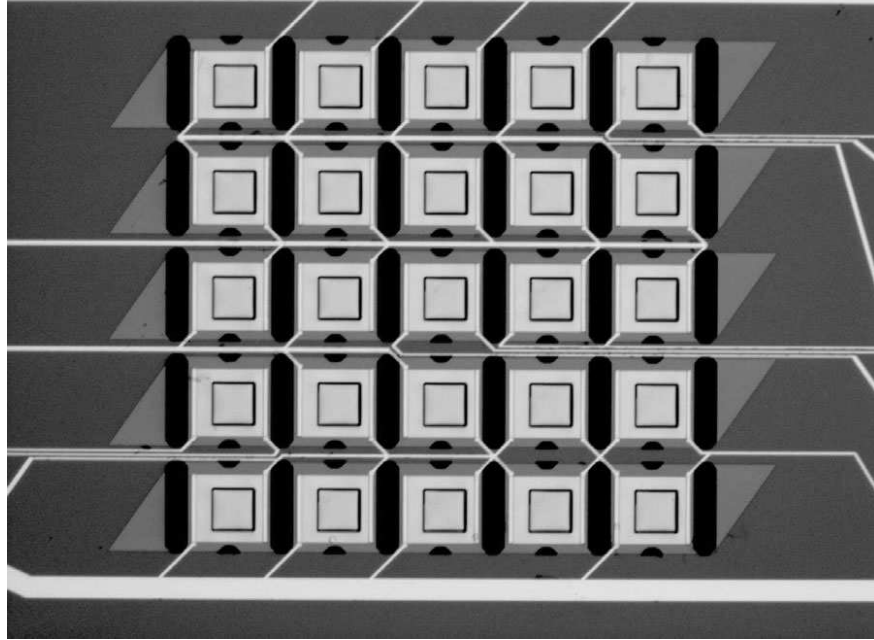
43

Figure 15: Microphotograph of a 5×5 pixel array of microcalorimeters fabricated by bulk micromaching on a Si <110> wafer. The Si bars and (111) planes run horizontally, with the trapezoidal etch terminations on the left and right side of the array. Each row of pixels is on a single membrane. Photograph courtesy of Marcel Bruijn, SRON-Sensor Research and Technology

face (54.7°). However, this angle prevents the fabrication of close-packed arrays by this process. In order to maintain support bars between pixels, there must be a space of $2\sqrt{2}$ times the substrate thickness between membranes on the top surface.

Etch faces perpendicular to the wafer face can be obtained in <110> wafers. In this geometry, it is possible to fabricate individual membranes separated by thin Si bars in one dimension, making close-packed arrays possible [137]. The crystallographic constraints, however, result in trapezoidal pits and membranes. Thus, in a close-packed square-pixel array, if adjacent pixels in a column are placed on different membranes, adjacent pixels in a row must be on the same membrane. In order to reduce thermal crosstalk between pixels within a row, normal-metal heat sinks are fabricated between pixels on the top surface of the membrane. Thermal isolation between pixels in a column is provided by the Si bars between each membrane. Such a device has been fabricated (Fig 15) and measured [138] obtaining results similar to single pixels.

Anisotropic plasma etching can also be used for bulk micromachining. Commonly referred to as deep reactive ion etching (DRIE), this techique utilizes ions directed at the wafer surface and edge passivation to etch arbitrarily shaped structures with nearly vertical sidewalls into Si. While several variations of this technique exist, the most common is the "Bosch process" [139, 140]. This process has two phases: an etching phase (using SF_6 gas to etch the Si), and a passivation phase (using C_4F_8 gas to grow protective polymer on exposed sidewalls). By rapidly switching between the etching and passivation phases it is possible to create very high aspect ratio structures with straight sidewalls. An example of structures created using this process is shown in Fig. 16. This process can also be used to fabricate membranes because of the high selectivity to SiO_2 (> 100:1) and Si_3N_4 (> 30:1). Because of the higher selectivity, silicon dioxide is generally used as the membrane etch stop. In a typical process, the membrane consists of a bilayer of SiO_2 and Si_3N_4. The thickness of the oxide is determined by the selectivity, the wafer thickness, and the etching uniformity obtained in the tool, with layer thickness of $\sim 100\,\mathrm{nm}$ being typical.

The properties of DRIE make it a nearly ideal tool for fabricating close-packed TES arrays with bulk micromachining. Because of the good selectivity of this etch to SiO_2, Si_3N_4 and photoresist, and the large attainable aspect ratios (> 30:1), close-packed arrays of thermally isolated TES detectors are now easily realized in a variety of geometries [141, 142, 143]. An example array fabricated by DRIE is shown in Fig 17.

44

Figure 16: Electron micrograph of a test strucure etched using DRIE, demonstrating the arbitrary geometries possible with this technique.

Even with DRIE, portions of the array area must be dedicated to the supporting grid and pixel wiring.

Another consideration in BMM arrays is the thermal conduction within the support structure. Ideally, the interpixel supports would be perfect thermal grounds so that each pixel sees an identical thermal environment, and there is no thermal crosstalk between pixels. Realistically, a tradeoff must be made between the thermal considerations and the desired filling fraction. The thermal conductivity of the Si beams may be strongly dependent on processing. Beams etched by crystallographic etches typically are much smoother than structures etched by DRIE, which exhibit a typical roughness of 100 nm. This roughness can substantially reduce the thermal conductance [144]. The thermal conductance can be improved by coating the micromachined walls with normal metal. For many array geometries, this coating can be accomplished by back-side evaporation at oblique angles.

In order to obtain near-unity filling fractions, additional techniques are employed. In x-ray detectors, mushroom absorbers (Sect. 3.3) can be integrated with either DRIE or <110> wet-etched arrays, resulting in very high filling fractions. The overhanging region of the mushroom can be used to cover the supporting grid and wiring.

Because Si is transparent to infrared and submillimeter wavelengths, other means can be used to obtain high-filling-fraction TES arrays for these wavelengths. One method, first developed for semiconductor thermistor bolometers [145], uses this tranparency to place the detector circuitry on the opposite side of the wafer from the incoming illumination. In this way, the electrical signals can be taken off-wafer to a separate readout circuit using wafer hybridization techniques such as indium bump-bonding.

This technique is currently being used for the TES detectors for SCUBA-2 [115]. A cross-sectional sketch of the SCUBA-2 detectors is shown in Fig. 18. DRIE is again used to create the thermal breaks between pixels and the support frame; however, here the pixels are composed of a thick region of silicon that is left behind the TES to form the quarter-wavelength absorbing cavity. The TES forms the reflector, and doped Si is used to form the absorber. Indium bump-bonding is used to attach the side of the detector wafer containing the TES to a separate readout wafer, eliminating the need for pixel wiring on the detector wafer. The readout SQUID multiplexer wafer is discussed further in Sect. 4.2.3.

4.1.2 Surface micromachining

Although bulk micromachining methods are in use, there are several drawbacks to this method, including the expense of the specialized DRIE tool and the delicate nature of the final array. Because of these drawbacks, several groups [146, 147, 148] are exploring the use of surface micromachining to fabricate arrays of TES detectors. In surface micromachining (SMM), all process steps take place on the front surface of the wafer. The thermal isolation is typically achieved by using a temporary mechanical support as a sacrificial layer that is removed near the end of the process. Because this is a planar process, which leaves the substrate
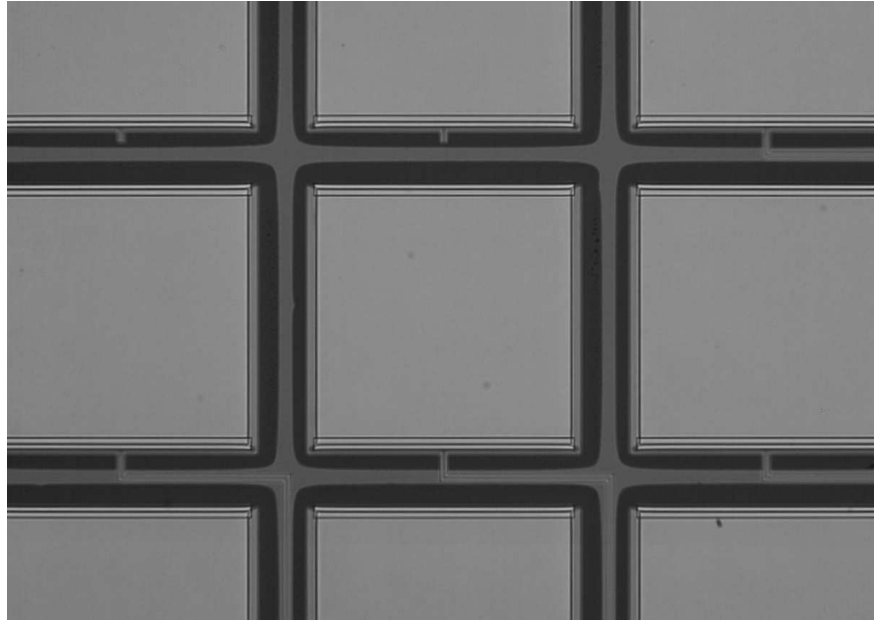
Figure 17: Optical micrograph showing a portion of a TES x-ray microcalorimeter array fabricated using DRIE. The floating squares (light gray)are TES detectors located on Si_3N_4 membranes (black), which are surrounded by the Si supporting grid (dark gray).
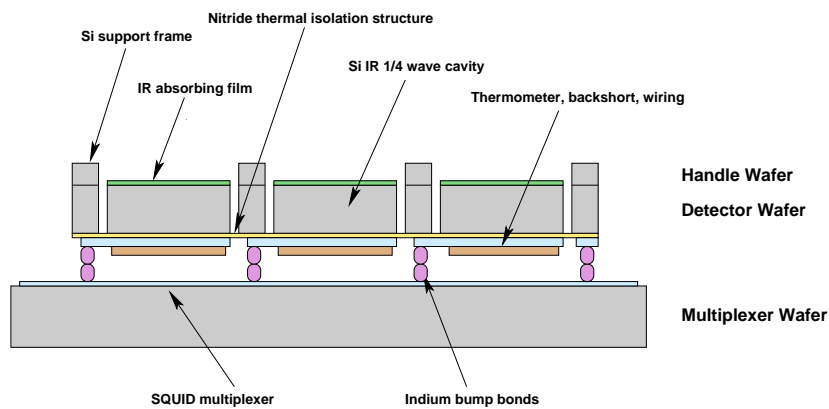

Figure 18: Sketch showing the pixel architecture used for SCUBA-2. The detector wafer is fabricated by fusion-bonding two wafers (the "handle" and "detector" wafers) with the absorber and DRIE etch masks on the internal faces. The TES detectors are deposited on the fused wafer, and the detector wafer is indium bump-bonded to a multiplexer wafer to provide electrical readout. Finally, a DRIE etch is used to etch down to the absorber and thermally isolate the pixels.
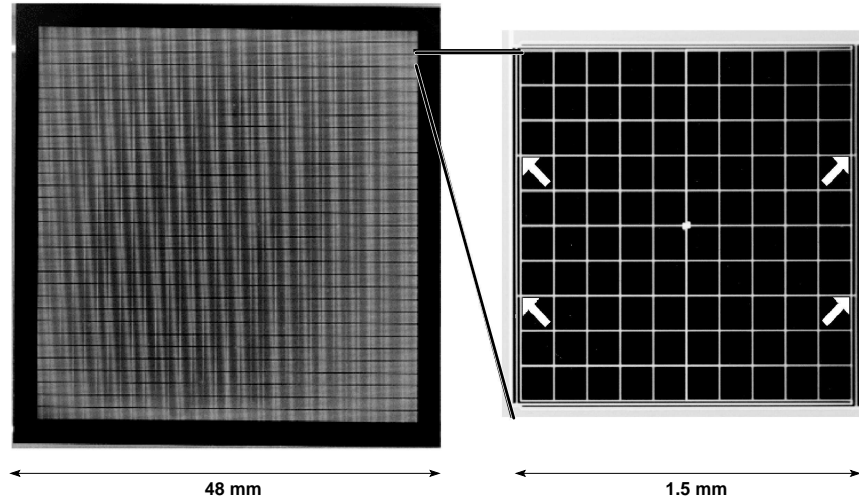
Figure 19: Photographs showing close-packed spider-web far-infrared / millimeter detectors fabricated by XeF_2 surface micromachining. On the left is an overview of the 32 × 32 array, and on the right is a magnification of the pixel. The white lines are silicon nitride beams suspended above the wafer surface. The four white arrows indicate the web attachment points. Photograph courtesy A.T. Lee, UC-Berkeley.

under the platform intact, it is possible to fabricate the detectors on top of other structures such as wiring or readout electronics. SMM arrays thus have the potential of a higher level of integration than is achievable with BMM.

The basic ideas for TES surface-micromachined detectors derives from uncooled surface-micromachined bolometers [149, 150] that have been under development for many years and form the basis of several commercially available imaging products. In uncooled SMM bolometers, a platform of PECVD Si_3N_4 is grown on a sacrificial mesa of polyimide. The silicon nitride membrane is patterned to have supporting legs that extend off the mesa, and the mesa is removed using an oxygen plasma. The resultant membrane is a three dimensional structure with a flat tabletop held above the surface of the wafer by curved supporting legs. While the specifics of this process are not applicable to TES detector arrays, many of the SMM TES approaches use similar techniques.

Because of the large thermal stresses incurred when cooling from room-temperature to the subkelvin operating temperatures, the membrane material must have very high strength. This has led researchers in SMM TES detectors to use Si_3N_4 grown at high temperature (∼800 C) by LPCVD as a membrane material. Silicon nitride membranes grown with lower temperature techniques (such as PECVD) are porous and have inferior mechanical properties. This high growth temperature has thus far limited the choice of sacrificial materials to Si. This sacrificial layer has come in the form of a plain Si wafer [146], a silicon-on-insulators wafer [151], and polysilicon [148, 147]. Recent measurements [152] indicate that polyimide may form a strong thermal isolation membrane that can be fabricated using much lower processing temperatures than LPCVD silicon nitride. This result may be very helpful in integrating under-pixel wiring or readout.

The removal of the sacrificial layer can be a difficult step. In many geometries, the lateral extent of the sacrificial layer under the membrane is much greater than the sacrificial layer thickness. This rules out the use of plasma etching, because the active plasma species experiences too many collisions and thus becomes inactive before reaching the sacrificial layer. For this reason, wet etches such as hydrazine [151] and TMAH are used [148] as is the dry plasma-less XeF_2 etch [146, 147]. The XeF_2 etch [153] is unique in that it is a gas-phase chemical etch, and thus does not apply surface tension forces to the delicate etched structures. An example of a TES array etched using XeF_2 is shown in Fig 19. Here a silicon nitride spider web is released from the substrate using the XeF_2 etch.

Surface micromachined X-ray microcalorimeters are currently under development by two groups [147, 148]. Because of the relatively small pixels required (200 μm - 500 μm), and the high fill factors desired, x-ray arrays especially benefit from the potential extra substrate area that may be available for wiring with
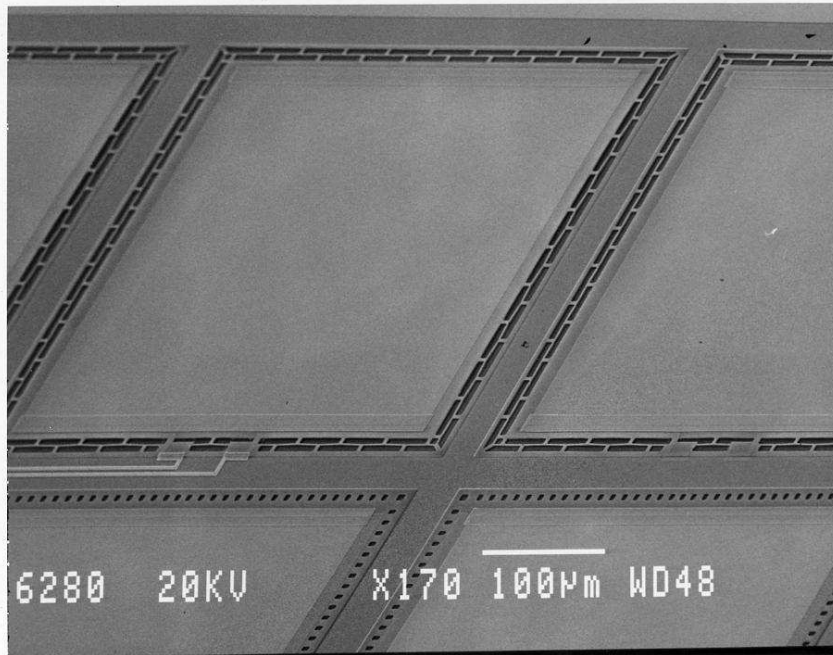
Figure 20: Electron micrograph showing a portion of a TES x-ray microcalorimeter array fabricated BY XeF_2 surface micromachining. In this image, we show pixels with two different release/support geometries. The large membrane squares are 2 μm above the wafer surface. The dark area are holes in the silicon nitride membrane. The underlying Si sacrificial layer was removed by XeF_2 etching through these holes.

this technique. A portion of a SMM x-ray microcalorimeter array is shown in Fig 20.

4.2   Multiplexed Readout

Arrays of thousands of TES detectors are now being developed. As shown in Fig. 2, SQUID circuits to instrument a single TES require multiple wires to be run from cryogenic temperatures to room temperature. These can include the detector bias, first-stage SQUID bias, first-stage SQUID feedback, series-array SQUID bias/output, and series-array SQUID flux bias. If the same "brute force" techniques are used to read out each pixel in a large array, the complexity, cost, and power load due to many thousands of leads can become unmanageable. A cryogenic SQUID multiplexer can be used to reduce the number of leads.

A number of schemes have been developed to multiplex the outputs of many TES pixels into a small number of wires. These schemes can be divided into broad categories based on the frequency range (low frequency or microwave) and the basis set used for encoding (principally boxcar functions for time division or sinewaves for frequency division).

At low frequencies, both time-division multiplexing (TDM) schemes with a SQUID switch at every pixel [154, 155] and frequency-division multiplexing (FDM) schemes with a large LC filter at every pixel [156, 157] are used to read out TES arrays. The advantage of low-frequency operation is that experimental techniques familiar in cryogenic detector work can be used, including low-power twisted-pair wiring and low-noise amplifiers with a few megahertz bandwidth. The disadvantage is that the filter elements required can be challenging (SQUID switches with relatively small inductive filters at every pixel for TDM, and large, but passive LC filters at every pixel for FDM), and the modest total bandwidth limits the number of signals that can be multiplexed in one wire.

At microwave frequencies, compact microwave filter elements can be used (either lumped or distributed elements), and the large total bandwidth makes it possible to multiplex more signals in each wire. However, microwave TES multiplexers are less mature, and the required room-temperature electronics are considerably more difficult. In a microwave SQUID multiplexer, a SQUID is placed at every pixel in a high-Q resonant

circuit [158]. In this approach, large arrays of SQUIDs could be frequency-division multiplexed into one coaxial cable with two additional coaxial cables to flux bias the SQUIDs. Hybrid schemes are also under development that use a low-frequency time-division multiplexer whose second-stage SQUIDs are frequency-division multiplexed in a microwave resonant circuit.

TES detectors have wideband noise, but only bandwidth-limited signals can be multiplexed without degradation. The development of a bandwidth-limiting filter is one of the most important considerations in implementing a multiplexing scheme. A variety of SQUID MUX schemes have been proposed that accept signal-to-noise ratio (SNR) degradation due to the absence of a bandwidth-limiting filter. For instance, the bias of multiple TES devices can be switched in a Hadamard code [159] and summed into a single SQUID. The signals can be demultiplexed using the Hadamard code, but the noise is increased by $\sqrt{N}$ due to aliasing of noise at frequencies above the Nyquist frequency associated with the frame rate (the rate at which the entire sequence of Hadamard codes is implemented). While approaches that accept significant SNR degradation are useful in some cases (e.g., when photon noise dominates), we focus here on multiplexing approaches that do not degrade the signal-to-noise ratio.

4.2.1 The Nyquist theorem and multiplexing

According to the Nyquist theorem, the information in a signal of bandwidth δf and duration δt can be exactly represented by $2\,\delta f\,\delta t$ real samples in time space. The same signal can be represented in frequency space as a Fourier series with $2\,\delta f\,\delta t$ real samples. The time and frequency samples form orthogonal basis sets to represent the bandwidth-limited function. Many other basis sets can also be used, such as Hadamard functions, wavelet-packet basis sets, or basis sets consisting of time samples within multiple frequency bands.

If an output SQUID channel has a bandwidth δF (larger than the signal bandwidth δf) it is possible, in principle, for the output to carry signals without degradation in $N \leq \delta F/\delta f$ different subsets of the output basis set. In order to multiplex, the bandwidth of the signal is limited by a filter, the information in each signal is moved to a different component of the output basis set (the signal is encoded), and the signals are summed in the output channel [157, 160]. The signals are encoded by multiplying them by a set of orthogonal modulation functions. The multiplication can be done either in the TES or the SQUID. In TDM, boxcar (low-duty-cycle square wave) modulation functions are used (Fig. 21). In FDM, sinusoids are used (Fig. 24). The signals are then added into one output channel. They can be separated and decoded using the same modulation functions. In the absence of SQUID noise, the fundamental limit on the number of signals that can be encoded in one output channel with a given bandwidth is independent of the choice of orthogonal basis set.

4.2.2 SQUID noise and multiplexing

Wideband SQUID noise is added to the signals after they are encoded. During decoding, all the noise outside of the noise bandwidth of the encoded signal is filtered out. The amount of noise that is added to the decoded signal depends on the noise bandwidth of the encoded signal. We assume here that the SQUID noise is white.

In TDM, the bandwidth of the encoded signal is set by the boxcar modulating function. In frequency space, the boxcar function is a sinc function, $F_{\mathrm{mod}}(f) = \sin(\pi f \delta t_s)/(\pi f \delta t_s)$, where δt_s is the time that the multiplexer dwells on one pixel. The noise bandwidth of the sinc function is

$$\delta B_{\mathrm{noise}} = \int_0^\infty \left(\frac{\sin(\pi f \delta t_s)}{\pi f \delta t_s} \right)^2 df = \frac{1}{2\delta t_{\mathrm{s}}} \; . \tag{115}$$

The noise above $\delta B_{\mathrm{noise}}$ is filtered by the sinc function in the process of decoding, either in an analog circuit (a gated integrator), or digitally, by averaging an oversampled signal. The "frame rate," $1/(N\delta t_{\mathrm{s}})$, is the rate at which all pixels are sampled. All the unfiltered noise above $1/(2N\delta t_{\mathrm{s}})$, the Nyquist frequency associated with the frame rate, is aliased into the signal band. The effective noise power of the SQUID is thus increased by a factor of $2N\delta t_{\mathrm{s}}/(2\delta t_{\mathrm{s}}) = N$. In order to maintain fixed SNR, the gain must be N times larger than it would be for a non-multiplexed TES: the number of turns on the SQUID input coil must be increased. SQUIDs are sufficiently quiet that, even with the required gain, it is possible to multiplex hundreds or thousands of signals into one output SQUID with TDM. Increasing the number of turns by

$\sqrt{N}$ to overcome the aliased SQUID noise also increases the required slew rate in the SQUID by $\sqrt{N}$. In applications with high dynamic range, such as fast x-ray calorimeter arrays, high-bandwidth feedback must be applied from room temperature to achieve sufficient slew rate.

In FDM, in contrast, the bandwidth of the encoded signal is the same as the bandwidth of the input signal. Multiplying by the modulating function, a sinusoid, moves the signal up to a high frequency but does not affect the bandwidth, and no aliasing of wideband SQUID noise occurs. However, in FDM, signals from all pixels are seen by the SQUID at all times. The slew rate requirements set by uncorrelated noise scales as $\sqrt{N}$, but the slew rate requirements due to the signal are typically more important. In a bolometer, if changes in the power seen by different pixels are uncorrelated, the slew rate requirements are modest. But if a common-mode power signal is seen in all detectors, the slew rate requirement on the SQUID increases as N, a more difficult slew-rate requirement than in TDM. This situation is expected, for instance, in a ground-based submillimeter camera when changes in the weather cause a common-mode signal on all pixels. In a calorimeter, the slew-rate requirement is determined by the characteristics of the source. If coincident pulses are not expected in different pixels, the slew rate requirements are again modest. But if coincident signals are commonplace, the slew rate requirements increase approximately linearly with the maximum number of coincident signals allowed.

4.2.3 Low-frequency TDM

Time-division SQUID multiplexers have been developed for applications ranging from biomagnetism [161] and non-destructive evaluation [162] to the readout of TES arrays [154], using both dc SQUIDs and rf SQUIDs [163]. In TES readout applications, each TES is biased by a voltage V with some load resistance R_{L} and connected to a SQUID "switch." The SQUIDs are turned on one at a time, and the outputs of many SQUIDs are added into one output channel.

The current noise of the TES is rolled off below the Nyquist frequency of the sampling in order to prevent degradation due to noise aliasing. From eqns. (94) and (35), the thermal-fluctuation noise in the TES, $S_{I_{\mathrm{TFN}}}(\omega)$, is naturally rolled off by a one pole filter at the pulse fall frequency, $1/(2\pi\tau_-)$ and a second pole at the pulse rise frequency $1/(2\pi\tau_+)$. However, from eqns. (89), (91) and (35), the TES Johnson noise $S_{I_{\mathrm{TES}}}(\omega)$ and load resistor Johnson noise $S_{I_{\mathrm{L}}}(\omega)$ are rolled off by only a single pole at $1/(2\pi\tau_-)$. Thus, the inductance in the loop (and consequently τ_-) must be large enough to avoid degradation due to aliasing of Johnson noise, yet still be small enough for stability. Often the critically damped condition is chosen to balance these constraints. Achieving critical damping sometimes requires adding an additional "Nyquist" inductor in the loop between the SQUID and the TES.

In first-generation "voltage summing" SQUID TDM, the modulation function is applied to the SQUID switches as a parallel address voltage to turn on a row of SQUIDs [154]. The SQUID output voltages in each column are summed into one output SQUID channel. Unfortunately, voltage-summing topologies are not practically scalable to two-dimensional arrays at temperatures well below 1 K. When wired in a two-dimensional array, parasitic currents in the two-dimensional network can lead to unacceptable crosstalk unless large address resistors are used to block the current flow. If large address resistors are used, there is unacceptably large Joule power dissipation. Second-generation SQUID TDM uses inductive summing of SQUID currents that prevents parasitic current flow without dissipation. This second-generation architecture is described here.

In "inductive summing" SQUID TDM [164, 155], boxcar address currents $I_1(t), I_2(t) \dots I_{\mathrm{N}}(t)$ are applied to turn on one row of M first-stage SQUIDs at a time (Fig. 21). An address resistor, R_A, shunts each first-stage SQUID. The value of the address resistor is typically chosen to be similar to the dynamic resistance of the SQUID to optimize a tradeoff between coupling, bandwidth, and Johnson noise currents from the address resistors. The current through the address resistor is inductively coupled through a summing coil to a second-stage SQUID shared by all the first-stage SQUIDs in a column. A separate wire can be run to room temperature for every address line, or the address currents can be provided by a CMOS multiplexer circuit cooled to 4 K [161].

A feedback flux is used to linearize the SQUID switches. Only one SQUID in a column is on at a time, so one feedback coil can be common to all SQUIDs in the column (Fig. (21)). The feedback is applied by room-temperature electronics that have an analog-digital converter (ADC), a field-programmable gate array (FPGA), and a digital-analog converter (DAC) for each multiplexed column [165]. When the SQUID
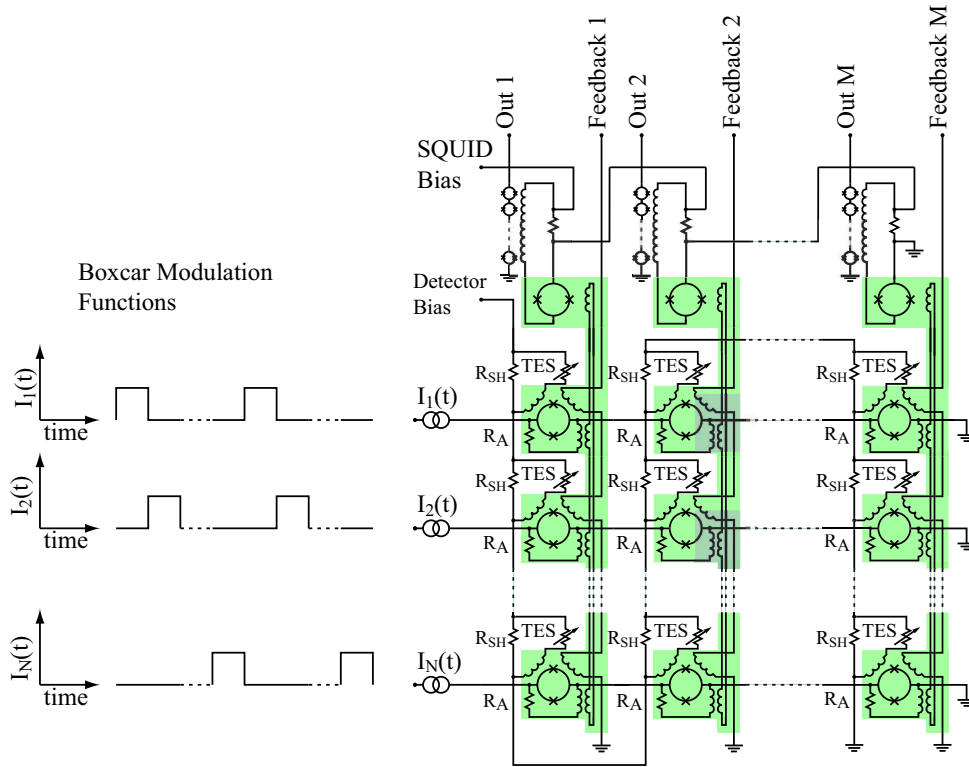
Figure 21: Two-dimensional multiplexing of a TES array with a time-division SQUID MUX. A common detector bias current is applied to all of the TESs in series. Each TES is wired in parallel with its own shunt resistor, $R_{\rm SH}$. Boxcar functions turn on one row of SQUID switches at a time. The outputs of all of the switches in a column are inductively summed into one output SQUID. A final series-array SQUID stage is used to amplify the signal before coupling to room-temperature electronics. A common feedback coil linearizes all SQUID switches in a column.
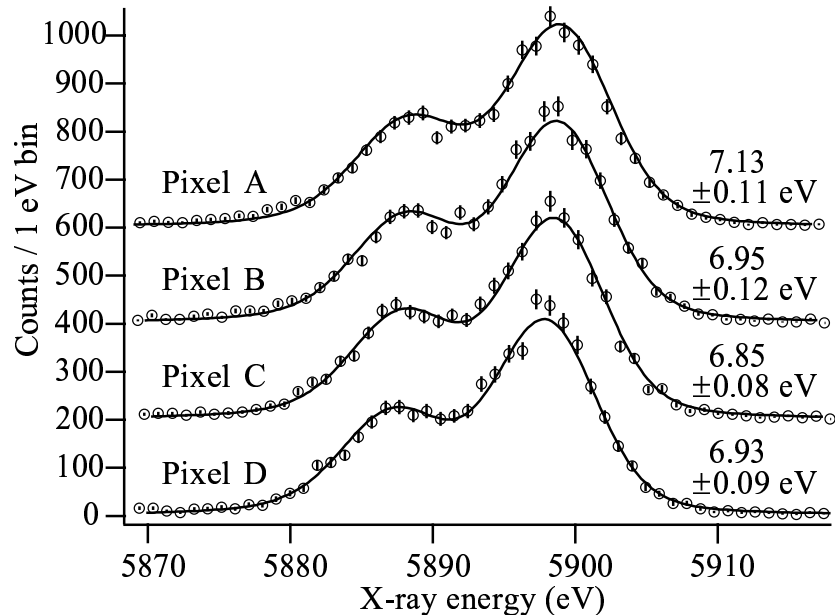
Figure 22: ^{55}Fe X-ray spectra measured simultaneously with an array of four TES x-ray calorimeters time-division multiplexed into one output channel. The spectra are offset vertically by 200 counts per eV. The data points are shown with statistical error bars, and the line is a fit to the Lorentzian natural linewidths of the Mn-Kα complex [135] convolved with a Gaussian detector response.

associated with a pixel is on, its output is measured by the ADC. The appropriate feedback signal to null the flux of the "on" SQUID is applied by the DAC to the common feedback coil. When the SQUID is turned off, the value of the DAC voltage required to null the SQUID flux is stored in the FPGA; the next time the pixel is turned on, the feedback algorithm is continued from the previous value of flux.

SQUID TDM has been used in FIBRE, an 8-pixel TES bolometer array in a submillimeter Fabry-Perot spectrometer. The SQUID multiplexer operated without significantly contributing to the noise of the bolometer [166]. FIBRE has been used in inital astronomical observations [28].

Doriese *et al.* have multiplexed four TES x-ray microcalorimeters in one output channel with good energy resolution [167]. The slight measured energy resolution degradation due to multiplexing (from $\approx$ 6.5 eV FWHM to $\approx$ 6.9 eV FWHM) is well understood, given the preliminary circuit parameters. Scaling to 32 pixels with less degradation is planned in a higher-bandwidth system.

A 1,280-pixel SQUID TDM chip has been developed for the SCUBA-2 instrument [29]. The SCUBA-2 MUX chip consists of 32 columns, each with 40 multiplexed SQUIDs (Fig. 23). The SCUBA-2 MUX chip is bump-bonded to a 1,280-pixel subarray of TES bolometers. The full SCUBA-2 instrument will combine 4 subarrays at 450 μm and 4 subarrays at 850 μm, for a total of 10,240 pixels.

SQUID TDM is being developed by groups at NIST, by Jena [168], and by Giessen [169]. It will be used in many instruments including a TES x-ray calorimeter array for NASA's Constellation-X observatory [30], an x-ray microanalysis array at NIST, SAFIRE [170], a 288-pixel first-light instrument on SOFIA, the Penn Array on the Green Bank Telescope [171], the Millimeter Bolometer Array Camera for the Atacama Cosmology Telescope [15], and SCUBA-2 [29], a 10,240-pixel submillimeter bolometer camera to be deployed at the James Clerk Maxwell Telescope in 2006.

Finally, it may be possible to implement SQUID TDM using digital SQUIDs with rapid single flux quantum (RSFQ) logic [172]. However, significant reduction in the power dissipation would be required to make digital SQUIDs practical for operation well below 1 K.
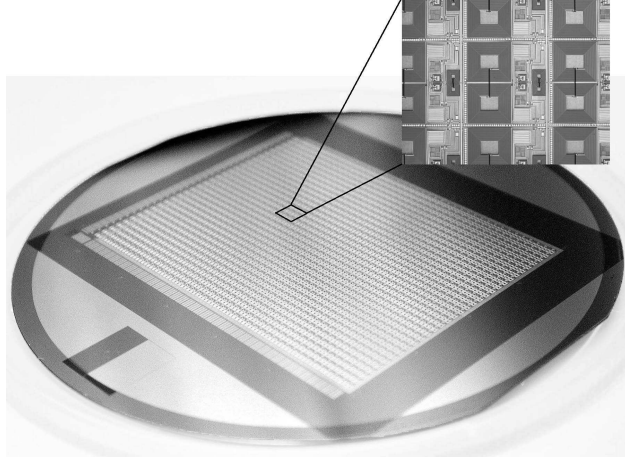
Figure 23: A 1,280-pixel SQUID TDM multiplexer for the SCUBA-2 instrument. The multiplexer wafer is bump-bonded to a TES array. 8 of these "subarray" modules make up the full instrument. Inset: a close view of a few of the MUX elements.

4.2.4 Low-frequency FDM

The first frequency-division SQUID multiplexers were developed for biomagnetism applications [173]. In these circuits, different sinusoidal modulation functions are applied as flux signals to multiple SQUIDs before their output voltage is summed. However, in the SQUID FDM circuits presently used for the readout of TES arrays, the modulation is applied to the bias of the TESs [156], and the output of multiple TES detectors in a row is summed into one SQUID. N different sinusoidal modulation functions, $I_1(t), I_2(t)$ ... $I_N(t)$, are applied to bias a row of N different TESs. The TES signals are thus moved up to a frequency band around their respective modulation, or "carrier" frequency.

The bandwidth of the signal and noise from each TES is limited by an LCR tank filter formed by a tuned inductor and capacitor at each pixel and the resistance of the TES (Fig. 24). Since the resonant frequency $\approx 1/(2\pi LC)$ is different for each pixel in the row, a single bias line can be used for an entire row. The bias line carries the sum of the modulation functions for all of the pixels (a "comb" in frequency space), but the LCR tank circuit for each pixel allows only the matched modulation frequency through to its respective TES.

In first-generation TES FDM, the outputs of the different TES channels is summed using a common transformer coil [156]. To improve the coupling efficiency, in present circuits (Fig. 24) the TES detectors are wired in parallel so that all of the signal currents are summed and flow through a common SQUID coil [174]. A feedback current is applied to each row SQUID to keep the total current through the SQUID coil fixed, providing a virtual ground that linearizes the SQUID and reduces crosstalk.

The amplitude of the carrier signals is generally larger than the low-frequency signals from the TESs. The combined carrier signals from all of the multiplexed TESs cause a significant flux slew rate in the SQUID and a large total flux swing. In order to reduce the required SQUID feedback slew rate, a carrier-nulling signal can be applied to the SQUID. All carrier-nulling signals for a row are applied to the row SQUID on one wire. The carrier-nulling signal is proportional to the carrier signal, but with phase and gain adjusted to minimize the load of the carrier on the SQUID (Fig. 24). Alternatively, the TES can be read out in a bridge configuration to null the carrier [175].

The resonant frequency of a series LRC resonator is $f \approx 1/(2\pi LC)$, and its bandwidth is $\delta B \approx R/(2\pi L)$. Low-frequency FDM requires large inductive and capacitive filter elements. Example values are $L = 40~\mu$H and $C = 0.64$ nF to 4.4 nF for operation at $f = 380$ kHz to 1 MHz [174]. The inductors are typically large spiral lithographic superconducting coils. To achieve the high required capacitance values, it is necessary to use either component capacitors connected to every pixel or lithographic capacitors with large chip areas, very thin dielectrics, or insulators with high dielectric constant (such as $SrTiO_3$ or Nb_2O_5). The loss in the dielectric must be small enough that the Q of the circuit is not degraded, which would widen the bandwidth
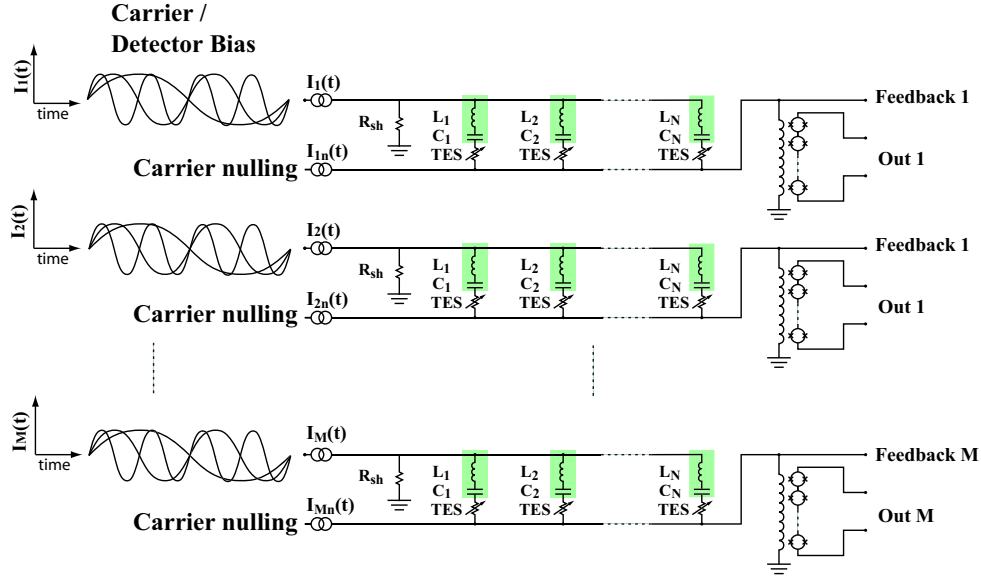
Figure 24: Two-dimensional multiplexing of a N×M TES array with a frequency-division SQUID MUX. N different sinusoidal carriers are applied on the bias line of a row of N TESs. Each TES in the row is part of an LCR tank circuit tuned to a different frequency. The current from all TESs is summed into the input coil of a series-array SQUID. A feedback signal is provided to make the input coil a virtual ground, and a carrier-nulling signal is provided to reduce the required SQUID flux slew rate.

of the filter. The Berkeley/LBNL group in collaboration with TRW has developed LC filter chips with 8 separate LC resonators (Fig. 25) on a 10 mm ×;10;mm chip.

The UC Berkeley/LBNL group has demonstrated the multiplexing of an array of 8 TES bolometers in one output channel without significant degradation in NEP [176]. A collaboration of LLNL and Berkeley/LBNL [17, 177] has demonstrated the multiplexing of two TES gamma-ray calorimeters without significant degradation in energy resolution due to the multiplexing (Fig. 26). The gamma-ray calorimeters in this experiment have an energy resolution of 60 eV at 60 keV.

Low-frequency SQUID FDM is being developed by groups at Berkeley/LBNL [156], VTT/SRON [157], LLNL [17], and ISAS [175]. These groups are planning to use this approach in several instruments to study the cosmic microwave background at millimeter wavelengths, including APEX-SZ [16], the South Pole Telescope, and POLARBEAR [178]. Low-frequency SQUID FDM is also planned for the European Space Agency's XEUS x-ray observatory [157].

4.2.5 Microwave SQUID multiplexer

SQUID multiplexers operated at microwave frequencies are being developed due to the promise of compact passive filter elements and large total bandwidth. They have significant advantages for reading out large TES arrays, but they are less mature than low-frequency multiplexers. Large arrays of SQUIDs operated at microwave frequencies could potentially be frequency-division multiplexed into one coaxial cable, with two additional coaxial cables used to flux bias the SQUIDs.

In a microwave reflectometer SQUID multiplexer [158], each SQUID is placed in a resonant circuit with a unique microwave resonant frequency. All of the resonant circuits are connected in parallel. A comb of microwave frequencies is used to simultaneously excite all resonant circuits. The amplitude and phase of the reflected microwave signal at each resonant frequency is a function of the magnetic flux in the associated SQUID, and thus of the current passing through the TES connected to its input coil. The reflected signal from all SQUIDs is summed into the input of one cryogenic high electron-mobility transistor (HEMT). Similar techniques have previously been used to multiplex the readout of single electron transistors [179] and kinetic inductance detectors [180]. This microwave reflectometer readout can be used with either dc or
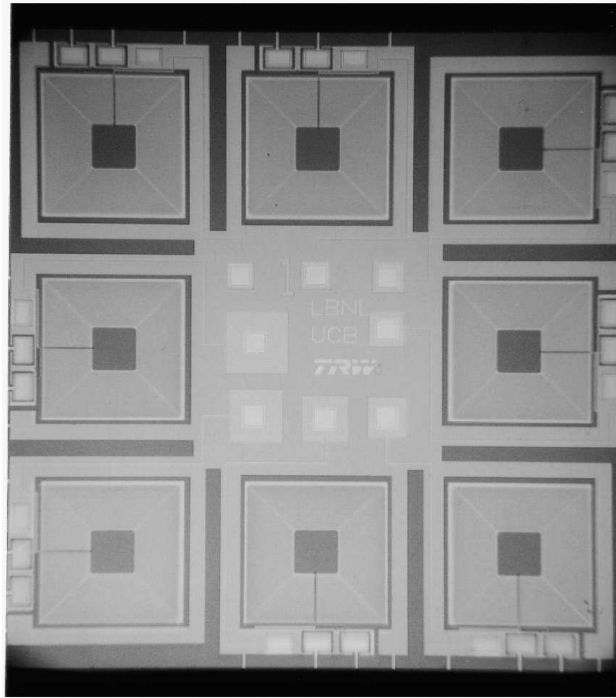
Figure 25: Photograph of niobium LC filter chip fabricated by TRW (now Northrup-Grumman). The filters consist of eight spiral inductors and eight parallel-plate capacitors with Nb_2O_5 dielectric. Photograph courtesy of Adrian Lee, UC Berkeley
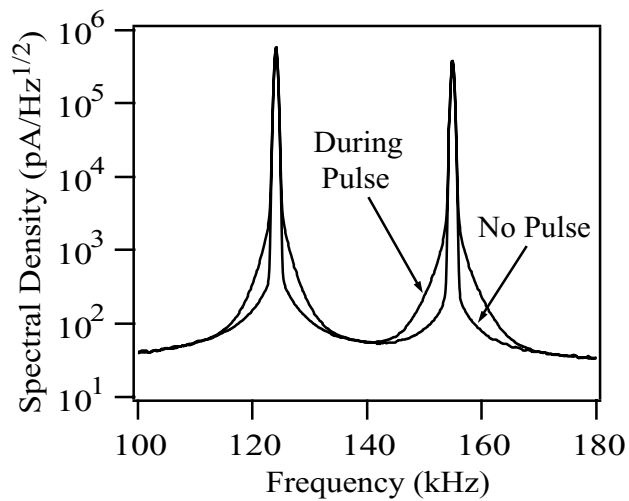

Figure 26: Frequency-space representation of data from two multiplexed TES gamma-ray calorimeters [17]. The two TESs are in separate LRC resonant circuits at two different resonant frequencies, 124 kHz and 154 kHz. At steady state, the peaks are sharp, with high Q. When a gamma ray is absorbed, the TES resistance increases and the peak broadens. Figure courtesy of J.N. Ullom, NIST (formerly LLNL).
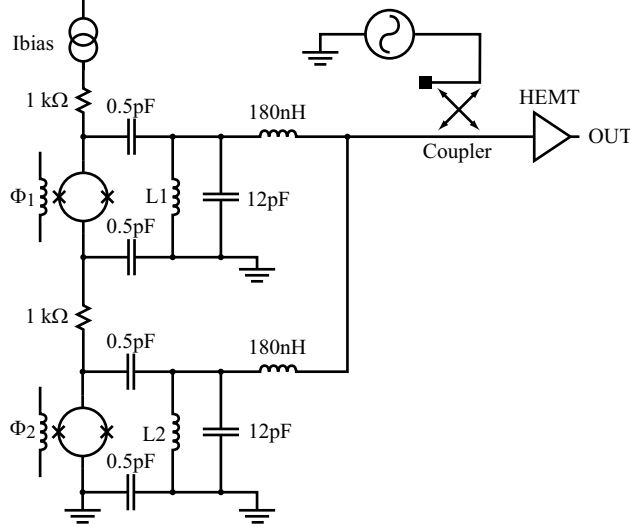
.

Figure 27: Resonant circuit used to demonstrate the multiplexed readout of two pixels. In the initial demonstration, component capacitors and inductors are used, and the resonant frequency is near 500 MHz. Future circuits will use lithographic elements (lumped or distributed) and will operate near 5 GHz.

rf SQUIDs.

Because SQUIDs have nonlinear periodic response functions, they are usually operated with flux feedback to linearize their response. In large arrays, however, it is impractical to provide a separate feedback line to every pixel. The SQUIDs in the microwave SQUID multiplexer are thus operated open-loop, without feedback. Open-loop operation is appropriate for applications with moderate dynamic range requirements, including the readout of most low-temperature detectors. Unlike low-frequency FDM schemes that couple many detectors and many carrier signals to one SQUID and thus require high dynamic range [156], the response of each SQUID in the microwave multiplexer can remain monotonic even with large signals in every detector. The signals are summed into a HEMT, which has large dynamic range. Operating open-loop leads to some nonlinearity in the SQUID response that must be corrected. In general, the response of a TES also has some nonlinearity that must be corrected. The software developed to correct the nonlinearity of the detectors can also be used to linearize the SQUIDs with no additional computational cost.

Microwave reflectometer readout of single SQUIDs has been demonstrated with good noise performance (flux noise $\approx 0.5\ \mu\Phi_0/\sqrt{\text{Hz}}$ at 4 K) and high bandwidth ($\sim 100\,\text{MHz}$) [158]. Furthermore, multiplexed readout of two SQUIDs has been demonstrated in a microwave reflectometer circuit. In this multiplexed circuit (Fig. 27), two SQUIDs were placed in circuits with different resonant frequencies and a loaded Q of 60. The resonant circuits transform the impedance of the SQUIDs to $\approx 50\,\Omega$. The reflected power at the two resonances is a function of the current through the input coil of the two SQUIDs (Fig. 28). Future circuits with lithographic filter elements are expected to have Qs of many thousands, allowing thousands of TES detectors to be multiplexed into one coaxial cable.

A microwave SQUID MUX is operated open-loop, but it is necessary to choose the flux bias of the SQUIDs to be on a sensitive, linear portion of the response curve. Time-division multiplexed circuits are being developed to flux bias each SQUID by trapping flux in a separate superconducting "flux-bias" coil coupled through an inductor, L_2, to the SQUID (Fig. 29). A flux-bias lead is inductively coupled to the flux-bias coil through inductor L_1 only when a heat-actuated superconducting switch is opened. In order to flux bias the SQUID, the heat switch is actuated (driving a resistor normal), and the flux-bias lead injects flux into the flux bias coil. The heat switch is then closed, trapping the appropriate flux in the flux-bias coil. An integral number of flux quanta are trapped in L_2 when the switch is closed. L_2 is only weakly coupled to the SQUID, so a large number of trapped flux quanta lead to only a fraction of a flux quantum in the SQUID. Thus, the flux bias can be set in fine steps.

The heat switches operate by using Joule power in a normal-metal film to heat the electrons in a superconducting film into the normal state. The structures are made small so that the thermal diffusion times
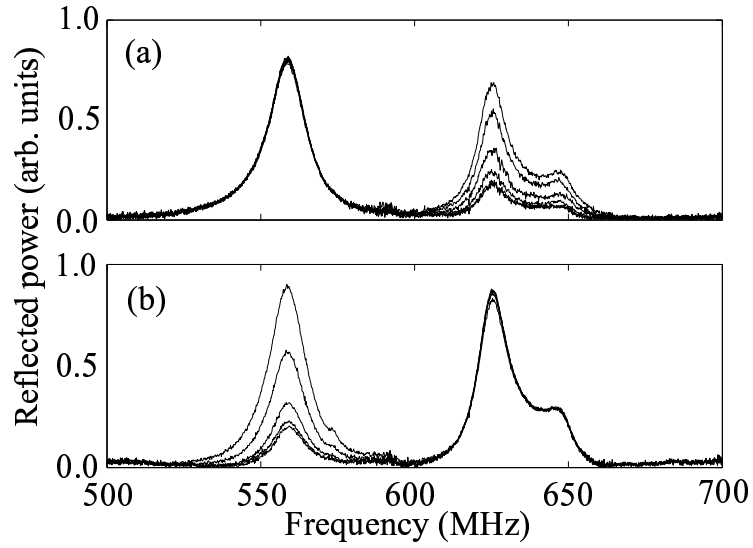
Figure 28: Differential measurement of the scattering of a microwave signal off the circuit in Fig. (27), relative to the signal when the SQUIDs are off. (**a**) A family of curves for different flux in SQUID 1. (**b**) A family of curves for different flux in SQUID 2. The high-frequency shoulder is due to a reflection in the HEMT output, which is out of the specified band.
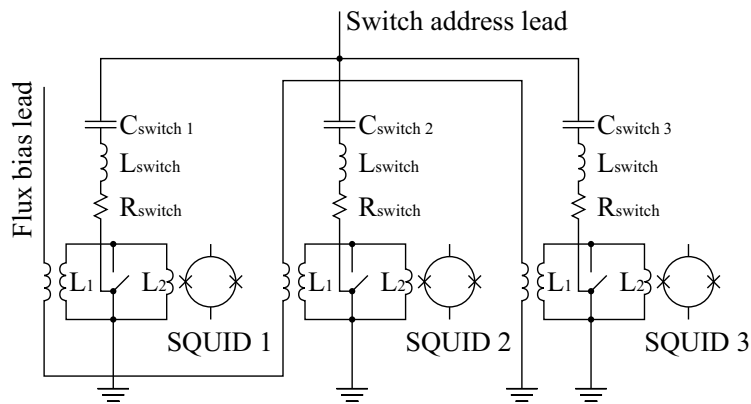

Figure 29: Array of persistent current flux-bias circuits. Each circuit is addressed by applying a different excitation frequency to the switch address lead (driving it normal) and applying flux to the flux-bias lead.

are fast enough for high-bandwidth operation, and the films are thin so that they can be heated with low applied power.

In an array, the heat-switch resistors are placed in high-Q LRC resonant circuits and driven normal using a microwave signal at the appropriate resonant frequency. All of the switch-address leads are tuned to different resonant frequencies and wired in parallel to a single coaxial cable (Fig. 29). The flux-bias lead passes in series through all of the flux-bias coils. When the array is turned on, the switches are addressed one at a time until the flux bias for the full array is set.

Once fully developed, the microwave SQUID multiplexer will allow much larger TES arrays to be operated with only three coaxial cables to the base temperature: one to carry the reflectometer signal, one to address the multiplexed flux bias circuit, and one to apply flux to the multiplexed flux bias circuit.

Finally, hybrid schemes implementing both microwave SQUID FDM and low-frequency TDM are being developed at NIST. In this approach, the second-stage SQUIDs in the standard low-frequency TDM circuit of Fig. 21 are multiplexed at microwave frequencies into a single HEMT amplifier. This hybrid FDM/TDM basis set is similar to that used in time-division multiple access (TDMA) cell phones, in which different frequency bands are time-division multiplexed. While requiring more leads than the standard microwave SQUID MUX (including an address line for every row and a feedback line for every column), the "TDMA" approach would allow linearized, high dynamic range operation for fast pulses, and high bandwidth per column (potentially 32 hundred-megahertz columns in an octave of bandwidth at $\sim 5 - 10\,\mathrm{GHz}$, for a total of over 1,000 SQUID channels in one HEMT amplifier).

5   Future Outlook

The last decade has seen explosive growth in the development and use of superconducting transition-edge sensors in a variety of applications. Dramatic progress has been made in single-pixel performance. Micromachined arrays of cryogenically multiplexed TES calorimeters have been developed. In spite of the recent progress, there is still significant room for improvement in our understanding of the noise processes in these devices, in the single-pixel performance, and in the scale of the TES arrays.

The fundamental source of the excess "electrical" noise observed in TES detectors is still not understood. A full thermodynamic analysis of the nonlinear, non-equilibrium TES thermal-electrical circuit has yet to be completed. A number of sources have been suggested for additional noise, including fluctuations in the order parameter, vortex flow in the Kosterlitz-Thouless transition, and noise in phase-slip lines (both noise in stable lines and noise due to phase-slip-line nucleation/denucleation or path instability). Both theoretical and experimental work is required to understand these noise processes. An understanding of the noise sources should result in designs with improved single-pixel performance.

The first TES arrays with more than a thousand pixels are now being fabricated. This number of pixels is sufficient for many future millimeter-wave cameras, where constraints on the size of the focal plane limit the number of pixels that can be used. Improvements in longer-wavelength instruments will likely result from improved absorbers, including antenna structures with polarization or frequency sensitivity. At shorter wavelengths, significantly larger pixel counts are desirable. The implementation of microwave readout techiques, such as the microwave SQUID multiplexer, may enable much larger arrays. For these larger arrays, it may be necessary to implement more intimate integration of the readout electronics and the TES pixels using techniques such as surface micromachining.

References

[1] H. Kamerlingh Onnes. *Leiden Comm.*, **120b** (1911).

[2] D.H. Andrews, W.F. Brucksch, W.T. Ziegler, and E.R. Blanchard. "Attenuated Superconductors i. For Measuring Infra-Red Radiation." *Rev. Sci. Instrum.*, **13**, 281 (1942).

[3] D.H. Andrews, R.D. Fowler, and M.C Williams. "The Effect of Alpha-particles on a Superconductor." *Phys. Rev.*, **76**(1), 154–155 (1949).

[4] D.H Andrews. *American Philisophical Yearbook*, p. 132 (1938).

[5] A. Goetz. "The Possible Use of Superconductivity for Radiometric Purposes." *Phys. Rev.*, **55**, 1270 (1939).

[6] M.K. Maul, M.W.P. Strandberg, and R.L. Kyhl. "Excess noise in superconducting bolometers." *Phys. Rev.*, **182**, 522 – 525 (1969).

[7] J. Clarke, P.L. Richards, and N.H. Yeh. "Composite Superconducting Transition Edge Bolometer." *Appl. Phys. Lett.*, **30**(12), 664 – 666 (1977).

[8] B. Neuhauser, B. Cabrera, C.J. Martoff, and B.A. Young. "Phonon-mediated detection of alpha particles with aluminum transition edge sensors." *Japanese Journal of Applied Physics, Supplement*, **26**(suppl.26-3, pt.2), 1671 – 1672 (1987).

[9] B.A. Young, B. Cabrera, A.T. Lee, C.J. Martoff, B. Neuhauser, and J.P. McVittie. "Phonon-mediated detection of X-rays in silicon crystals using superconducting transition edge phonon sensors." *IEEE Transactions on Magnetics*, **25**(2), 1347 – 1350 (1989).

[10] John Clarke and Alex I. Braginski. *The SQUID Handbook: Volume 1: Fundamentals and Technology of SQUIDs and SQUID Systems*. Wiley (2004).

[11] W. Seidel, G. Forster, W. Christen, F. von Feilitzsch, H. Gobel, F. Probst, and R.L. Mossbauer. "Phase transition thermometers with high temperature resolution for calorimetric particle detectors employing dielectric absorbers." *Phys. Lett. B*, **236**, 483–487 (1990).

[12] K.D. Irwin, S.W. Nam, B. Cabrera, B. Chugg, G.S. Park, R.P. Welty, and J.M. Martinis. "A self-biasing cryogenic particle detector utilizing electrothermal feedback and a SQUID readout." *IEEE Trans. Appl. Supercond.*, **5**(2 pt.3), 2690 – 2693 (1995).

[13] K.D. Irwin. "An application of electrothermal feedback for high resolution cryogenic particle detection." *Appl. Phys. Lett.*, **66**(15), 1998 – 2000 (1995).

[14] A.T. Lee, P.L. Richards, Sae Woo Nam, B. Cabrera, and K.D. Irwin. "A superconducting bolometer with strong electrothermal feedback." *Appl. Phys. Lett.*, **69**(12), 1801 – 1803 (1996).

[15] A. Kosowsky. "The Atacama Cosmology Telescope." *New Astron. Rev.*, **47**(11-12), 939 – 943 (2003).

[16] D. Schwan, F. Bertoldi, S. Cho, M. Dobbs, R. Guesten, N.W. Halverson, W.L. Holzapfel, E. Kreysa, T.M. Lanting, A.T. Lee, M. Lueker, J. Mehl, K. Menten, D. Muders, M. Myers, T. Plagge, A. Raccanelli, P. Schilke, P.L. Richards, H. Spieler, and M. White. "APEX-SZ: a Sunyaev-Zel'dovich galaxy cluster survey." *New Astron. Rev.*, **47**(11-12), 933 – 937 (2003).

[17] M.F. Cunningham, J.N. Ullom, T. Miyazaki, S.E. Labov, J. Clarke, T.M. Lanting, A.T. Lee, P.L. Richards, Jongsoo Yoon, and H. Spieler. "High-resolution operation of frequency-multiplexed transition-edge photon sensors." *Appl. Phys. Lett.*, **81**(1), 159 – 161 (2002).

[18] T. Miyazaki, Joel.N. Ullom, Mark.F. Cunningham, and S.E. Labov. "Noise analysis of gamma-ray TES microcalorimeters with a demonstrated energy resolution of 52 eV at 60 keV." *IEEE Trans. Appl. Supercond.*, **13**(2), 630 – 633 (2003).

[19] B. Cabrera, L.M. Krauss, and F. Wilczek. "Bolometric detection of neutrinos." *Phys. Rev. Lett.*, **55**, 25 – 28 (1985).

[20] D. Bassi, A. Boschetti, M. Scontoni, and M. Zen. "Molecular-beam diagnostics by means of fast superconducting bolometer and infrared laser." *Appl. Phys. B*, **26**(3), 99 –103 (1981).

[21] D. Twerenbold, J. Vuilleumier, D.l Gerber, A. Tadsen, B. van den Brandt, and P.M. Gillevet. "detection of single macromolecules using a cryogenic particle detector coupled to a biopolymer mass spectrometer." *Appl. Phys. Lett.*, **68**, 3503–3505 (1996).

[22] G.C. Hilton, J.M. Martinis, D.A. Wollman, K.D. Irwin, L.L. Dulcie, D. Gerber, P.M. Gillevet, and D. Twerenbold. "Impact energy measurement in time-of-flight mass spectrometry with cryogenic microcalorimeters." *Nature*, **391**(6668), 672 – 675 (1998).

[23] R. Abusaidi, D.S. Akerib, Jr. Barnes, P.D., D.A. Bauer, A. Bolozdynya, P.L. Brink, R. Bunker, B. Cabrera, D.O. Caldwell, J.P. Castle, R.M. Clarke, P. Colling, M.B. Crisler, A. Cummings, A. Da Silva, A.K. Davies, R. Dixon, B.L. Dougherty, D. Driscoll, S. Eichblatt, J. Emes, R.J. Gaitskell, S.R. Golwala, D. Hale, E.E. Haller, J. Hellmig, M.E. Huber, K.D. Irwin, J. Jochum, F.P. Lipschults, A. Lu, V. Mandic, J.M. Martinis, S.W. Nam, H. Nelson, B. Neuhauser, M.J. Penn, T.A. Perera, M.C. Perillo Isaac, B. Pritychenko, R.R. Ross, T. Saab,

B. Sadoulet, R.W. Schnee, D.N. Seitz, P. Shestople, T. Shutt, A. Smith, G.W. Smith, A.H. Sonnenschein, A.L. Spadafora, W. Stockwell, J.D. Taylor, S. White, S. Yellin, and B.A. Young. "Exclusion limits on the WIMP-nucleon cross section from the cryogenic dark matter search." *Physical Review Letters*, **84**(25), 5699 – 5703 (2000).

[24] G. Angloher, M. Bruckmayer, C. Bucci, M. Buhler, S. Cooper, C. Cozzini, P. DiStefano, F. von Feilitzsch, T. Frank, D. Hauff, Th. Jagemann, J. Jochum, V. Jorgens, R. Keeling, H. Kraus, M. Loidl, J. Marchese, O. Meier, U Nagel, F. Probst, Y. Ramachers, A. Rulofs, J. Schnagl, W. Seidel, I. Sergeyev, M. Sisti, M. Stark, S. Uchaikin, L. Stodolsky, H. Wulandari, and L. Zerle. "Limits on wimp dark matter using sapphire cryogenic detectors." *Astroparticle Physics*, **18**(1), 43 – 55 (2002).

[25] D.A. Wollman, K.D. Irwin, G.C. Hilton, L.L. Dulcie, D.E. Newbury, and J.M. Martinis. "High-resolution, energy-dispersive microcalorimeter spectrometer for X-ray microanalysis." *J. Microsc.*, **188**, 196 – 223 (1997).

[26] A.J. Miller, S.W. Nam, J.M. Martinis, and A.V. Sergienko. "Demonstration of a low-noise near-infrared photon counter with multiphoton discrimination." *Appl. Phys. Lett.*, **83**(4), 791 – 793 (2003).

[27] B. Cabrera, R.M. Clarke, P. Colling, A.J. Miller, S. Nam, and R.W. Romani. "Detection of single infrared, optical, and ultraviolet photons using superconducting transition edge sensors." *Appl. Phys. Lett.*, **73**(6), 735 – 737 (1998).

[28] D.J. Benford, T.A. Ames, J.A. Chervenak, E.N. Grossman, K.D. Irwin, S.A. Khan, B. Maffei, S.H. Moseley, F. Pajot, T.G. Phillips, J.-C. Renault, C.D. Reintsema, C. Rioux, R.A. Shafer, J.G. Staguhn, C. Vastel, and G.M. Voellmer. "First astronomical use of multiplexed transition edge bolometers." *AIP Conf. Proc.*, **605**, 589 – 592 (2002).

[29] W.S. Holland, W.D. Duncan, B.D. Kelly, K.D. Irwin, A.J. Walton, P.A.R. Ade, and E.I. Robson. "SCUBA-2: a large format submillimetre camera on the James Clerk Maxwell Telescope." *Proc. SPIE*, **4855**, 1 – 18 (2003).

[30] N.E. White and H. Tananbaum. "The Constellation X-ray mission." *Nucl. Instrum. Methods Phys. Res. A*, **436**(1-2), 201 – 204 (1999).

[31] J. Bardeen, L.N. Cooper, and J.R. Schreiffer. "Theory of Superconductivity." *Phys. Rev.*, **108**(5), 1175 – 1204 (1957).

[32] V.L. Ginzburg and L.D. Landau. *Zh. Eksperim. i Teor. Fiz.*, **20**, 1064 (1950).

[33] L.P. Gor'kov. *Zh. Eksperim. i Teor. Fiz.*, **36**, 1918 (1959).

[34] Michael Tinkham. *Introduction to Superconductivity*. McGraw-Hill, 2nd ed. (1995).

[35] M.R. Beasley, J.E. Mooij, and T.P. Orlando. "Possibility of Vortex-Antivortex Pair Dissociation in Two-Dimensional Superconductors." *Phys. Rev. Lett.*, **42**(17), 1165 –1168 (1979).

[36] S. Doniach and B.A. Huberman. "Topological Excitations in Two-Dimensional Superconductors." *Phys. Rev. Lett.*, **42**(17), 1169 – 1172 (1979).

[37] W.A. Little. "Decay of Persistent Currents in Small Superconductors." *Phys. Rev.*, **156**(2), 396 – 403 (1967).

[38] J.E. Lukens, R.J. Warburton, and W.W. Webb. "Onset of Quantized Thermal Fluctuations in "One-Dimensional" Superconductors." *Phys. Rev. Lett.*, **25**(17), 1180 – 1184 (1970).

[39] R.S. Newbower, M.R Beasley, and M. Tinkham. "Fluctuation Effects on the Superconducting Transition of Tin Whisker Crystals." *Phys. Rev. B*, **5**(3), 864 – 868 (1972).

[40] K.D. Irwin, G.C. Hilton, D.A. Wollman, and J.M. Martinis. "Thermal-response time of superconducting transition-edge microcalorimeters." *J. Appl. Phys.*, **83**(8), 3978 – 3985 (1998).

[41] W.J. Skocpol, M.R. Beasley, and M. Tinkham. "Phase-slip centers and nonequilibrium processes in superconducting tin microbridges." *J. Low Temp. Phys.*, **16**(1-2), 145 – 167 (1974).

[42] J. Clarke and J.L. Paterson. "Josephson-Junction Amplifier." *Appl. Phys. Lett.*, **19**(11), 469 – 471 (1971).

[43] M. Kiviranta and H. Seppa. "Dc-squid electronics based on the noise cancellation scheme." *IEEE Trans. Appl. Supercond.*, **5**(2), 2146 – 2148 (1995).

[44] R.P. Welty and J.M. Martinis. "A series array of DC SQUIDs." *IEEE Transactions on Magnetics*, **27**(2 pt.4), 2924 – 2926 (1991).

[45] R.P. Welty and J.M. Martinis. "Two-stage integrated SQUID amplifier with series array output." *IEEE Trans. Appl. Supercond.*, **3**(1, pt. 4), 2605 – 2608 (1993).

[46] M.E. Huber, P.A. Neil, R.G. Benson, D.A. Burns, A.F. Corey, C.S. Flynn, Y. Kitaygorodskaya, O. Massihzadeh, J.M. Martinis, and G.C. Hilton. "DC SQUID series array amplifiers with 120 MHz bandwidth (corrected)." *IEEE Trans. Appl. Supercond.*, **11**(2), 4048 – 4053 (2001).

[47] K.D. Irwin. *Phonon-Mediated Particle Detection Using Superconducting Tungsten Transition-Edge Sensors*. Ph.D. thesis, Stanford University (1995).

[48] M.A. Lindeman. *Microcalorimetry and the Transition-Edge Sensor*. Ph.D. thesis, University of California at Davis (2000).

[49] J.C. Mather. "Bolometer Noise - Non-Equilibrium Theory." *Appl. Optics*, **21**(6), 1125 –1129 (1982).

[50] J.C. Mather. "Bolometers - Ultimate Sensitivity, Optimization, and Amplifier Coupling." *Appl. Optics*, **23**(4), 584 –588 (1984).

[51] S.H. Moseley, J.C. Mather, and D. McCammon. "Thermal detectors as X-ray spectrometers." *J. Appl. Phys.*, **56**(5), 1257 – 1262 (1984).

[52] M.A. Lindeman, S. Bandler, R.P. Brekosky, J.A. Chervenak, E. Figueroa-Feliciano, F.M. Finkbeiner, M.J. Li, and C.A. Kilbourne. "Impedance measurements and modeling of a transition-edge-sensor calorimeter." *Rev. Sci. Instrum.*, **75**(5), 1283 – 1289 (2004).

[53] Enectalí Figueroa Feliciano. *Theory and development of position-sensitive quantum calorimeters*. Ph.D. thesis, Stanford University (2001).

[54] L.D. Landau and E.M. Lifshitz. *Statistical Physics*. Addison-Wesley Publishing Company, Reading, Massachusetts, first ed. (1958).

[55] R.L. Stratonovich. *Nonlinear Nonequilibrium Thermodynamics I: Linear and Nonlinear Fluctuation-Dissipation Theorems*. Springer-Verlag, Berlin, first ed. (1992).

[56] C. Kittel and H. Kroemer. *Thermal Physics*. W.H. Freeman and Company, New York, second ed. (1980).

[57] H.B. Callen and R.F. Greene. "On a Theorem of Irreversible Thermodynamics." *Phys. Rev.*, **86**(5), 702 – 710 (1952).

[58] R.F. Greene and H.B. Callen. "On a Theorem of Irreversible Thermodynamics. II." *Phys. Rev.*, **88**(6), 1387 – 1391 (1952).

[59] W.S. Boyle and K.F. Rodgers. "Performance characteristics of a new low-temperature bolometer." *J. Opt. Soc. Am.*, **49**, 66 (1959).

[60] Jr. Wyatt, J.L. and G.J Coram. "Nonlinear device noise models: Satisfying the thermodynamic requirements." *IEEE Trans. Elect. Dev.*, **46**(1), 184 – 193 (1999).

[61] R.L. Stratonovich. *Izv. VUZ Radiofizika*, **13**, 1512 (1970).

[62] H.F.C. Hoevers, A.C. Bento, M.P. Bruijn, L. Gottardi, M.A.N. Korevaar, W.A. Mels, and P.A.J. de Korte. "Thermal fluctuation noise in a voltage biased superconducting transition edge thermometer." *Appl. Phys. Lett.*, **77**(26), 4422 – 4424 (2000).

[63] J.M. Gildemeister, A.T. Lee, and P.L. Richards. "Model for excess noise in voltage-biased superconducting bolometers." *Appl. Opt.*, **40**(34), 6229 – 6235 (2001).

[64] C.M. Knoedler. "Phase-slip shot noise contribution to excess noise in superconducting bolometers." *J. Appl. Phys.*, **54**(5), 2773 – 2776 (1983).

[65] G. C. Hilton, K. D. Irwin, J. M. Martinis, and D. A. Wollman. "Superconducting transition-edge sensor with weak links." U.S. Patent 6,239,431 (2001).

[66] J.N. Ullom, W.B. Doriese, G.C. Hilton, J.A. Beall, S. Deiker, K.D. Irwin, C.D. Reintsema, L.R. Vale, and Y. Xu. "Suppression of excess noise in Transition-Edge Sensors using magnetic field and geometry." *Nucl. Instrum. Methods Phys. Res. A*, **520**(1-3), 333 – 335 (2004).

[67] J.G. Staguhn, S.H. Moseley, B.J. Benford, C.A. Allen, J.A. Chervenak, T.R. Stevenson, and W.T. Hsieh. "Approaching the fundamental noise limit in Mo/Au TES bolometers with transverse normal metal bars." *Nucl. Instrum. Methods Phys. Res. A*, **520**(1-3), 336 – 339 (2004).

[68] J.N. Ullom, W.B. Doriese, G.C. Hilton, J.A. Beall, S. Deiker, W.D. Duncan, L. Ferreira, K.D. Irwin, C.D. Reintsema, and L.R. Vale. "Characterization and reduction of unexplained noise in superconducting transition-edge sensors." *Appl. Phys. Lett.*, **84**(21), 4206 – 4208 (2004).

[69] G.M. Seidel and I.S. Beloborodov. "Intrinsic excess noise in a transition edge sensor." *Nucl. Instrum. Methods Phys. Res. A*, **520**(1-3), 325 – 328 (2004).

[70] A. Luukanen, K.M. Kinnunen, A.K. Nuottajarvi, H.F.C. Hoevers, W.M.B. Tiest, and J.P. Pekola. "Fluctuation-limited noise in a superconducting transition-edge sensor." *Phys. Rev. Lett.*, **90**(23), 238306 (2003).

[71] M.L. Lindeman. "A geometrical model of excess noise in transition edge sensors and related experiments." (2004). Talk at the 2nd TES Workshop at the University of Miami.

[72] G. C. Hilton, J. M. Martinis, K. D. Irwin, and D. A. Wollman. "Normal metal boundary conditions for multi-layer tes detectors." U.S. Patent 6,455,849 (2002).

[73] G.C. Hilton, J.M. Martinis, K.D. Irwin, N.F. Bergren, D.A. Wollman, M.E. Huber, S. Deiker, and S.W. Nam. "Microfabricated transition-edge x-ray detectors." *IEEE Trans. Appl. Supercond.*, **11**(1), 739 – 742 (2001).

[74] W.M. Bergmann Tiest, H.F.C. Hoevers, W.A. Mels, M.L. Ridder, M.P. Bruijn, P.A.J. de Korte, and M.E. Huber. "Performance of X-ray microcalorimeters with an energy resolution below 4.5 eV and 100 mu s response time." *AIP Conf. Proc.*, **605**, 199 – 202 (2002).

[75] M. Galeazzi, F. Zuo, C. Chen, and E. Ursino. "Intrinsic noise sources in superconductors near the transition temperature." *Nucl. Instrum. Methods Phys. Res. A*, **520**(1-3), 344 – 347 (2004).

[76] R.P. Huebener and D.E. Gallus. "Current-induced intermediate state in thin-film type-I superconductors: electrical resistance and noise." *Phys. Rev. B.*, **7**(9), 4089 – 4099 (1973).

[77] G.W. Fraser. "On the nature of the superconducting-to-normal transition in transition edge sensors." *Nucl. Instrum. Methods Phys. Res. A*, **523**(1-2), 234 – 245 (2004).

[78] J. Chervenak, D.J. Benford, S.H. Moseley, and K.D. Irwin. "Dual Transition Edge Sensor Bolometers for Enhanced Dynamic Range." *Proceedings of the Second Workshop on New Concepts for Far-Infrared and Sub-millimeter Space Astronomy*, pp. 378 – 381 (2002).

[79] C.L. Hunt, P.D. Mauskopf, and A.L. Woodcraft. "A tes development and test facility at cardiff, and a solution to the optical saturation problem of superconducting bolometers." *Proc. SPIE*, **5498**, 318 – 321 (2004).

[80] D.J. Fixsen, S.H. Moseley, B. Cabrera, and E. Figueroa-Feliciano. "Optimal Fitting of Non-linear Detector Pulses with Nonstationary Noise." *AIP Conf. Proc.*, **605**, 339 – 342 (2002).

[81] D.J. Fixsen, S.H. Moseley, B. Cabrera, and E. Figueroa-Feliciano. "Pulse estimation in nonlinear detectors with nonstationary noise." *Nucl. Instrum. Methods Phys. Res. A*, **520**(1-3), 555 – 558 (2004).

[82] U. Nagel, A. Nowak, H.J. Gebauer, P. Colling, S. Cooper, D. Dummer, P. Ferger, M. Frank, J. Igalson, A. Nucciotti, F. Probst, W. Seidel, E. Kellner, F.v. Feilitzsch, and G. Forster. "Proximity effect in iridium-gold bilayers." *J. Appl. Phys.*, **76**(7), 4262 – 4266 (1994).

[83] B.A. Young, T. Saab, B. Cabrera, J.J. Cross, R.M. Clarke, and R.A. Abusaidi. "Measurement of T_c suppression in tungsten using magnetic impurities." *J. Appl. Phys.*, **86**(12), 6975 – 6978 (1999).

[84] B.A. Young, T. Saab, B. Cabrera, J.J. Cross, and R.A. Abusaidi. "T_c tuning of tungsten transition edge sensors using iron implantation." *Nucl. Instrum. Methods Phys. Res. A*, **444**(1-2), 296 – 299 (2000).

[85] K.D. Irwin, B. Cabrera, B. Tigner, and S. Sethuraman. "Tungsten Thin Films for Use in Cryogenic Particle Detectors." *Proceedings of the 4th International Workshop on Low Temperature Detectors for Neutrinos and Dark Matter (LTD 4)*, p. 290 (1992).

[86] P. Ferger, P. Colling, C. Bucci, A. Nucciotti, M. Buhler, S. Cooper, F. vonFeilitzsch, G. Forster, A. Gabutti, J. Hohne, J. Igalson, E. Kellner, M. Loidl, O. Meier, U. Nagel, F. Probst, A. Rulofs, U. Schanda, W. Seidel, M. Sisti, L. Stodolsky, A. Stolovich, and L. Zerle. "Cryogenic particle detectors with superconducting phase transition thermometers." *Nucl. Instrum. Methods Phys. Res. A*, **370**(1), 157 – 159 (1996).

[87] K.D. Irwin, S.W. Nam, B. Cabrera, B. Chugg, and B.A. Young. "A quasiparticle-trap-assisted transition-edge sensor for phonon-mediated particle detection." *Rev. Sci. Inst.*, **66**(11), 5322 – 5326 (1995).

[88] B.A. Young, S.W. Nam, P.L. Brink, B. Cabrera, B. Chugg, R.M. Clarke, A.K. Davies, and K.D. Irwin. "Technique for fabricating tungsten thin film sensors with $T_c \leq 100$ mK on germanium and silicon substrates [dark matter detectors]." *IEEE Trans. Appl. Supercond.*, **7**(2), 3367 – 3370 (1997).

[89] A.E. Lita, D. Rosenberg, S. Nam, A.J. Miller, A. Salminen, R.E. Schwall, and D. Balzar. "Tuning Of Tungsten Thin Film Superconducting Transition Temperature For Fabrication Of Photon Number Resolving Detectors." (2004). Presented at the Applied Superconductivity Conference, Oct 4-8, 2004.

[90] S.F. Lee, J.M. Gildemeister, W. Holmes, A.T. Lee, and P.L. Richards. "Voltage-biased superconducting transition-edge bolometer with strong electrothermal feedback operated at 370 mK." *Appl. Optics*, **37**(16), 3391 – 3397 (1998).

[91] J. Hohne, M. Altmann, G. Angloher, P. Hettl, J. Jochum, T. Nussle, S. Pfnur, J. Schnagl, M.L. Sarsa, S. Wanninger, and F. van Feilitzsch. "High-resolution X-ray spectrometry using iridium-gold phase transition thermometers." *X-Ray Spectrom.*, **28**(5), 396 – 398 (1999).

[92] K.D. Irwin, G.C. Hilton, J.M. Martinis, and B. Cabrera. "A hot-electron microcalorimeter for X-ray detection using a superconducting transition edge sensor with electrothermal feedback." *Nucl. Instrum. Methods Phys. Res. A*, **370**(1), 177 – 179 (1996).

[93] K.D. Irwin, G.C. Hilton, D.A. Wollman, and J.M. Martinis. "X-ray detection using a superconducting transition-edge sensor microcalorimeter with electrothermal feedback." *Appl. Phys. Lett.*, **69**(13), 1945 – 1947 (1996).

[94] C.L. Hunt, J.J. Bock, P.K. Day, A. Goldin, A.E. Lange, H.G. LeDuc, A. Vayonakis, and J. Zmuidzinas. "Transition-edge superconducting antenna-coupled bolometer." *Proc. SPIE*, **4855**, 318 – 321 (2003).

[95] F.M. Finkbeiner, T.C. Chen, S. Aslam, E. Figueroa-Feliciano, R.L. Kelley, M. Li, D.B. Mott, C.K. Stahle, and C.M. Stahle. "Fabrication of superconducting bilayer transition edge thermometers and their application for spaceborne X-ray microcalorimetry." *IEEE Trans. Appl. Supercond.*, **9**(2, pt.3), 2940 – 2942 (1999).

[96] K.D. Irwin, G.C. Hilton, J.M. Martinis, S. Deiker, N. Bergren, S.W. Nam, D.A. Rudman, and D.A. Wollman. "A Mo-Cu superconducting transition-edge microcalorimeter with 4.5 eV energy resolution at 6 keV." *Nucl. Instrum. Methods Phys. Res. A*, **444**(1-2), 184 – 187 (2000).

[97] D.T. Chow, M.A. Lindeman, M.F. Cunningham, M. Frank, Jr. Barbee, T.W., and S.E. Labov. "Gamma-ray spectrometers using a bulk Sn absorber coupled to a Mo/Cu multilayer superconducting transition edge sensor." *Nucl. Instrum. Methods Phys. Res. A*, **444**(1-2), 196 – 200 (2000).

[98] F.B. Kiewiet, M.P. Bruijn, H.F.C. Hoevers, A.C. Bento, W.A. Mels, and P.A.J. de Korte. "Fabrication and characterization of infrared and sub-mm spiderweb bolometers with low-T_c superconducting transition edge thermometers." *IEEE Trans. Appl. Supercond.*, **9**(2), 3862 – 3865 (1999).

[99] J.M. Martinis, G.C. Hilton, K.D. Irwin, and D.A. Wollman. "Calculation of T_c in a normal-superconductor bilayer using the microscopic-based Usadel theory." *Nucl. Instrum. Methods Phys. Res. A*, **444**(1-2), 23 – 27 (2000).

[100] G. Brammertz, A.A. Golubov, P. Verhoeve, R. den Hartog, A. Peacock, and H. Rogalla. "Critical temperature of superconducting bilayers: Theory and experiment." *Appl. Phys. Lett.*, **80**(16), 2955 – 2957 (2002).

[101] B.A. Young, J.R. Williams, S.W. Deiker, S.T. Ruggiero, and B. Cabrera. "Using ion implantation to adjust the transition temperature of superconducting films." *Nucl. Instrum. Methods Phys. Res. A*, **520**(1-3), 307 – 310 (2004).

[102] S.T. Ruggiero, A. Williams, W.H. Rippard, A. Clark, S.W. Deiker, L.R. Vale, and J.N. Ullom. "Dilute Al-Mn alloys for low-temperature device applications." *J. Low Temp. Phys.*, **134**(3-4), 973 – 984 (2004).

[103] S.T. Ruggiero, A. Williams, W.H. Rippard, A.M. Clark, S.W. Deiker, B.A. Young, L.R. Vale, and J.N. Ullom. "Dilute Al-Mn alloys for superconductor device applications." *Nucl. Instrum. Methods Phys. Res. A*, **520**(1-3), 274 – 276 (2004).

[104] S.W. Deiker, W. Doriese, G.C. Hilton, K.D. Irwin, W.H. Rippard, J.N. Ullom, L.R. Vale, S.T. Ruggiero, A. Williams, and B.A. Young. "Superconducting transition edge sensor using dilute AlMn alloys." *Appl. Phys. Lett.*, **85**(11), 2137–2139 (2004).

[105] P.M. Downey, A.D. Jeffries, S.S. Meyer, R. Weiss, F.J. Bachner, J.P. Donnelly, W.T. Lindley, R.W. Mountain, and D.J. Silversmith. "Monolithic Silicon Bolometers." *Appl. Optics*, **23**(6), 910 – 914 (1984).

[106] J. J. Bock, D. Chen, P. D. Mauskopf, and A. E. Lange. "a novel bolometer for infrared and millimeter-wave astrophsics." *Space Science Reviews*, **74**(1-2), 229–235 (1995).

[107] C.K. Stahle, R.L. Kelley, D. McCammon, S.H. Moseley, and A.E. Szymkowiak. "Microcalorimeter arrays for high resolution soft X-ray spectroscopy." *Nucl. Instrum. Methods Phys. Res. A*, **370**(1), 173 – 176 (1996).

[108] J.M. Gildemeister, A.T. Lee, and P.L. Richards. "A fully lithographed voltage-biased superconducting spiderweb bolometer." *Appl. Phys. Lett.*, **74**(6), 868 – 870 (1999).

[109] W. Holmes, J.M. Gildemeister, P.L. Richards, and V. Kotsubo. "Measurements of thermal transport in low stress silicon nitride films." *Appl. Phys. Lett.*, **72**(18), 2250 –2252 (1998).

[110] M.M. Leivo and J.P. Pekola. "Thermal characteristics of silicon nitride membranes at sub-Kelvin temperatures." *Appl. Phys. Lett.*, **72**(11), 1305 – 1307 (1998).

[111] M.J. Li, C.A. Allen, S.A. Gordon, J.L. Kuhn, D.B. Mott, C.K. Stahle, and L.L. Wang. "Fabrication of pop-up detector arrays on Si wafers." *Proc. SPIE*, **3874**, 422 – 431 (1999).

[112] J.G. Staguhn, D.J. Benford, F. Pajot, T.J. Ames, J.A. Chervenak, E.N. Grossman, K.D. Irwin, B. Maffei, Jr. Moseley, S.H., T.G. Phillips, C.D. Reintsema, C. Rioux, R.A. Shafer, and G.M. Voellmer. "Astronomical demonstration of superconducting bolometer arrays." *Proc. SPIE*, **4855**, 100 – 107 (2003).

[113] W.A. Little. "The transport of heat between dissimilar solids at low temperature." *Can. J. Phys.*, **37**, 334 – 349 (1959).

[114] F.C. Wellstood, C. Urbina, and J. Clarke. "Hot-electron effects in metals." *Phys. Rev. B*, **49**(9), 5942 – 5955 (1994).

[115] A.J. Walton, W. Parkes, J.G. Terry, C. Dunare, J.T.M. Stevenson, A.M. Gundlach, G.C. Hilton, K.D. Irwin, J.N. Ullom, W.S. Holland, W.D. Duncan, M.D. Audley, P.A.R. Ade, R.V. Sudiwala, and E. Schulte. "Design and fabrication of the detector technology for SCUBA-2." *IEE Proceedings-Science, Measurement and Technology*, **151**(2), 110 – 120 (2004).

[116] A.T. Lee, S. Cho, J.M. Gildemeister, N. Halverson, W.L. Holzapfel, J. Mehl, M.J. Myers, T. Lanting, P.L. Richards, E. Rittweger, D. Schwan, H. Spieler, and Huan Tran. "Voltage-biased TES bolometers for the far-infrared to millimeter wavelength range." *Proc. SPIE*, **4855**, 129 – 135 (2003).

[117] D. Rosenberg, S.W. Nam, A.J. Miller, A. Salminen, E. Grossman, R.E. Schwall, and J.M. Martinis. "Near-unity absorption of near-infrared light in tungsten films." *Nucl. Instrum. Methods Phys. Res. A*, **520**(1-3), 537 – 540 (2004).

[118] N. Tralshawala, S. Aslam, R.P. Brekosky, T.C. Chen, E.F. Feliciano, F.M. Finkbeiner, M.J. Li, D.B. Mott, C.K. Stahle, and C.M. Stahle. "Design and fabrication of superconducting transition edge X-ray calorimeters." *Nucl. Instrum. Methods Phys. Res. A*, **444**(1-2), 188 – 191 (2000).

[119] C.K. Stahle, R.L. Kelley, S.H. Moseley, A.E. Szymkowiak, M. Juda, D. McCammon, and J. Zhang. "Thermalization of X-rays in evaporated tin and bismuth films used as the absorbing materials in X-ray calorimeters." *J. Low Temp. Phys.*, **93**(3-4), 257 – 262 (1993).

[120] C.K. Stahle, R.P. Brekosky, S.B. Dutta, K.C. Gendreau, R.L. Kelley, D. McCammon, R.A. McClanahan, S.H. Moseley, D.B. Mott, F.S. Porter, and A.K. Szymkowiak. "The physics and the optimization of the XRS calorimeters on Astro-E." *Nucl. Instrum. Methods Phys. Res. A*, **436**(1-2), 218 – 225 (1999).

[121] E.H. Sondheimer. "The mean free path of electrons in metals." *Adv. Phys.*, **1**, 1–42 (1952).

[122] G.V. Chester and A. Thellung. "The Law of Wiedemann and Franz." *Proc. Phys. Soc. (London)*, **77**(5), 1005 – 1013 (1961).

[123] J. T. Karvonen, L. J. Taskinen, and I. J. Maasilta. "Electron-phonon interaction in thin copper and gold films." *Phys. Stat. Solidi (in press)* (2005).

[124] Charles Kittel. *Introduction to Solid State Physics*. John Wiley, seventh ed. (1996).

[125] Neil W. Ashcroft and N. David Mermin. *Solid State Physics*. Harcourt Brace (1976).

[126] Liu Shumei, Zhang Dianlin, Jing Xiunian, Lu Li, Li Shanlin, Kang Ning, Wu Xiaosong, and J.J. Lin. "Upper critical field of Ti and α-TiAl alloys: Evidence of an intrinsic type-II superconductivity in pure Ti." *Phys. Rev. B*, **62**(13), 8695–8698 (2000).

[127] V.V. Boĭko, V.F. Gantnakherm, and V.A. Gasparov. "Temperature dependence of the probability for scattering of charge carriers in molybdenum and tungsten." *Sov. Phys. JETP*, **38**(3), 604–607 (1974).

[128] R.T. Johnson, O.E. Vilches, and J.C. Wheatley. "Superconductivity of Tungsten." *Phys. Rev. Lett.*, **16**(3), 101–104 (1966).

[129] D. U. Gubser and Jr. Soulen, R. J. "Thermodynamic Properties of Superconducting Iridium." *J. Low Temp. Phys.*, **13**(3/4), 211–226 (1973).

[130] R.F. Broom and P. Wolf. "Q factor and resonance amplitude of Josephson tunnel junctions." *Phys. Rev. B*, **16**(7), 3100 – 3107 (1977).

[131] M.A. Lindeman, R.P. Brekosky, E. Figueroa-Feliciano, F.M. Finkbeiner, M. Li, C.K. Stahle, C.M. Stahle, and N. Tralshawala. "Performance of Mo/Au TES microcalorimeters." *AIP Conf. Proc.*, **605**, 203 – 206 (2002).

[132] P.A.J. de Korte, H.F.C. Hoevers, J.W.A. den Herder, J.A.M. Bleeker, W.M.B. Tiest, M.P. Bruijn, M.L. Ridder, R.J. Wiegerink, J.S. Kaastra, J. van der Kuur, and W.A. Mels. "TES X-ray calorimeter-array for imaging spectroscopy." *Proc. SPIE*, **4851**, 779 – 789 (2003).

[133] Y. Ishisaki, U. Morita, T. Koga, K. Sato, T. Ohashi, K. Mitsuda, N.Y. Yamasaki, R. Fujimoto, N. Iyomoto, T. Oshima, K. Futamoto, Y. Takei, T. Ichitsubo, T. Fujimori, S. Shoji, H. Kudo, T. Nakamura, T. Arakawa, T. Osaka, T. Homma, H. Sato, H. Kobayashi, K. Mori, K. Tanaka, T. Morooka, S. Nakayama, K. Chinone, Y. Kuroda, M. Onishi, and K. Otake. "Present performance of a single pixel Ti/Au bilayer TES calorimeter." *Proc. SPIE*, **4851**, 831 – 841 (2003).

[134] Wouter Bergmann Tiest. *Energy Resolving Power of Transition-Edge X-ray Microcalorimeters*. Ph.D. thesis, University of Utrecht (2004).

[135] G. Holzer, M. Fritsch, M. Deutsch, J. Hartwig, and E. Forster. "K$\alpha_{1,2}$ and k$\beta_{1,3}$ x-ray emission lines of the 3d transition metals." *Phys. Rev. A*, **56**(6), 4554 – 4568 (1997).

[136] G.T.A. Kovacs, N.I. Maluf, and K.E. Petersen. "Bulk micromachining of silicon." *Proc. IEEE*, **86**(8), 1536 – 1551 (1998).

[137] M.P. Bruijn, H.F.C. Hoevers, W.A. Mels, J.W. Den Herder, and P.A.J. De Korte. "Options for an imaging array of micro-calorimeters for X-ray astronomy." *Nucl. Instrum. Methods Phys. Res. A*, **444**(1-2), 260 – 264 (2000).

[138] M.P. Bruijn, N.H.R. Baars, W.M.B. Tiest, A. Germeau, H.F.C. Hoevers, P.A.J. de Korte, W.A. Mels, M.L. Ridder, E. Krouwer, J.J. van Baar, and R.J. Wiegerink. "Development of an array of transition edge sensors for application in X-ray astronomy." *Nucl. Instrum. Methods Phys. Res. A*, **520**(1-3), 443 – 445 (2004).

[139] F. Lärmer and A. Schilp. "Method for anisotropically etching silicon." German Patent DE4241045 (1992).

[140] S.A. McAuley, H. Ashraf, L. Atabo, A. Chambers, S. Hall, J. Hopkins, and G. Nicholls. "Silicon micromachining using a high-density plasma source." *J. Phys D*, **34**, 2769 – 2774 (2001).

[141] J.A. Chervenak, F.M. Finkbeiner, T.R. Stevenson, D.J. Talley, R.P. Brekosky, S.R. Bandler, E. Figueroa-Feliciano, M.A. Lindeman, R.L. Kelley, T. Saab, and C.K. Stahle. "Fabrication of transition edge sensor X-ray microcalorimeters for constellation-X." *Nucl. Instrum. Methods Phys. Res. A*, **520**(1-3), 460 – 462 (2004).

[142] M.A. Lindeman, S. Bandler, R.P. Brekosky, J.A. Chervenak, E. Figueroa-Feliciano, F.M. Finkbeiner, R.L. Kelley, T. Saab, C.K. Stahle, and D.J. Talley. "Performance of compact TES arrays with integrated high-fill-fraction X-ray absorbers." *Nucl. Instrum. Methods Phys. Res. A*, **520**(1-3), 411 – 413 (2004).

[143] W.B. Doriese, J.A. Beall, J. Beyer, S. Deiker, L. Ferreira, G.C. Hilton, K.D. Irwin, J.M. Martinis, S.W. Nam, C.D. Reintsema, J.N. Ullom, L.R. Vale, and Y. Xu. "Time-division SQUID multiplexer for the readout of X-ray microcalorimeter arrays." *Nucl. Instrum. Methods Phys. Res. A*, **520**(1-3), 559 – 561 (2004).

[144] Z. Moktadir, M.P. Bruijn, R. Wiegerink, M. Elwenspoek, M. Ridder, and W.A. Mels. "Limitations of heat conductivity in cryogenic sensors due to surface roughness." *Proc. IEEE Sensors 2002*, pp. 1024 – 1027 (2002).

[145] P. Agnese, C. Buzzi, P. Rey, L. Rodriguez, and J.-L. Tissot. "New technological development for far infrared bolometer arrays [for FIRST telescope]." *Proc. SPIE*, **3698**(284-290) (1999).

[146] J.M. Gildemeister, A.T. Lee, and P.L. Richards. "Monolithic arrays of absorber-coupled voltage-biased superconducting bolometers." *Appl. Phys. Lett.*, **77**(24), 4040 – 4042 (2000).

[147] G.C. Hilton, J.A. Beall, S. Deiker, J. Beyer, L.R. Vale, C.D. Reintsema, J.N. Ullom, and K.D. Irwin. "Surface micromachining for transition-edge detectors." *IEEE Trans. Appl. Supercond.*, **13**(2), 664 – 667 (2003).

[148] M.P. Bruijn, W.M.B. Tiest, H.F.C. Hoevers, E. Krouwer, J. van der Kuur, M.L. Ridder, Z. Moktadir, R. Wiegerink, D. van Gelder, and M. Elwenspoek. "Development of arrays of transition edge sensors for application in X-ray astronomy." *Nucl. Instrum. Methods Phys. Res. A*, **513**(1-2), 143 – 146 (2003).

[149] P. Eriksson, J.Y. Andersson, and G. Stemme. "Theoretical and experimental investigation of interferometric absorbers for thermal infrared detectors." *Sens. Mater.*, **9**(2), 117 – 130 (1997).

[150] B.E. Cole, R.E. Higashi, and R.A. Wood. "Monolithic two-dimensional arrays of micromachined microstructures for infrared applications." *Proc. IEEE*, **86**(8), 1679 – 1686 (1998).

[151] K. Tanaka, T. Morooka, K. Chinone, M. Ukibe, F. Hirayama, M. Ohkubo, and M. Koyanagi. "Strong, easy-to-manufacture, transition edge x-ray sensor." *Appl. Phys. Lett.*, **77**(25), 4196 – 4198 (2000).

[152] Robin Cantor (2004). Private communication.

[153] F. I. Chang, R. Yeh, G. Lin, P. B. Chu, E. Hoffman, E. J. J. Kruglick, and K. S. J. Pister. "Gas-phase silicon micromachining with xenon difluoride." *Proc. SPIE*, **2641**, 117–128 (1995).

[154] J.A. Chervenak, K.D. Irwin, E.N. Grossman, J.M. Martinis, C.D. Reintsema, and M.E. Huber. "Superconducting multiplexer for arrays of transition edge sensors." *Appl. Phys. Lett.*, **74**(26), 4043 – 4045 (1999).

[155] P.A.J. de Korte, J. Beyer, S. Deiker, G.C. Hilton, K.D. Irwin, M. MacIntosh, Sae Woo Nam, C.D. Reintsema, L.R. Vale, and M.E. Huber. "Time-division superconducting quantum interference device multiplexer for transition-edge sensors." *Rev. Sci. Instrum.*, **74**(8), 3807 – 3815 (2003).

[156] Jongsoo Yoon, J. Clarke, J.M. Gildemeister, A.T. Lee, M.J. Myers, P.L. Richards, and J.T. Skidmore. "Single superconducting quantum interference device multiplexer for arrays of low-temperature sensors." *Appl. Phys. Lett.*, **78**(3), 371 – 373 (2001).

[157] M. Kiviranta, H. Seppa, J. van der Kuur, and P. de Korte. "SQUID-based readout schemes for microcalorimeter arrays." *AIP Conf. Proc.*, **605**, 295 – 300 (2002).

[158] K.D. Irwin and K.W. Lehnert. "Microwave squid multiplexer." *Appl. Phys. Lett.*, **85**(11), 2107–2109 (2004).

[159] B.S. Karasik and W.R. McGrath. *Proceedings of the 12th International Symposium on Space Terahertz Technology, San Diego, February 13-16* (2001).

[160] K.D. Irwin. "SQUID multiplexers for transition-edge sensors." *Physica C*, **368**(1-4), 203 – 210 (2002).

[161] K. Kazami, J. Kawai, and G. Uehara. "Basic study on multiplexed superconducting quantum interference device for multichannel biomagnetometer." *Jap. Journ. Appl. Phys.*, **35**(pt.2 8B), L1055–8 (1996).

[162] H. Krause, S. Gartner, N. Wolters, R. Hohmann, W. Wolf, J. Schubert, W. Zander, Yi Zhang, M. v. Kreutzbruck, and M. Muck. "Multiplexed squid array for non-destructive evaluation of aircraft structures." *IEEE Trans Appl. Superconductivity*, **11**(1), 1168 – 1171 (2001).

[163] M. Muck. "A three channel squid-system using a multiplexed readout." *IEEE Transactions on Magnetics*, **27**(2), 2986 – 2988 (1992).

[164] K.D. Irwin, L.R. Vale, N.E. Bergren, S. Deiker, E.N. Grossman, G.C. Hilton, S.W. Nam, C.D. Reintsema, D.A. Rudman, and M.E. Huber. "Time-division SQUID multiplexers." *AIP Conf. Proc.*, **605**, 301 – 304 (2002).

[165] C.D. Reintsema, J. Beyer, Sae Woo Nam, S. Deiker, G.C. Hilton, K. Irwin, J. Martinis, J. Ullom, L.R. Vale, and M. MacIntosh. "Prototype system for superconducting quantum interference device multiplexing of large-format transition-edge sensor arrays." *Rev. Sci. Instrum.*, **74**(10), 4500 – 4508 (2003).

[166] D.J. Benford, C.A. Allen, J.A. Chervenak, M.M. Freund, A.S. Kutyrev, S.H. Moseley, R.A. Shafer, J.G. Staguhn, E.N. Grossman, G.C. Hilton, K.D. Irwin, J.M. Martinis, S.W. Nam, and C.D. Reintsema. "Multiplexed readout of superconducting bolometers." *Int. J. Infrared Millim. Waves*, **21**(12), 1909 – 1916 (2000).

[167] W.B. Doriese, J.A. Beall, S. Deiker, W.D. Duncan, L. Ferreira, G.C. Hilton, K.D. Irwin, C.D. Reintsema, J.N. Ullom, L.R. Vale, and Y. Xu. "Time-division multiplexing of high-resolution tes x-ray microcalorimeters: Four pixels and beyond." *Appl. Phys. Lett.*, **85**(20), 4762–4764 (2004).

[168] T. May, V. Zakosarenko, E. Kreysa, W. Esch, S. Anders, L. Fritzsch, R. Boucher, R. Stolz, J. Kunert, and Meyer H.G. "On-chip integrated squid readout for superconducting bolometers." (2004). Presented at the Applied Superconductivity Conference, Oct 4-8, 2004.

[169] M. Muck, C.G. Korn, A. Mugford, and J.B. Kycia. "A simple three-channel dc squid system using time domain multiplexing." *Rev. Sci. Instrum.*, **75**(8), 2660 – 2663 (2004).

[170] D.J. Benford, G.M. Voellmer, J.A. Chervenak, K.D. Irwin, S.H. Moseley, R.A. Shafer, and J.G. Staguhn. "Design and fabrication of a 2d superconducting bolometer array for safire." *Proc. SPIE*, **4857**, 125 – 135 (2003).

[171] D.J. Benford, M.J. Devlin, S.R. Dicker, K.D. Irwin, P.R. Jewell, J. Klein, B.S. Mason, H.S. Moseley, R.D. Norrod, and M.P. Supanich. "A 90 GHz array for the green bank telescope." *Nucl. Instrum. Methods Phys. Res. A*, **520**(1-3), 387 – 389 (2004).

[172] M. Radparvar. "A wide dynamic range single-chip squid magnetometer." *IEEE Trans. Appl. Supercond.*, **4**(2), 87 – 91 (1994).

[173] H. Furukawa and K. Shirae. "Multichannel dc squid system." *Jap. Journ. Appl. Phys.*, **28, pt.2**(3), L456–8 (1989).

[174] T.M. Lanting, Hsiao-Mei Cho, J. Clarke, M. Dobbs, A.T. Lee, P.L. Richards, H.G. Spieler, and A. Smith. "Frequency-domain multiplexing for large-scale bolometer arrays." *Proc. SPIE*, **4855**, 172 – 181 (2003).

[175] T. Miyazaki, M. Yamazaki, K. Futamoto, K. Mitsuda, R. Fujimoto, N. Iyomoto, T. Oshima, D. Audley, Y. Ishisaki, T. Kagei, T. Ohashi, N. Yamasaki, S. Shoji, H. Kudo, and Y. Yokoyama. "AC calorimeter bridge; a new multi-pixel readout method for TES calorimeter arrays." *AIP Conf. Proc.*, **605**, 313 – 316 (2002).

[176] A.T. Lee (2004). Private communication.

[177] J.N. Ullom, M.F. Cunningham, T. Miyazaki, S.E. Labov, J. Clarke, T.M. Lanting, A.T. Lee, P.L. Richards, Jongsoo Yoon, and H. Spieler. "A frequency-domain read-out technique for large microcalorimeter arrays demonstrated using high-resolution gamma -ray sensors." *IEEE Trans. Appl. Supercond.*, **13**(2), 643 – 648 (2003).

[178] M.J. Myers, W. Holzapfel, A.T. Lee, R. O'Brient, P.L. Richards, D. Schwan, A.D. Smith, H. Spieler, and H. Tran. "Arrays of antenna-coupled bolometers using transition edge sensors." *Nucl. Instrum. Methods Phys. Res. A*, **520**(1-3), 424 – 426 (2004).

[179] T.R. Stevenson, F.A. Pellerano, C.M. Stahle, K. Aidala, and R.J. Schoelkopf. "Multiplexing of radio-frequency single-electron transistors." *Appl. Phys. Lett.*, **80**(16), 3012 – 3014 (2002).

[180] P.K. Day, H.G. LeDuc, B.A. Mazin, A. Vayonakis, and J. Zmuidzinas. "A broadband superconducting detector suitable for use in large arrays." *Nature*, **425**(6960), 817 – 821 (2003).